The Journal of Chemical Physics

RESEARCH ARTICLE | NOVEMBER 20 2025

ABACUS: An electronic structure analysis package for the AI era

Weiqing Zhou ; Daye Zheng; Qianrui Liu ; Denghui Lu ; Yu Liu ; Peize Lin; Yike Huang ; Xingliang Peng; Jie J. Bao; Chun Cai ; Zuxin Jin ; Jing Wu; Haochong Zhang; Gan Jin; Yuyang Ji; Zhenxiong Shen; Xiaohui Liu; Liang Sun; Yu Cao ; Menglin Sun; Jianchuan Liu ; Tao Chen ; Renxi Liu ; Yuanbo Li ; Haozhi Han ; Xinyuan Liang ; Taoni Bao ; Zichao Deng; Tao Liu; Nuo Chen ; Hongxu Ren; Xiaoyang Zhang ; Zhaoqing Liu; Yiwei Fu; Maochang Liu ; Zhuoyuan Li; Tongqi Wen ; Zechen Tang; Yong Xu ; Wenhui Duan ; Xiaoyang Wang; Qiangqiang Gu ; Fu-Zhi Dai; Qijing Zheng; Yang Zhong ; Hongjun Xiang ; Xingao Gong; Jin Zhao ; Yuzhi Zhang ; Qi Ou ; Hong Jiang ; Shi Liu ; Ben Xu ; Shenzhen Xu ; Xinguo Ren ; Lixin He ; Linfeng Zhang; Mohan Chen

J. Chem. Phys. 163, 192501 (2025)
https://doi.org/10.1063/5.0297563

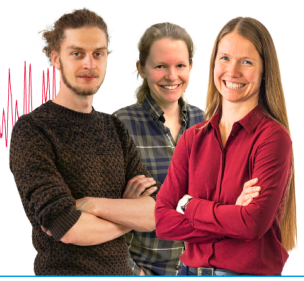

The Journal of Chemical Physics SOFTWARE pubs.aip.org/aip/jcp

ABACUS: An electronic structure analysis package for the AI era

Cite as: J. Chem. Phys. 163, 192501 (2025); doi: 10.1063/5.0297563
Submitted: 20 August 2025 • Accepted: 25 October 2025 •
Published Online: 20 November 2025

Weiqing Zhou,[1,2] Daye Zheng,[1] Qianrui Liu,[3] Denghui Lu,[1,3] Yu Liu,[3] Peize Lin,[4] Yike Huang,[1] Xingliang Peng,[1] Jie J. Bao,[1] Chun Cai,[1] Zuxin Jin,[1] Jing Wu,[1] Haochong Zhang,[4] Gan Jin,[4] Yuyang Ji,[5] Zhenxiong Shen,[4,5] Xiaohui Liu,[6] Liang Sun,[3] Yu Cao,[3,7] Menglin Sun,[8] Jianchuan Liu,[9] Tao Chen,[3] Renxi Liu,[1,3,10] Yuanbo Li,[3] Haozhi Han,[1,3] Xinyuan Liang,[3,10] Taoni Bao,[3] Zichao Deng,[3] Tao Liu,[3] Nuo Chen,[3] Hongxu Ren,[3] Xiaoyang Zhang,[1,3] Zhaoqing Liu,[11] Yiwei Fu,[12] Maochang Liu,[12,13] Zhuoyuan Li,[14,15] Tongqi Wen,[14,15] Zechen Tang,[16] Yong Xu,[16,17,18] Wenhui Duan,[16,17,19] Xiaoyang Wang,[20] Qiangqiang Gu,[1,21] Fu-Zhi Dai,[1,22] Qijing Zheng,[23] Yang Zhong,[24] Hongjun Xiang,[24] Xingao Gong,[24] Jin Zhao,[23] Yuzhi Zhang,[1,25] Qi Ou,[26] Hong Jiang,[11] Shi Liu,[27,28] Ben Xu,[29] Shenzhen Xu,[1,8] Xinguo Ren,[7,a)] Lixin He,[4,5,30,b)] Linfeng Zhang,[1,25] and Mohan Chen[1,3,c)]

AFFILIATIONS

[1]AI for Science Institute, Beijing 100080, People's Republic of China
[2]Key Laboratory of Artificial Micro- and Nano-structures of Ministry of Education and School of Physics and Technology, Wuhan University, Wuhan 430072, People's Republic of China
[3]HEDPS, CAPT, School of Mechanics and Engineering Science and School of Physics, Peking University, Beijing 100871, People's Republic of China
[4]Institute of Artificial Intelligence, Hefei Comprehensive National Science Center, Hefei 230026, People's Republic of China
[5]Key Laboratory of Quantum Information, University of Science and Technology of China, Hefei 230026, People's Republic of China
[6]Supercomputing Center, University of Science and Technology of China, Hefei, Anhui 230026, People's Republic of China
[7]Institute of Physics, Chinese Academy of Sciences, Beijing 100190, People's Republic of China
[8]School of Materials Science and Engineering, Peking University, Beijing 100871, People's Republic of China
[9]School of Electrical Engineering and Electronic Information, Xihua University, Chengdu 610039, People's Republic of China
[10]Academy for Advanced Interdisciplinary Studies, Peking University, Beijing 100871, People's Republic of China
[11]College of Chemistry and Molecular Engineering, Peking University, Beijing 100871, People's Republic of China
[12]International Research Center for Renewable Energy, State Key Laboratory of Multiphase Flow, Xi'an Jiaotong University, Xi'an, Shaanxi 710049, People's Republic of China
[13]Suzhou Academy of Xi'an Jiaotong University, Suzhou, Jiangsu 215123, People's Republic of China
[14]Center for Structural Materials, Department of Mechanical Engineering, The University of Hong Kong, Hong Kong, People's Republic of China
[15]Materials Innovation Institute for Life Sciences and Energy (MILES), The University of Hong Kong, Shenzhen, People's Republic of China
[16]State Key Laboratory of Low Dimensional Quantum Physics and Department of Physics, Tsinghua University, Beijing 100084, People's Republic of China
[17]Frontier Science Center for Quantum Information, Beijing, People's Republic of China
[18]RIKEN Center for Emergent Matter Science (CEMS), Wako, Saitama 351-0198, Japan
[19]Institute for Advanced Study, Tsinghua University, Beijing 100084, People's Republic of China
[20]Laboratory of Computational Physics, Institute of Applied Physics and Computational Mathematics, Fenghao East Road 2, Beijing 100094, People's Republic of China
[21]School of Artificial Intelligence and Data Science, University of Science and Technology of China, Hefei 230026, People's Republic of China

[22]School of Materials Science and Engineering, University of Science and Technology Beijing, Beijing 100083, People's Republic of China
[23]Department of Physics, University of Science and Technology of China, Hefei, Anhui 230026, People's Republic of China
[24]Key Laboratory of Computational Physical Sciences (Ministry of Education), Institute of Computational Physical Sciences, State Key Laboratory of Surface Physics, and Department of Physics, Fudan University, Shanghai 200433, People's Republic of China
[25]DP Technology, Beijing 100080, People's Republic of China
[26]Basic Research Department, SINOPEC Research Institute of Petroleum Processing Co., Ltd., Beijing 100083, People's Republic of China
[27]Department of Physics, School of Science, Westlake University, Hangzhou, Zhejiang 310030, People's Republic of China
[28]Institute of Natural Sciences, Westlake Institute for Advanced Study, Hangzhou, Zhejiang 310024, People's Republic of China
[29]Graduate School of China Academy of Engineering Physics, Beijing 100193, People's Republic of China
[30]Synergetic Innovation Center of Quantum Information and Quantum Physics, University of Science and Technology of China, Hefei 230026, People's Republic of China

Note: This paper is part of the Special Topic on Electronic Structure Software 2.0.
[a)]**Electronic mail:** renxg@iphy.ac.cn
[b)]**Electronic mail:** helx@ustc.edu.cn
[c)]**Author to whom correspondence should be addressed:** mohanchen@pku.edu.cn

ABSTRACT

ABACUS (Atomic-orbital Based *Ab initio* Computation at USTC) is an open-source software for first-principles electronic structure calculations and molecular dynamics simulations. It mainly features density functional theory (DFT) and molecular dynamics functions and is compatible with both plane wave basis sets and numerical atomic orbital basis sets. ABACUS serves as a platform that facilitates the integration of various electronic structure methods, such as Kohn–Sham DFT, stochastic DFT, orbital-free DFT, real-time time-dependent DFT, etc. In addition, with the aid of high-performance computing, ABACUS is designed to perform efficiently and provide massive amounts of first-principles data for generating general-purpose machine learning potentials, such as deep potential with attention models. Furthermore, ABACUS serves as an electronic structure platform that interfaces with several artificial intelligence-assisted algorithms and packages, such as DeePKS-kit, DeePMD, DP-GEN, DeepH, DeePTB, HamGNN, etc.

I. INTRODUCTION

The theoretical foundations of density-based methodologies can be traced to the Thomas–Fermi (TF) model proposed in 1927. The TF model established the first kinetic energy functional based on the uniform electron gas approximation.[1,2] Although this orbital-free (OF) framework pioneered the conceptual basis for density functional theory (DFT), its oversimplified treatment of kinetic energy limited chemical accuracy.[3] In 1964, Hohenberg and Kohn[4] established two theorems. First, the external potential of a many-electron system is uniquely determined by its electron density. Second, a universal energy functional exists whose minimum value corresponds to the ground-state electron density. Later in 1965, Kohn and Sham[5] developed the Kohn–Sham density functional theory (KS-DFT), whose accuracy is determined by the exchange–correlation functional. This framework allows a non-interacting electron system where the kinetic energy can be computed exactly via electronic wave functions. Crucially, the non-interacting system can yield the electron density of the real system via the so-called self-consistent field (SCF) method.

Over the past few decades, driven by developments of the DFT method itself and continuous refinement of numerical algorithms, various popular KS-DFT packages have emerged.[6–17] In addition, with the exponential growth in computing capabilities, the KS-DFT method has become a cornerstone to predict various properties of materials in physics, chemistry, materials science, biology, geophysics, etc. Despite these achievements, challenges still remain. For example, the community increasingly demands DFT implementations that combine enhanced computational efficiency with improved hardware adaptability across different architectures. Recently, with rapid advancements in artificial intelligence (AI) technologies, an important question arises: can these new technologies drive substantial improvements in computational accuracy and efficiency for electronic structure methods such as KS-DFT and OF-DFT?

In this review paper, we introduce the ABACUS package, which was initiated around 2006 and has achieved a series of progress over the past two decades.[18–30] For instance, the ABACUS package supports both plane wave (PW) basis and numerical atomic orbital (NAO) basis for first-principles electronic structure calculations,

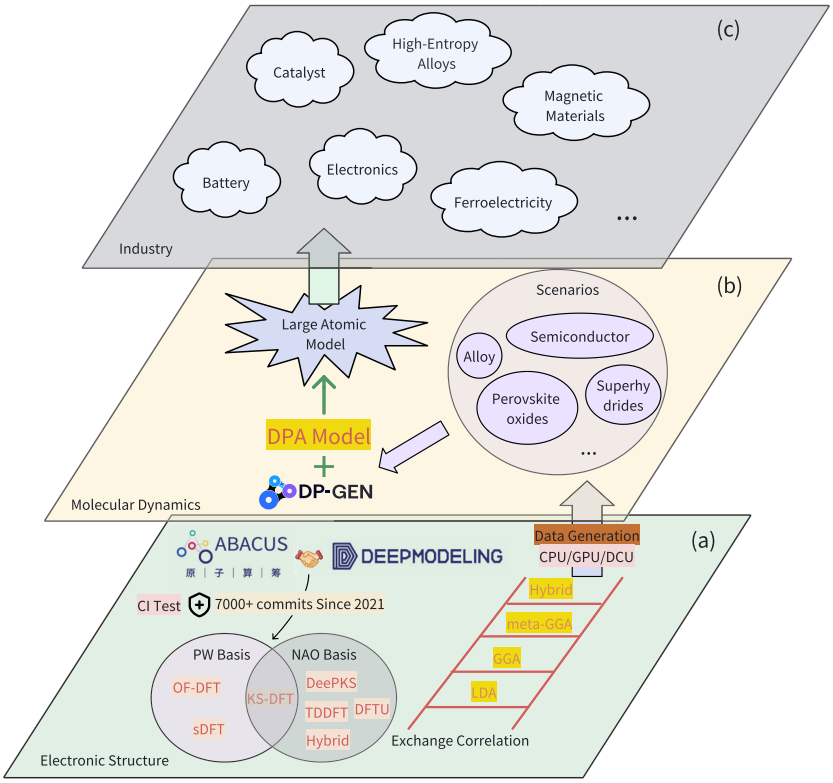

FIG. 1. ABACUS is dedicated to building an algorithm platform and data engine for AI4ES (AI for Electronic Structure). (a) Since partnering with the open-source community DeepModeling in 2021, ABACUS has garnered over 7300 commits under the protection of Continuous Integration (CI) tests. Its adaptable architecture allows developers to incorporate numerous electronic structure algorithms. (b) The AI-assisted functional correction method DeePKS permits ABACUS to achieve precise functional results at a reduced cost. Owing to high-performance implementation on various devices, ABACUS effectively produces extensive first-principles data across multiple sectors. (c) Combining advanced electronic structure algorithms and AI-assisted pre-trained models, one can transfer the precision of quantum mechanics across scales.

geometry relaxation, and molecular dynamics (MD) simulations. In addition, ABACUS offers robust support for highly efficient parallelization of diverse electronic structure methods, leveraging MPI, OpenMP, and CUDA to optimize performance across distributed and accelerated computing architectures. Based on recent advancements in AI technologies for atomistic simulations and electronic structure methods,[31–39] researchers have identified significant potential for AI to transform both electronic structure methods and their corresponding software implementations. In this context, the effort to create an integrated platform that integrates physics-based models, high-performance computing (HPC), and AI capabilities has become particularly critical. Since 2021, the ABACUS development team has maintained an ongoing collaboration with the DeepModeling open-source community.[40]

As illustrated in Fig. 1, ABACUS aims to establish an electronic structure algorithmic platform (Fig. 2) and computational engine tailored for the AI for Science (AI4S) paradigm. This integration features three aspects. First, state-of-the-art electronic structure method developments with AI-assisted algorithms. Second, molecular dynamics simulations to provide data for the OpenLAM project,[41] which is designed to generate a general-purpose machine learning (ML) model for the periodic table. Third, the platform can be potentially used in various industry fields such as battery, catalyst, electronics, ferroelectricity, magnetic materials, high-entropy alloys, etc.

In this work, we provide a detailed overview of the latest developments in ABACUS. Section II details the implementation of general features in ABACUS, such as the pseudopotentials, exchange–correlation functionals, SCF method, geometry relaxation, molecular dynamics, etc. Section III describes the implementation of the KS-DFT, stochastic DFT (sDFT), and OF-DFT methods with the plane wave basis. Moreover, recent advances in AI-assisted kinetic energy density functionals (KEDFs) are introduced for OFDFT. Section IV introduces the linear combination of atomic orbital (LCAO) calculation methods, where numerical atomic orbitals serve as a basis to solve the KS equation and yield forces and stress, as well as newly developed methods such as hybrid functional, the AI-assisted electronic structure method DeePKS, DFT+U, and real-time time-dependent DFT (RT-TDDFT), all of which are based on the numerical atomic orbital basis. Section V mainly focuses on the machine-learning-based interatomic potentials and describes the role played by ABACUS. Section VI presents various software interfaces between ABACUS and other packages. Finally, we conclude this paper in Sec. VII.

II. KOHN–SHAM DENSITY FUNCTIONAL THEORY

A. Kohn–Sham equation

In KS-DFT, the electronic orbitals are obtained by solving the following KS equation:

$$\left[-\frac{1}{2}\nabla^2 + \hat{V}_{\mathrm{KS}}\right]\psi_i = \varepsilon_i\psi_i, \tag{1}$$

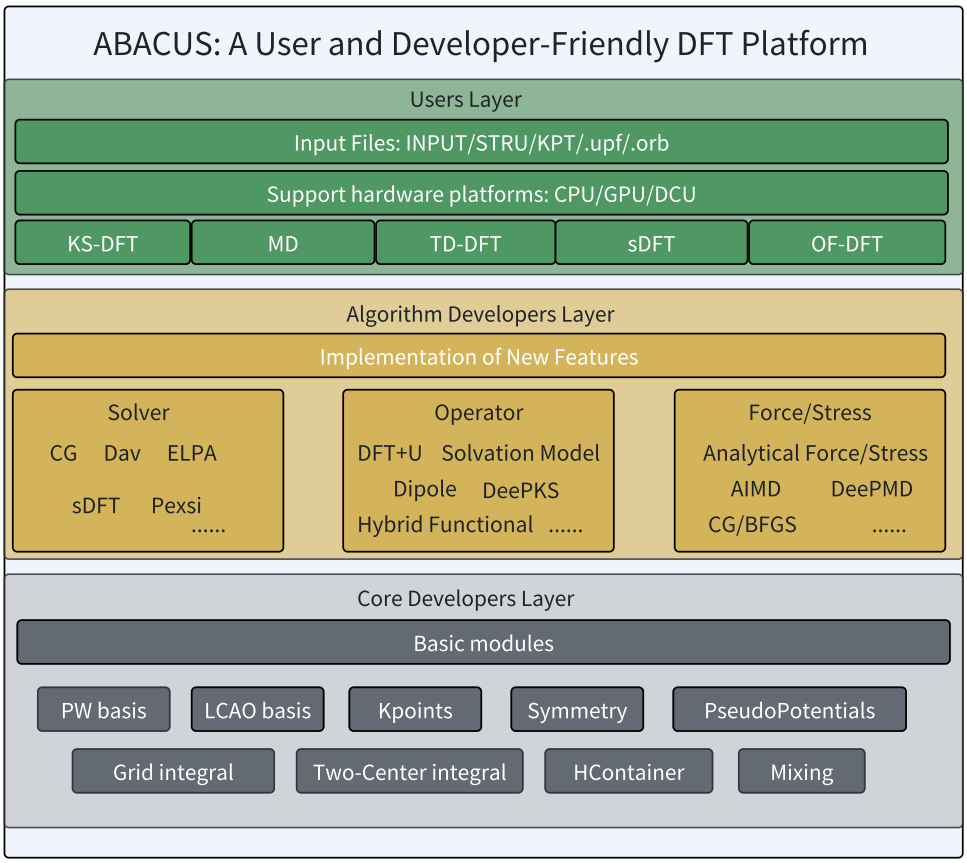

FIG. 2. Code architecture of ABACUS. For users, a few input files need to be prepared in advance, including **INPUT**, **STRU**, **KPT**, pseudopotential files, and orbital files (only for numerical atomic orbital calculations). For developers, the software features a highly modular design that allows for the swift integration of new functionalities. The development team is responsible for formulating and refining key data structures, mathematical routines, and other foundational components in ABACUS. For instance, the `HContainer` module is utilized for storing sparse matrices under the numerical atomic orbital basis set, such as Hamiltonian and density matrices; the `Grid Integral` module is implemented for grid integration.

where ψ_i is the Kohn–Sham wave function with energy ε_i, and $\hat{V}_{\mathrm{KS}}$ is an effective potential written as

$$\hat{V}_{\mathrm{KS}} = \hat{V}_{\mathrm{ext}} + \hat{V}_{\mathrm{H}} + \hat{V}_{\mathrm{xc}}. \tag{2}$$

Here, the three terms on the right-hand side are the external potential term, the Hartree term, and the exchange–correlation (XC) term, respectively. Typically, the external potential term includes the ion–electron interactions that can be described via pseudopotentials, as well as external fields such as the electric field.

The KS equation can be solved via different types of basis sets, such as plane waves,[8,14,16] numerical atomic orbitals,[9,15,42,43] real-space grids,[11,44] Gaussian orbitals,[10,17] wavelet basis sets,[45] etc. Currently, ABACUS supports both plane waves and NAOs as basis sets. On the one hand, the plane wave basis can accurately and efficiently handle periodic systems with a relatively small number of atoms. On the other hand, the NAOs are centered on atoms, and the required number of basis sets is substantially less than the plane wave basis. Therefore, the NAO basis is suitable to simulate systems containing thousands of atoms.[10,15]

1. Pseudopotentials

The Coulomb potential exhibits a singularity at the atomic nucleus, necessitating an extensive basis set for the precise representation of "near-core" wave functions, which imposes substantial computational overhead. To overcome this challenge, several pseudopotential methodologies have been developed in the past few decades.[16,46–52] These pseudopotentials achieve a significant reduction in computational costs while preserving computational accuracy.

ABACUS supports both norm-conserving pseudopotentials (NCPPs)[53] and ultrasoft pseudopotentials (USPPs).[49] In particular, the pseudopotential operator $\hat{V}_{\mathrm{ps}}$ is decomposed into local and nonlocal components in NCPPs as

$$\hat{V}_{\mathrm{ps}} = \hat{V}_{\mathrm{local}} + \hat{V}_{\mathrm{KB}}, \tag{3}$$

where the local pseudopotential (LPS) $\hat{V}_{\mathrm{local}}$ equals the all-electron functions beyond a cutoff radius. Furthermore, $\hat{V}_{\mathrm{KB}}$ is composed of a set of separable nonlocal projectors as proposed by Kleinman and Bylander,[54] later extended by Hamann.[52] The formula is

$$\hat{V}_{\mathrm{KB}} = \sum_{ll'mm'} D_{ll'} |\beta_{lm}\rangle\langle\beta_{l'm'}|. \tag{4}$$

Here, β_{lm} is a projector with angular quantum number l and magnetic quantum number m, and its weighting factor is $D_{ll'}$. In addition, these projectors β_{lm} are expressed as the product of a radial function and a spherical harmonic function. In cases such as transition metals (TMs) or magnetic systems, the non-linear core corrections[55] are usually adopted in the pseudopotential file to improve the transferability of pseudopotentials. For the spin-orbital coupling

(SOC) effect, it can be incorporated into the non-local projectors in the $\hat{V}_{\mathrm{KB}}$ term.[56–58]

Compared to NCPPs, the ultrasoft pseudopotentials[49] offer substantially improved computational efficiency by removing the norm-conservation constraint, which allows greater flexibility in constructing the pseudo-wave function within the core region, yielding inherently softer wave functions that reduce computational overhead. As a result, USPPs facilitate faster convergence of basis set expansions, although this advantage comes with the trade-off of requiring more sophisticated implementation within KS-DFT packages.

2. Exchange–correlation functionals

In KS-DFT codes, to describe the collinear spin of given systems, the spin-up electron density $\rho^{\uparrow}(\mathbf{r})$ and spin-down electron density $\rho^{\downarrow}(\mathbf{r})$ are usually treated separately and then summed up to the total electron density,

$$\rho(\mathbf{r}) = \rho^{\uparrow}(\mathbf{r}) + \rho^{\downarrow}(\mathbf{r}), \tag{5}$$

while the spin density takes the form of

$$m(\mathbf{r}) = \rho^{\uparrow}(\mathbf{r}) - \rho^{\downarrow}(\mathbf{r}). \tag{6}$$

In this regard, the exchange–correlation energy $E_{\mathrm{xc}}[\rho^{\uparrow}, \rho^{\downarrow}]$ exhibits an explicit functional dependence on $\rho^{\uparrow}$ and $\rho^{\downarrow}$. The corresponding exchange–correlation potential for spin channel σ (where $\sigma \in \{\uparrow, \downarrow\}$) is derived via the functional derivative,

$$V_{\mathrm{xc},\sigma}(\mathbf{r}) = \frac{\delta E_{\mathrm{xc}}[\rho^{\uparrow}, \rho^{\downarrow}]}{\delta \rho_{\sigma}(\mathbf{r})}. \tag{7}$$

Since the invention of KS-DFT, numerous density functional approximations have been developed. The earliest implementation, the local density approximation (LDA),[5] is expressed as a functional of the spin-summed electron density $\rho(\mathbf{r})$. Subsequent refinements introduced the local spin density approximation (LSDA),[59,60] which incorporates spin density components $\rho^{\uparrow}$ and $\rho^{\downarrow}$ within a broken-symmetry Slater determinant framework, thereby correctly describing the dissociation limit of H_2.

Including density gradients $\nabla\rho(\mathbf{r})$ (or spin density gradients $\nabla\rho^{\uparrow}$ and $\nabla\rho^{\downarrow}$) as additional variables led to the development of generalized gradient approximation (GGA) functionals, some of which substantially improved the KS-DFT accuracy compared to LDA/LSDA. For instance, the Perdew–Burke–Ernzerhof (PBE) functional[61] reduces the mean absolute error (MAE) for molecular atomization energies of 20 main-group molecules from 31.4 kcal/mol (LSDA) to 7.9 kcal/mol.

Further advancement was achieved with meta-GGA functionals, which incorporate the kinetic energy density $\tau(\mathbf{r})$. This class of functionals, exemplified by the strongly constrained and appropriately normed (SCAN) functional,[62] offers enhanced accuracy over GGAs. Variants of SCAN, such as rSCAN[63] and R2SCAN,[64] were subsequently developed to improve numerical stability and convergence while largely retaining its accuracy.

One may also include a fraction of exact Hartree–Fock (HF) exchange energy into the exchange–correlation term, and the resulting functional is called a hybrid functional, such as the HSE06,[65,66] PBE0,[67] and B3LYP functionals.[68]

Analogous to spin-unpolarized systems, approximations for $E_{\mathrm{xc}}[\rho^{\uparrow}, \rho^{\downarrow}]$ are typically constructed hierarchically. The simplest approach, the LSDA,[69] expresses E_{xc} solely as a function of the local spin densities $\rho^{\sigma}(\mathbf{r})$. More refined treatments, such as the generalized gradient approximation (GGA), introduce additional dependence on the gradients of the spin densities $\nabla\rho^{\sigma}(\mathbf{r})$. Further sophistication is achieved in meta-GGA functionals through the incorporation of the kinetic energy density, while hybrid functionals explicitly include fractional exact exchange (EXX) integrals.

The LDA, GGA, and meta-GGA functionals have already been implemented in ABACUS for both plane wave and numerical atomic orbital basis sets. Both LDA and GGA functionals are accessible through either native implementations or the Libxc library,[70] whereas the meta-GGA functional is currently restricted to Libxc. Benchmark studies of SCAN, rSCAN,[63] and r2SCAN[64] within ABACUS are detailed in Ref. 29. Efficient hybrid functional calculations are available for localized basis sets, utilizing combined capabilities of Libxc and the local resolution of identity (LRI) methodology (see Sec. IV D for the computational details).

3. Non-collinear spin

The non-collinear spin calculation allows electron spins to orient in arbitrary directions rather than being restricted to a single axis. Within the framework of non-collinear spin KS-DFT, the Kohn–Sham electronic wave function i can be represented as two-component spinors as

$$\Psi_i(\mathbf{r}) = \begin{pmatrix} \psi_i^{\uparrow}(\mathbf{r}) \\ \psi_i^{\downarrow}(\mathbf{r}) \end{pmatrix}. \tag{8}$$

The spin-resolved density matrix $\rho^{\sigma\sigma'}$ (with $\sigma, \sigma' \in \{\uparrow, \downarrow\}$) contains the full spin structure of the system. It can be further decomposed into charge and spin contributions via the Pauli matrices $\boldsymbol{\sigma} = (\sigma_x, \sigma_y, \sigma_z)$ and the identity matrix $\boldsymbol{I}$ as follows:

$$\begin{aligned} \begin{pmatrix} \rho^{\uparrow\uparrow} & \rho^{\uparrow\downarrow} \\ \rho^{\downarrow\uparrow} & \rho^{\downarrow\downarrow} \end{pmatrix} &= (\rho \boldsymbol{I} + \boldsymbol{\sigma} \cdot \boldsymbol{m}) \\ &= \frac{1}{2} \begin{pmatrix} \rho + m_z & m_x - i m_y \\ m_x + i m_y & \rho - m_z \end{pmatrix}, \end{aligned} \tag{9}$$

where $\boldsymbol{I}$ is a 2×2 identity matrix; and m_x, m_y, and m_z refer to the magnetic densities along the x, y, and z axes, respectively.

Next, the exchange–correlation potential V_{xc} adopts a 2×2 matrix form acting on two-component spinors,

$$V_{\mathrm{xc}}(\mathbf{r}) = \begin{pmatrix} V_{\mathrm{xc}}^{\uparrow\uparrow}(\mathbf{r}) & V_{\mathrm{xc}}^{\uparrow\downarrow}(\mathbf{r}) \\ V_{\mathrm{xc}}^{\downarrow\uparrow}(\mathbf{r}) & V_{\mathrm{xc}}^{\downarrow\downarrow}(\mathbf{r}) \end{pmatrix}, \tag{10}$$

where the off-diagonal elements $V_{\mathrm{xc}}^{\uparrow\downarrow}$ and $V_{\mathrm{xc}}^{\downarrow\uparrow}$ account for the spin-flip interactions arising from spin–orbit coupling (SOC) or other magnetic effects. These terms mediate the mixing between spin-up and spin-down states, enabling the description of non-collinear magnetism.

Using the Pauli matrix as a basis, the exchange–correlation potential can be converted into

$$
\begin{aligned}
v_{\mathrm{xc}}(\mathbf{r}) &= \frac{\delta E_{\mathrm{xc}}}{\delta \rho(\mathbf{r})} = \frac{1}{2}\Big[V_{\mathrm{xc}}^{\uparrow\uparrow}(\mathbf{r}) + V_{\mathrm{xc}}^{\downarrow\downarrow}(\mathbf{r})\Big],\\
b_{\mathrm{xc}}^{x}(\mathbf{r}) &= -\frac{\delta E_{\mathrm{xc}}}{\delta m_x(\mathbf{r})} = \frac{1}{2}\Big[V_{\mathrm{xc}}^{\uparrow\downarrow}(\mathbf{r}) + V_{\mathrm{xc}}^{\downarrow\uparrow}(\mathbf{r})\Big],\\
b_{\mathrm{xc}}^{y}(\mathbf{r}) &= -\frac{\delta E_{\mathrm{xc}}}{\delta m_y(\mathbf{r})} = \frac{i}{2}\Big[V_{\mathrm{xc}}^{\uparrow\downarrow}(\mathbf{r}) - V_{\mathrm{xc}}^{\downarrow\uparrow}(\mathbf{r})\Big],\\
b_{\mathrm{xc}}^{z}(\mathbf{r}) &= -\frac{\delta E_{\mathrm{xc}}}{\delta m_z(\mathbf{r})} = \frac{1}{2}\Big[V_{\mathrm{XC}}^{\uparrow\uparrow}(\mathbf{r}) - V_{\mathrm{XC}}^{\downarrow\downarrow}(\mathbf{r})\Big].
\end{aligned}
\tag{11}
$$

Here, $\mathbf{b}_{xc}$ is the effective exchange–correlation magnetic field, defined as the functional derivative of the exchange–correlation energy with respect to the magnetization density, and it can be decomposed into three independent components ($\mathbf{b}_{xc}^{x}, \mathbf{b}_{xc}^{y}, \mathbf{b}_{xc}^{z}$). During Hamiltonian construction, the potential must be reconstructed in its spinor form to operate on the two-component Kohn–Sham wave functions.

B. Self-consistent field method

1. Mixing of electron densities

The Kohn–Sham equations are typically solved through the SCF method, an iterative procedure where the input electron density ρ_{in} is systematically updated based on various mixing methods until achieving convergence. The efficiency and reliability of this procedure critically depend on the choice of electron density mixing algorithm, which serves the dual purpose of accelerating convergence toward the ground state while preventing stagnation in local minima. The simplest approach, linear (or "plain") mixing, updates the density for non-spin-polarized systems as

$$
\rho_{in}^{i+1} = \rho_{in}^{i} + \alpha_{\rho} R[\rho_{in}^{i}], \tag{12}
$$

where i denotes the iteration index. $\alpha_{\rho} \in [0,1]$ is the mixing parameter, and a residual vector can be defined as

$$
R[\rho_{\mathrm{in}}] = \rho_{\mathrm{out}} - \rho_{\mathrm{in}}. \tag{13}
$$

In addition to the linear mixing method, ABACUS implements Pulay's direct inversion in iterative subspace (DIIS) method[71,72] and Broyden's quasi-Newton approach.[73] Figure 3 illustrates the electron density mixing strategies implemented in ABACUS to guarantee stable SCF convergence.

Magnetic calculations usually exhibit significantly poorer convergence behavior compared to their non-magnetic counterparts, frequently encountering two distinct failure cases, i.e., divergence of SCF or convergence to excited magnetic configurations. These

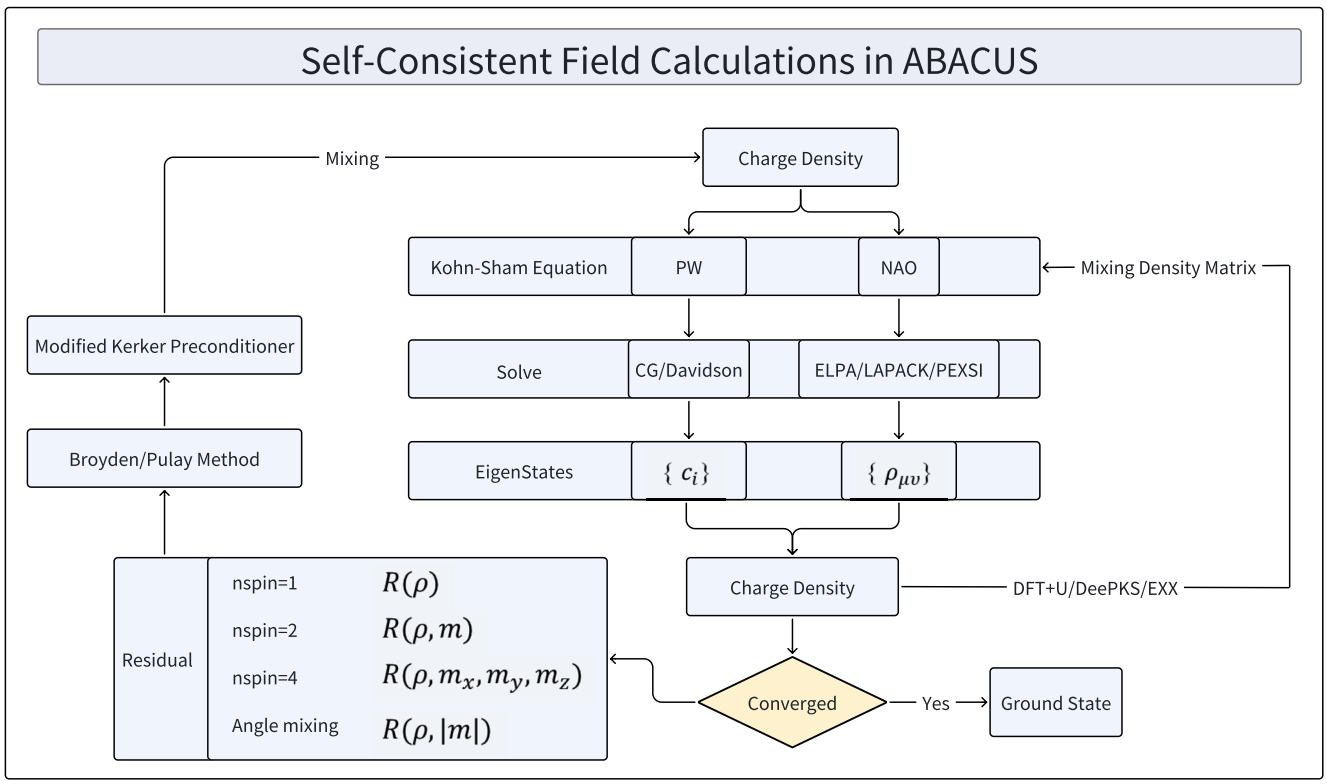

FIG. 3. ABACUS performs self-consistent field (SCF) calculations with two available basis sets: PW and NAOs. The PW basis set employs iterative diagonalization methods such as CG and Davidson to solve the Kohn–Sham equations. For NAOs, it uses exact diagonalization or the low-scaling method PEXSI.[74,75] ABACUS applies different mixing algorithms for various types of calculations, including non-magnetic, collinear, and non-collinear. In addition, ABACUS supports the density matrix mixing method for DFT+U, hybrid functionals (EXX), and DeePKS calculations with the NAO basis set.

issues are due to the complex coupling between charge and magnetization degrees of freedom when solving the Kohn–Sham equations. To address these challenges, ABACUS implements a mixing scheme that explicitly accounts for spin polarization. For collinear cases, the residual vector R is reformulated to simultaneously track both charge and magnetization density variations,

$$R(\rho, \boldsymbol{m}) = R(\rho^{\uparrow} + \rho^{\downarrow}, \rho^{\uparrow} - \rho^{\downarrow}), \tag{14}$$

where ρ represents the total charge density and m denotes the magnetization vector. The mixing procedure employs a history-dependent update with wavevector-dependent preconditioning,

$$\begin{aligned} \rho_{in}^{i+1} &= \sum_{j=i-n}^{i} p_j \left[\rho_{in}^{j} + \alpha_{\rho} \frac{q^2}{q^2 + q_{\rho}^2} \left(\rho_{out}^{j} - \rho_{in}^{j} \right) \right], \\ \boldsymbol{m}_{in}^{i+1} &= \sum_{j=i-n}^{i} p_j \left[\boldsymbol{m}_{in}^{j} + \alpha_{m} \frac{q^2}{q^2 + q_{m}^2} \left(\boldsymbol{m}_{out}^{j} - \boldsymbol{m}_{in}^{j} \right) \right], \end{aligned} \tag{15}$$

where n determines the history length, p_j are the Pulay/Broyden coefficients determined according to the residual vector [Eq. (14)], and the q-dependent terms represent a modified Kerker preconditioner.[76] The damping parameters q_{ρ} and q_m control the suppression of long-wavelength oscillations in charge and magnetization densities, respectively.

ABACUS provides several choices to optimize magnetic calculations, beginning with the implementation of separate preconditioning parameters for charge q_{ρ} and magnetization q_m densities to address their distinct physical characteristics and convergence behaviors. By default, the code deactivates magnetic density preconditioning (setting $q_m = 0$) to prioritize numerical stability in most cases, while still providing users the flexibility to enable magnetic preconditioning when enhanced convergence for challenging magnetic systems is required. This approach combines robust default settings with customizable options, allowing the code to automatically handle routine cases while permitting users to fine-tune the mixing parameters for complex magnetic configurations. We compared the magnetic convergence for several magnetic materials using two versions of ABACUS (v3.4 and v3.5). All computational details are available online.[77] As illustrated in Fig. 4(a), a marked difference in SCF convergence behavior is observed between the two versions. Our findings demonstrate that ABACUS v3.5 achieves significantly enhanced convergence efficiency when compared to version 3.4 of ABACUS.

ABACUS generalizes the collinear mixing formalism to non-collinear magnetic calculations through an expanded residual definition that incorporates all magnetization components,

$$R = R(\rho, \boldsymbol{m}_x, \boldsymbol{m}_y, \boldsymbol{m}_z), \tag{16}$$

where $\boldsymbol{m}_x$ denotes the x-component of the magnetization density $\boldsymbol{m} = \rho^{\uparrow} - \rho^{\downarrow}$, with analogous definitions for the y and z components. While this formulation successfully extends the standard Broyden mixing approach [Eqs. (15) and (16)] to non-collinear cases, it may fail to converge to the true ground state when magnetic moment directions require optimization. To address this limitation, ABACUS implements an angle mixing scheme based on the work of Ref. 79. This approach reformulates the residual in terms of a reduced parameter space $R(\rho, |\boldsymbol{m}|)$. The residual incorporates the magnitude difference $|\boldsymbol{m}_{\text{in}}^{i}| - |\boldsymbol{m}_{\text{out}}^{i}|$, where $|\boldsymbol{m}_{\text{in}}^{i}|$ is the input spin density of the i-th iteration and $|\boldsymbol{m}_{\text{out}}^{i}|$ is the calculated output one. The mixing algorithm proceeds through three key steps at each iteration i. First, $|\boldsymbol{m}_{\text{in}}^{i+1}| = |\boldsymbol{m}_{\text{out}}^{i}|$ is ensured to keep the local moment unchanged. Second, for the angle relaxation, the input angle is computed as $\theta_{\text{in}}^{i+1} = \beta \theta_{\text{out}}^{i}$, where θ_{out}^{i} measures the angular deviation between $\boldsymbol{m}_{\text{in}}^{i}$ and $\boldsymbol{m}_{\text{out}}^{i}$, and β serves as a relaxation parameter. Third, $\boldsymbol{m}_{\text{in}}^{i+1}$ is restricted to the plane defined by $\boldsymbol{m}_{\text{in}}^{i}$ and $\boldsymbol{m}_{\text{out}}^{i}$ to maintain geometric consistency. This methodology enables efficient exploration of magnetic configuration space while avoiding common convergence pitfalls associated with traditional non-collinear mixing approaches.

Traditional SCF calculations typically focus solely on charge density mixing, neglecting the density matrix that plays a crucial role in methods such as DFT+U. This oversight creates inconsistency, particularly evident when the system is far from its ground state, as the DFT+U method[80–84] explicitly requires the density matrix. Such

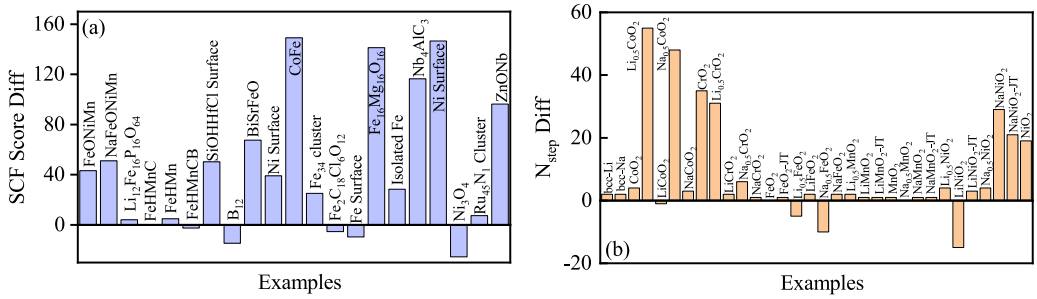

FIG. 4. (a) Differences in SCF performance score (*vide infra*) between v3.4 and v3.5 on the selection set of 21 examples. Prior to v3.4, the residual was defined by $\rho_{\uparrow}$ and $\rho_{\downarrow}$, whereas starting from v3.5, the residual is defined by the charge density and the magnetic density, and they are mixed separately. Since some test cases failed to converge in v3.4, we present results with convergence scores rather than directly using convergence steps. The max number of iterations is set to 100 in all calculations, and the SCF convergence threshold is `scf_thr=1e-6`. The SCF score is defined by $|\log_{10}(\delta\rho_{\text{last}})| \times 10 \times \frac{100}{N_{\text{step}}}$, where $\delta\rho_{\text{last}}$ is the density difference $R(\rho_{in})$ of the last iteration and N_{step} is the number of convergence iterations. (b) Difference in SCF convergence step (N_{step}) for the DFT+U calculation with only mixing charge density and both mixing charge density and density matrix. Here, "JT" represents a structure under Jahn–Teller distortion.[78] For the sake of reproduction, we have made public all the details of the calculations in the link,[77] where one can find the complete report and download all input files.

a discrepancy frequently leads to convergence difficulties in strongly correlated systems. To address this discrepancy, ABACUS supports a restart mixing scheme that begins with conventional charge density mixing during initial iterations when the density matrix cannot be reliably estimated from atomic wave function coefficients, then automatically switches to simultaneous mixing of both charge density and density matrix once a predefined convergence threshold is achieved.

The charge mixing scheme in DFT+U calculations can be further enhanced by an automated U-ramping procedure that gradually increases the U parameter during SCF iterations.[85,86] We performed DFT+U calculations on a series of selected magnetic materials (source files available online[77]) using ABACUS v3.6, with particular focus on comparing the SCF convergence behavior between calculations with and without density matrix mixing. Figure 4(b) demonstrates the reduction of SCF convergence steps after the density matrix mixing method is adopted.

2. Smearing methods

In metallic systems, SCF iterations frequently encounter convergence difficulties stemming from charge density oscillations. These oscillations arise because the electron occupation number drops abruptly to zero at the Fermi energy, with electronic states near the Fermi surface frequently switching between filled and empty electronic states. Furthermore, there exists no variational principle that regulates the convergence of the system's total energy with respect to k-point sampling. Smearing methods mitigate this issue by introducing a controlled degree of partial occupation for Kohn–Sham orbitals in the vicinity of the Fermi energy, effectively damping numerical instabilities and promoting convergence. A few smearing methods that have been implemented in ABACUS are listed below.

First, the electron occupancy can be approximated by a Gaussian distribution,

$$f(\varepsilon) = \frac{1}{w\sqrt{2\pi}} e^{\frac{(\varepsilon-E_{\mathrm{F}})^2}{2w^2}}, \tag{17}$$

where E_{F} denotes the Fermi energy, ε represents the single-particle energy levels, and w controls the broadening width.

Second, the Fermi–Dirac smearing scheme is intrinsically aligned with finite-temperature density functional theory,[87] where the electronic temperature T governs the statistical electron distribution. Crucially, within this framework, the smearing width ($k_B T$) arises as a natural consequence of thermal excitations in the electronic system, rather than serving as an empirically tuned broadening parameter. The formula is

$$f(\varepsilon) = \frac{1}{1+\exp\left(\frac{\varepsilon-E_{\mathrm{F}}}{k_B T}\right)}, \tag{18}$$

where k_B denotes Boltzmann's constant. However, in comparison to Gaussian smearing, the drawback of the Fermi–Dirac smearing method lies in its long tail, which necessitates the calculation and storage of a large number of partially occupied states to obtain the charge density.

Third, through smooth approximations of the δ and step functions (Fermi–Dirac-like), the Methfessel–Paxton (MP) method[88] enables the Brillouin-zone integration in metals to converge exponentially with the number of sampling points. The approximation formulas for the step function can be written as

$$\begin{aligned} S_0(x) &= \frac{1}{2}[1-\mathrm{erf}\,(x)], \\ S_N(x) &= S_0(x) + \sum_{n=1}^{N} A_n H_{2n-1}(x) e^{-x^2}, \end{aligned} \tag{19}$$

where $x = \frac{\varepsilon-E_{\mathrm{F}}}{w}$, $\mathrm{erf}(x)$ is the error function, and H_n represents the N-th Hermite polynomial with the expansion coefficient A_n. Using the formula above, $S_N(x)$ can be used to accurately compute the integral $\int S_N(x)F(x)dx$, where $F(x)$ represents the physical quantities such as the density of states (DOS). Although the broadening function of the MP smearing method ensures that the total free energy remains independent of the smearing temperature up to at least third order, thereby making Hellmann–Feynman forces consistent with the total free energy, it still introduces nonmonotonic and non-positive-definite occupation functions.

Fourth, to address possible negative occupancies that may lead to negative total electron density during SCF and numerical instability in the MP method, Marzari *et al.* introduced the cold-smearing method,[89] where the broadening function takes the form of

$$\tilde{\delta}(x) = \frac{2}{\sqrt{\pi}} e^{-\left[x-(1/\sqrt{2})\right]^2} (2-\sqrt{2}\,x). \tag{20}$$

Here, $x = \frac{E_{\mathrm{F}}-\varepsilon}{w}$. In this regard, the occupation numbers $f(\varepsilon_i)$ can be obtained by $\int_{-\infty}^{x_i} \tilde{\delta}(x)dx$. Note that the cold smearing method yields a free energy independent of smearing temperature up to the second order.

C. Geometry relaxation

In geometry optimization under fixed cell conditions, the ionic positions are iteratively adjusted to minimize the total energy until the residual atomic forces are smaller than a specified threshold. The force acting on atom I is defined as the negative gradient of the total energy E_{tot} with respect to its atomic position $\mathbf{R}_I$, and the formula is

$$\mathbf{F}_I = -\partial E_{\mathrm{tot}}/\mathbf{R}_I. \tag{21}$$

This minimization problem can be solved using various optimization algorithms, including the steepest descent (SD), the conjugate gradient (CG), the Broyden–Fletcher–Goldfarb–Shanno (BFGS),[90] and the Fast Inertial Relaxation Engine (FIRE)[91] methods. At each iteration step, the atomic positions are updated according to

$$\mathbf{R}_I^{n+1} = \mathbf{R}_I^n + \alpha \mathbf{D}_I^n, \tag{22}$$

where $\mathbf{D}_I$ represents the optimization direction, α is the step length, and n denotes the index of the geometry relaxation step.

Furthermore, when the cell is allowed to relax, the stress tensor $\sigma_{\alpha\beta}$ is computed as

$$\sigma_{\alpha\beta} = -\frac{1}{\Omega}\frac{\partial E_{\mathrm{tot}}}{\partial \varepsilon_{\alpha\beta}}, \tag{23}$$

where Ω denotes the cell volume and $\varepsilon_{\alpha\beta}$ is the strain tensor components. Next, different geometry relaxation strategies can be

employed. For example, one approach to perform cell relaxation consists of two sequential optimization stages. First, optimizing atomic positions with lattice vectors held fixed, followed by adjusting lattice vectors while keeping ionic positions constant. An alternative strategy involves optimization of both atomic positions and lattice vectors at the same time. This simultaneous refinement allows for dynamic coupling between atomic rearrangements and lattice deformation, potentially accelerating convergence to the equilibrium structure. The geometry optimization methods implemented in ABACUS have been applied to study alloys,[92] interfaces,[93] slabs,[94] low-dimensional materials,[95,96] etc.

D. Molecular dynamics

By solving Newton's equations of motion for each atom in the system, molecular dynamics (MD) simulations numerically integrate atomic forces over a small time step to trace the positions of atoms. In this regard, MD simulations offer a robust framework for investigating the temporal evolution of atomic systems, facilitating the study of a wide range of phenomena such as phase transitions, diffusion processes, chemical reactions, and material properties.

Central to MD simulations is the potential energy surface (PES), which describes atomic interactions and can be derived through various methods. Quantum mechanical (QM) approaches such as density functional theory (DFT) can provide high-accuracy PES calculations but are computationally intensive. Alternatively, machine learning potentials[32,97] offer a balance between accuracy and efficiency by learning the PES from DFT training data, enabling simulations of larger systems or longer timescales. Although classical MD methods enable rapid PES evaluations for systems, their reliance on empirical force fields (such as the Lennard-Jones potential[98,99]) results in lower accuracy compared to the other two approaches.

Once the PES is established, atomic forces are computed via gradients of the total energy with respect to atomic positions, which are then integrated over time to predict atomic trajectories. The velocity Verlet algorithm,[100] a widely used integration scheme that ensures long-term stability, updates atomic positions $\mathbf{r}(t + \Delta t)$ and velocities $\mathbf{v}(t + \Delta t)$ in discrete time steps Δt.

MD simulations can be performed under various statistical ensembles, each imposing different constraints to model specific experimental conditions. ABACUS supports the following ensembles: First, the NVE (microcanonical) ensemble conserves particle number N, volume V, and total energy E, simulating isolated systems where energy exchange with the environment is negligible. Second, for simulations requiring constant temperature T, the NVT (canonical) ensemble[101] employs thermostats such as velocity rescaling, a straightforward but non-equilibrium approach, or the Nosé–Hoover chain method,[102–104] which rigorously incorporates auxiliary degrees of freedom to maintain temperature via Hamiltonian dynamics. The Anderson thermostat[105] couples the system to a heat bath that imposes the desired temperature to simulate the NVT ensemble. The coupling to a heat bath is represented by a stochastic collision that occasionally acts on randomly selected particles. The Berendsen thermostat[106] rescales the velocities of atoms at each step to reset the temperature of a group of atoms. In addition, the Langevin dynamics[107] couples the system to a heat bath through stochastic and frictional forces, ensuring that the system reaches and maintains the desired temperature over time, mimicking conditions where the system exchanges energy with its environment. Third, the NPT (isothermal–isobaric) ensemble maintains constant pressure P and temperature T using barostats such as Parrinello–Rahman.

In addition to the above methods, ABACUS also supports the multi-scale shock technique (MSST),[108] enabling the simulation of shock wave propagation in materials, thereby extending the range of accessible timescales for investigating shock phenomena within such non-equilibrium frameworks.

Born–Oppenheimer Molecular Dynamics (BOMD) decouples the motion of nuclei and electrons and treats nuclei as classical particles moving on a PES that is instantaneously determined by the electronic structure. As an *ab initio* method, BOMD relies on explicit electronic structure calculations and has been implemented in ABACUS. Here, we list some applications.[109–114] Liu *et al.*[110] employed the BOMD simulations to predict the diffusion coefficients of deuterium in liquid Sn over a temperature range of 573–1673 K. Figure 5(a) shows the diffusion coefficients of deuterium in a liquid Sn cell consisting of 216 atoms at five temperatures between 573 and 1673 K. These simulations reveal that deuterium diffuses through liquid Sn more rapidly than Sn atoms diffuse within themselves. Figure 5(b) depicts the effects of deuterium concentration on the diffusion rates of both deuterium and Sn at 1073 K. The findings suggest that Sn's structural and dynamic characteristics remain largely unaffected by the presence of deuterium for the tested temperatures and concentrations.

Chen *et al.*[109] combined stochastic density functional theory (sDFT) with BOMD to explore warm dense matter systems at temperatures ranging from several tens of eV to 1000 eV. They also trained machine-learning-based interatomic models using the first-principles data and employed these models to examine large systems via BOMD simulations. Furthermore, they evaluated the structural

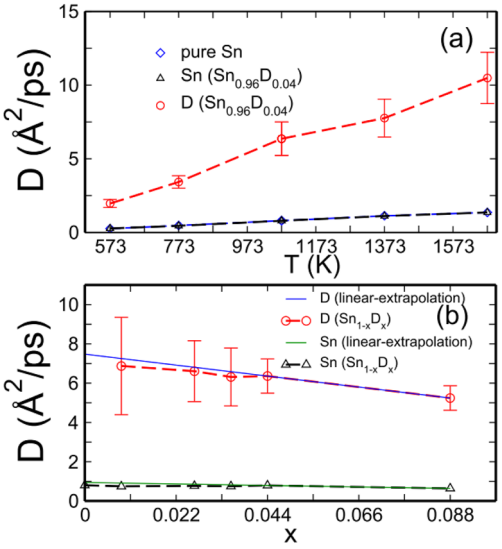

FIG. 5. (a) Diffusion coefficients of D in liquid $Sn_{0.96}D_{0.04}$, Sn in $Sn_{0.96}D_{0.04}$, and Sn in pure liquid Sn as a function of temperature. (b) Diffusion coefficients of D and Sn in liquid $Sn_{1-x}D_x$ at 1073 K with x being 0.009, 0.027, 0.036, 0.044, and 0.085. Adapted with permission from Liu *et al.*, J. Chem. Phys. **147**, 064505 (2017). Copyright 2017 AIP Publishing LLC.

and dynamic characteristics, as well as the transport coefficients, of warm dense matter. Figure 6 shows the radial distribution functions (RDFs) $g(r)$ of warm dense B with a density of 2.46 g/cm^3 at 86 and 350 eV, and the sDFT results are in excellent agreement with those obtained from extended first-principles molecular dynamics (Ext-FPMD).[115,116]

Ma *et al.*[120] combine the *ab initio* molecular dynamics (AIMD) and finite-temperature orbital-free DFT (FT-OFDFT) with the theoretical formalism of Xu-Wang-Ma (XWM) nonlocal free energy functional (XWMF) to study a variety of warm dense matter systems such as the Si, Al, H, He, and H–He mixtures. The KS-DFT calculations were performed using ABACUS, while the OF-DFT calculations were carried out with ATLAS.[121] The XWMF functional is expected to be a good choice for the realistic simulations of warm dense matter systems covering a broad range of temperatures and pressures.

E. Implicit solvation model

Electrochemical reactions, which refer to potential-driven processes at electrode/solvent interfaces, play a pivotal role in advancing green-energy technologies for clean fuel production. A fundamental understanding of the atomic-scale structure and physicochemical properties of these interfaces is indispensable for the rational design and optimization of electrochemical systems. Atomic-scale computational simulations have emerged as a powerful tool for elucidating the complex nature of electrochemical interfaces. However, theoretical modeling at the molecular level faces substantial challenges, such as solvent layers, electrical double layers, and variations in electron numbers at electrode–solvent interfaces, among others.

To address these challenges, we implement a combined approach incorporating (i) an implicit solvation model to approximate solvent effects, (ii) a dipole correction scheme to mitigate spurious electrostatic interactions, and (iii) a compensating charge plate to maintain charge neutrality. As illustrated in Fig. 7, these methodological components are integrated into the SCF workflow of ABACUS, where the potential of the implicit solvent V_{sol}, the compensating charge V_{comp}, and the dipole correction V_{dip} is included in iterative electron density and total energy calculations. This integrated approach enables more realistic simulations of electrochemical systems while maintaining computational efficiency.

Solid–liquid interfaces are ubiquitous and are frequently encountered and employed in electrochemical simulations. To accurately model such systems, it is important to consider the solvation effect. The implicit solvation model is a well-developed method to deal with solvation effects and is widely used in both finite and periodic systems. This approach treats the solvent as a continuous medium rather than as individual "explicit" solvent molecules,

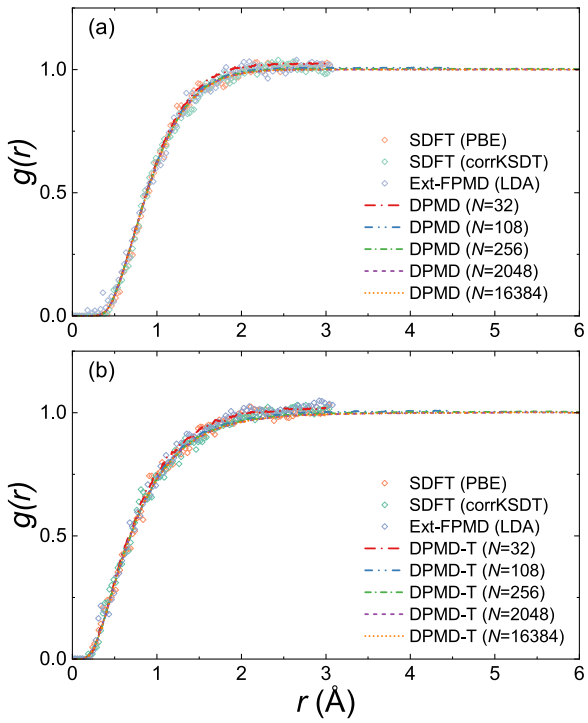

FIG. 6. Radial distribution functions (RDFs) $g(r)$ for B systems at a density of 2.46 g/cm^3 and the temperatures are (a) 86 eV and (b) 350 eV. Some of the $g(r)$ are derived from Ext-FPMD,[117] as well as the sDFT calculations, which employed the PBE[61] and corrKSDT[118] XC functionals. The number of B atoms is set to 32 in AIMD simulations. In addition, DPMD denotes the model trained by the traditional DP method,[32] whereas DPMD-T indicates the TDDP method applied to model training as reported by Zhang *et al.*[119] N is the number of B atoms in a cell. Adapted with permission from Chen *et al.*, Matter Radiat. Extremes **9**, 015604 (2024). Copyright 2024 AIP Publishing LLC.

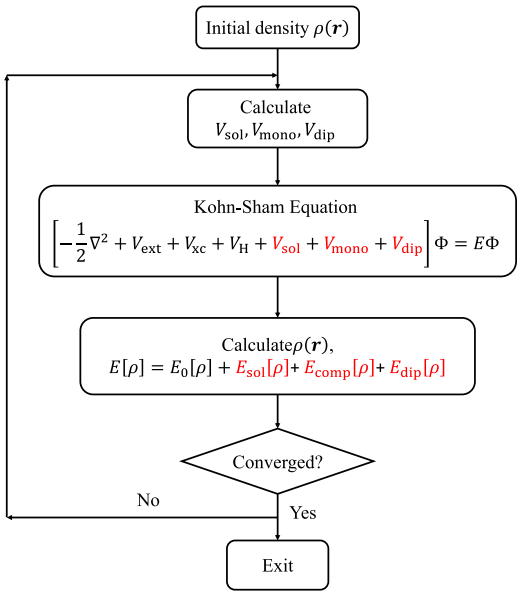

FIG. 7. Implementation of the implicit solvation model in ABACUS. The self-consistent loop of solving the KS equation starts with an initial charge density $\rho(\mathbf{r})$, followed by the evaluation of correction potentials, including the implicit solvent potential V_{sol}, the compensating charge potential V_{comp}, and the dipole correction potential V_{dip}. These corrections are subsequently applied to the KS equations for iterative electron density and total energy calculations, where $E_0[\rho]$ denotes the energy without corrections.

which means that the solute embedded in an implicit solvent and the average over the solvent degrees of freedom becomes implicit in the properties of the solvent bath.

We place the solute in a cavity surrounded by a continuum dielectric medium characterized by the relative permittivity of the solvent, as employed in a previous work.[122] We describe the dielectric response in terms of the solute's electron density, considering the polarization of solvents in response to the electronic structures of the solute, the effects of cavitation and dispersion, and the reaction of the solute system to the presence of the solvent.

We determine the form of the dielectric cavity in the solvent by assuming a diffuse cavity that is a local functional of the electron density $\rho(\mathbf{r})$ of the solute, which satisfies the following functional dependence:

$$\varepsilon(\rho) = 1 + (\varepsilon_b - 1)S(\rho), \tag{24}$$

where ε_b is the relative permittivity of the bulk solvent and $S(\rho)$ is the cavity shape function, given by[123]

$$S(\rho) = \frac{1}{2}\mathrm{erfc}\left[\frac{\ln\left(\frac{\rho}{\rho_c}\right)}{\sqrt{2}b}\right]. \tag{25}$$

The parameter ρ_c is the charge density cutoff, defining the electron density at which the dielectric cavity forms. The parameter b determines the width of the diffuse cavity. This assumption leads to a smooth variation of the relative permittivity from $\varepsilon(\mathbf{r}) = 1$ of the solute to ε_b in the solvent.

The conjugate gradient method is used to solve the generalized Poisson equation,

$$\nabla \cdot [\varepsilon(\rho)\nabla\phi(\mathbf{r})] = -4\pi[N(\mathbf{r}) - \rho(\mathbf{r})], \tag{26}$$

where $\phi(\mathbf{r})$ is the electrostatic potential due to the electron density $\rho(\mathbf{r})$ and nuclear charge density $N(\mathbf{r})$ of the solute system in a polarizable medium.

The typical Kohn–Sham Hamiltonian consists of two additional terms in the local part of the potential. One of them is the electrostatic correction caused by the induced charge,[122]

$$V_{\mathrm{el}} = -\frac{d\varepsilon(\rho)}{d\rho}\frac{|\nabla\phi|^2}{8\pi}, \tag{27}$$

and the other term is the cavity potential, which describes the cavitation, dispersion, and repulsion interaction between the solute and the solvent that is not captured by the electrostatic terms alone,[122]

$$V_{\mathrm{cav}} = \tau\frac{d|\nabla S|}{d\rho}, \tag{28}$$

where τ is the effective surface tension parameter. The two corrections [Eqs. (27) and (28)] are collectively referred to as the implicit solvent-induced potential term V_{sol}, while the energy correction terms are

$$E_{\mathrm{el}} = -\frac{1}{8\pi}\int \varepsilon(\rho)|\nabla\varphi|^2 \mathrm{d}\mathbf{r}, \tag{29}$$

$$E_{\mathrm{cav}} = \tau\int |\nabla S|\mathrm{d}\mathbf{r}. \tag{30}$$

We benchmark the accuracy of the implicit solvation implementation by calculating molecular solvation energies E_{sol}, which is defined as the total energy difference between a solvated condition and a vacuum condition in ABACUS, and comparing them against VASPsol-calculated values.[124] We can see from Fig. 8 that the solvation energies from ABACUS agree well with those produced by the VASPsol package. The minor discrepancies between the solvation energies computed by the two methods may be attributed to the pseudopotential difference. Note that we use projector-augmented-wave (PAW) potentials in VASPsol and the norm-conserving pseudopotentials in ABACUS.

ABACUS also supports adding dipole correction and compensating charge when modeling surfaces, which were utilized in a recent work.[125] The periodic boundary conditions imposed on the electrostatic potential create an artificial electric field across a slab. By introducing an isolated slab-shaped density distribution $\rho(\mathbf{r})$ that is normal to the z-axis, a dipole correction[126] is added to the bare ionic potential to compensate for the artificial dipole field within the context of periodic supercell calculations.

Modeling a constant-potential electrochemical surface reaction requires the adjustment of electron numbers in a simulation cell. Simultaneously, we must preserve the supercell's neutrality under the periodic boundary conditions. Thus, a distribution of compensating charge needs to be implemented in the vacuum region of surface models when extra electrons are added to or extracted from the system. The compensating charge implemented in ABACUS follows the methodology developed by Brumme *et al.*[127] We assume that the monopole with a total charge of $-n_{\mathrm{dop}}$ per unit cell is located at z_{mono} along the z axis. In this case, the effective potential $V_{\mathrm{mono}}(\mathbf{r})$ is added to the Hamiltonian, and the additional term E_{mono} is included in the total energy. Since $V_{\mathrm{mono}}(\mathbf{r})$ is independent of the electron density, it is unnecessary to update in a self-consistent manner. We also implemented the correction on the ionic forces induced by the presence of the monopole, allowing for calculating the electronic structure and complete structural relaxation in the field-effect configuration.

We output the electrostatic energy of an electron along the z direction perpendicular to the Pt surface for a testing system with

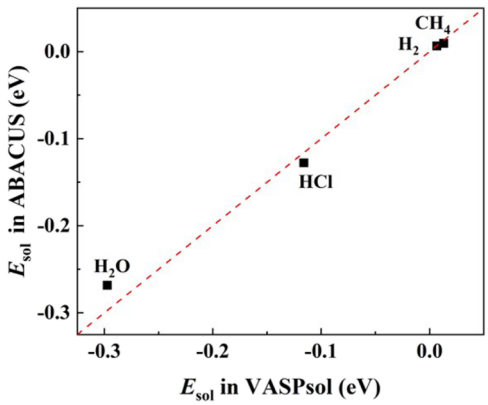

FIG. 8. Solvation energies E_{sol} (the total energy difference between a solvated condition and a vacuum condition) calculated by VASPsol and ABACUS for H_2O, HCl, H_2, and CH_4 systems.

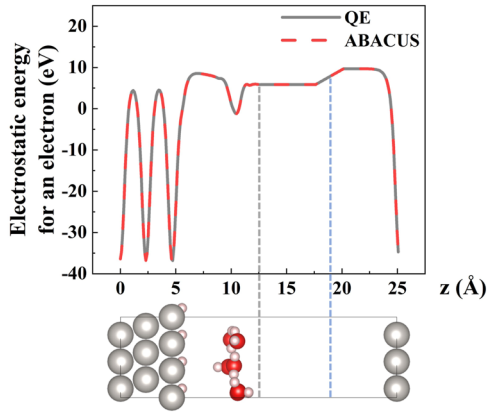

FIG. 9. Electrostatic energy of an electron along the z direction perpendicular to the Pt surface calculated by Quantum ESPRESSO and ABACUS.[125] The gray vertical dashed line represents the position of the compensating charge plate, while the blue dashed line corresponds to the dipole correction. A schematic structure plot of the testing interface model is aligned below the average electrostatic energy curves. Gray, red, and white spheres correspond to the platinum, oxygen, and hydrogen atoms, respectively.

an added electron number $N_e^{\text{extra}} = 0.2$ in the simulation cell. The testing system is a (3 × 3) Pt (111) surface slab composed of three atomic layers, as illustrated in Fig. 9. The modeled electrode surface contains 27 Pt atoms, with a monolayer of hydrogen coverage and six explicit water molecules. We place a compensating charge plate in the vacuum region above the water layer, and a dipole correction is also included in DFT calculations. Figure 9 shows that the electrostatic energy results from ABACUS are in perfect agreement with those computed from Quantum ESPRESSO.[14]

III. METHODS IN PLANE WAVE BASIS

A. Kohn–Sham equation in plane wave basis

In the atomic system with periodic boundary conditions, the electronic wave functions can be expanded with the plane waves, which take the form of

$$\psi_{n\mathbf{k}}(\mathbf{r}) = \sum_{\mathbf{G}} c_{n\mathbf{k}}(\mathbf{G}) e^{i(\mathbf{k}+\mathbf{G})\cdot\mathbf{r}}, \tag{31}$$

where $\mathbf{G}$ and $\mathbf{k}$, respectively, represent the wave vectors of plane waves and sampling points in the Brillouin zone, n denotes the band index, and $\{c_{n\mathbf{k}}(\mathbf{G})\}$ are the expansion coefficients of the plane wave basis. The k-point sampling method is typically employed as the Monkhorst–Pack scheme.[128] Next, the Kohn–Sham equation described with the plane wave basis can be written as

$$\sum_{\mathbf{G}'} \left[\frac{1}{2}(\mathbf{k}+\mathbf{G})^2 \delta_{\mathbf{G}\mathbf{G}'} + \hat{V}_{\text{KS}}(\mathbf{G}-\mathbf{G}')\right] c_{n\mathbf{k}}(\mathbf{G}') = \varepsilon_{nk} c_{n\mathbf{k}}(\mathbf{G}), \tag{32}$$

where $\hat{V}_{\text{KS}}(\mathbf{G}-\mathbf{G}')$ is the plane wave representation of the Kohn–Sham potential $\hat{V}_{\text{KS}}$, ε_{nk} is the eigenvalue of the Kohn–Sham equation, and $\delta_{\mathbf{G}\mathbf{G}'}$ is the Kronecker delta function. In this regard, the total energy can be calculated as

$$E_{\text{tot}} = \sum_{n\mathbf{k}} f(\varepsilon_{n\mathbf{k}})\varepsilon_{n\mathbf{k}} - \frac{1}{2}\iint \frac{\rho(\mathbf{r})\rho(\mathbf{r}')}{|\mathbf{r}-\mathbf{r}'|}\mathrm{d}\mathbf{r}\mathrm{d}\mathbf{r}' - \int V_{\text{xc}}(\mathbf{r})\rho(\mathbf{r})\mathrm{d}\mathbf{r} + E_{\text{xc}}[\rho(\mathbf{r})] + E_{\text{II}}, \tag{33}$$

where $f(\varepsilon_{n\mathbf{k}})$ is the Fermi–Dirac distribution function, $\rho(\mathbf{r})$ is the electron density, V_{xc} is the exchange–correlation potential, E_{xc} is the exchange–correlation energy, and E_{II} is the ionic energy calculated by the Ewald method.[129]

According to the Hellmann–Feynman theorem,[130,131] the force acting on atom I is defined as Eq. (21) and the stress is defined as Eq. (23). Consequently, when including a non-local part in the norm-conserving pseudopotential, the force acting on atom I of type τ can be divided into three parts, namely,

$$\mathbf{F}_I = \mathbf{F}_I^{\text{Ewald}} + \mathbf{F}_I^{\text{L}} + \mathbf{F}_I^{\text{NL}}, \tag{34}$$

where $\mathbf{F}_I^{\text{Ewald}}$ is the Ewald force. $\mathbf{F}_I^{\text{L}}$ is the force contributed by the local part of the pseudopotential, and $\mathbf{F}_I^{\text{NL}}$ is from the non-local part. The local potential term is given by

$$\mathbf{F}_I^{\text{L}} = -i\Omega \sum_{\mathbf{G}\neq\mathbf{0}} \mathbf{G} e^{i\mathbf{G}\cdot\mathbf{R}_I} v_\tau^{\text{L}}(\mathbf{G})\rho^*(\mathbf{G}), \tag{35}$$

where Ω is the cell volume and v_τ^{L} is the local potential of atom type τ. Moreover, $\rho(\mathbf{G})$ is the electron density in the plane wave basis, which is computed as

$$\rho(\mathbf{G}) = \frac{1}{\Omega}\int \rho(\mathbf{r}) e^{-i\mathbf{G}\cdot\mathbf{r}}\mathrm{d}\mathbf{r}. \tag{36}$$

Furthermore, the non-local potential term is written as

$$\mathbf{F}_I^{\text{NL}} = -2i \sum_{n\mathbf{k}\mathbf{G}\mathbf{G}'} f(\varepsilon_{n\mathbf{k}}) c_{n\mathbf{k}}^*(\mathbf{G}) c_{n\mathbf{k}}(\mathbf{G}') \times \left[e^{i(\mathbf{G}'-\mathbf{G})\cdot\mathbf{R}_I}(\mathbf{G}'-\mathbf{G}) v_\tau^{\text{NL}}(\mathbf{k}+\mathbf{G}, \mathbf{k}+\mathbf{G}')\right], \tag{37}$$

where v_τ^{NL} is the nonlocal potential of atom type τ.

The stress tensor is decomposed into the Ewald term $\sigma_{\alpha\beta}^{\text{Ewald}}$, the Hartree term $\sigma_{\alpha\beta}^{\text{H}}$, the exchange–correlation term $\sigma_{\alpha\beta}^{\text{xc}}$, the kinetic energy term $\sigma_{\alpha\beta}^{\text{T}}$, the local pseudopotential term $\sigma_{\alpha\beta}^{\text{L}}$, and the non-local pseudopotential term $\sigma_{\alpha\beta}^{\text{NL}}$, expressed as

$$\sigma_{\alpha\beta} = \sigma_{\alpha\beta}^{\text{Ewald}} + \sigma_{\alpha\beta}^{\text{Hartree}} + \sigma_{\alpha\beta}^{\text{xc}} + \sigma_{\alpha\beta}^{\text{T}} + \sigma_{\alpha\beta}^{\text{L}} + \sigma_{\alpha\beta}^{\text{NL}}. \tag{38}$$

The formulas of the terms can be found in Ref. 27.

B. Iterative diagonalization methods

The Kohn–Sham (KS) equations, when expanded in a plane wave basis, are typically solved using iterative diagonalization techniques such as the Conjugate Gradient (CG) and Davidson methods. For example, Fig. 10 shows the CG algorithm for solving the Kohn–Sham equations, where the input wave functions $\{\psi_i\}$ are iteratively updated to satisfy orthogonality conditions and to approximate the eigenfunctions of the given Hamiltonian matrix. Regarding the Hamiltonian matrix, it generally includes electron kinetic energy terms, the effective potential, and non-local pseudopotential terms. Importantly, the $\mathrm{H}\psi_i$ operation that involves

for $i = 1$ **to** n **do**
  $\psi_i = (I - \sum_{j<i} |\psi_j\rangle\langle\psi_j|)\psi_i$
  $\psi_i = \frac{\psi_i}{\|\psi_i\|}$
  $p_i = H\psi_i$
  $\lambda_i = \langle\psi_i|p_i\rangle$
  $k = 1$
  while $k \leq k_{maxiter}$ **and** *convergence not reached* **do**
    $g_i = K(p_i - \lambda\psi_i)$
    $g_i = (I - \sum_{j\leq i} |\psi_j\rangle\langle\psi_j|)g_i$
    if $k = 1$ **then**
      $d_i^k = g_i$
    else
      $d_i^k = g_i + \gamma d_i^{k-1}$
    end if
    $d_i^k = \frac{d_i^k}{\|d_i^k\|}$
    $h_i = Hd_i^k$
    $\psi_i = \psi_i\cos\theta + d_i^k\sin\theta$
    $p_i = p_i\cos\theta + h_i\sin\theta$
    $\lambda_i = \langle\psi_i|p_i\rangle$
  end while
end for

FIG. 10. Preconditioned conjugate gradient algorithm for $H\psi_i = \lambda\psi_i$, where $i = 1, \ldots, n$ is the band index. Here, ψ_i is the N-dimensional wave function, and H stands for the $N \times N$ Hamiltonian. A preconditioner K is applied to the residual $H\psi_i - \lambda\psi_i$ to obtain a preconditioned gradient g_i, which is then used to construct an improved search direction d_i by the Polak–Ribière method.[132] Next, the new ψ_i and λ_i are obtained.[133] Here, γ controls the conjugacy of the search directions, leveraging the algorithm's history for optimal convergence. θ acts as an optimal step size, ensuring maximal energy reduction at each iteration.

the multiplication of the Hamiltonian matrix with the electronic wave function ψ_i is computationally expensive because mathematical operations such as Fast Fourier transforms (FFTs) and Basic Linear Algebra Subprograms (BLAS) operations are needed.

In general, diagonalization of the Hamiltonian matrix is the most computationally intensive step in most KS-DFT calculations. Therefore, the development of efficient diagonalization algorithms optimized for high-performance computing (HPC) architectures is essential. In particular, recent advances in heterogeneous computing platforms have substantially accelerated scientific computations, particularly in computational chemistry and materials science.[14,134,135] In some cases, the plane wave basis set is capable of dealing with systems consisting of thousands of atoms or more.[136–140]

ABACUS employs a unified framework that operates seamlessly across diverse hardware architectures. Key linear algebra operations, such as generalized matrix-vector multiplication (`gemv`) and vector division (`vecdiv`), are encapsulated within a platform-agnostic interface, supporting execution on platforms such as central processing unit (CPU), graphics processing unit (GPU), and deep computing unit (DCU). Consequently, the algorithm achieves high computational efficiency across multiple platforms. To evaluate the efficiency of heterogeneous acceleration in ABACUS, we conducted SCF calculations using plane wave basis sets on the Bohrium cloud platform,[141] comparing CPU and DCU performance at equivalent computational costs. The Davidson method was selected for these benchmarks due to its demonstrated superiority in convergence speed compared to conjugate gradient approaches. Our analysis reveals a clear scaling relationship between system size and acceleration performance, with DCU computations achieving up to fivefold speedup for systems containing ~50 atoms, as illustrated in Fig. 11. This performance improvement grows increasingly pronounced in larger systems, underscoring the effectiveness of our heterogeneous computing framework.

C. Stochastic DFT

1. Formulas

The stochastic density functional theory (sDFT)[143] was proposed to circumvent the $O(N^3)$ scaling of KS-DFT calculations. In particular, by introducing stochastic orbitals and the Chebyshev expansion scheme in the sDFT method, the electron density can be evaluated by tracing operators, bypassing the diagonalization of the Hamiltonian. Since the computational costs of tracing operations scale linearly with system size, this approach significantly enhances computational efficiency for large systems. Later, the finite-temperature sDFT[144] defines the Fermi–Dirac operator at finite temperature as

$$\hat{f}_H = \frac{1}{1 + \exp\left(\frac{\hat{H} - E_\mu}{k_B T}\right)}, \tag{39}$$

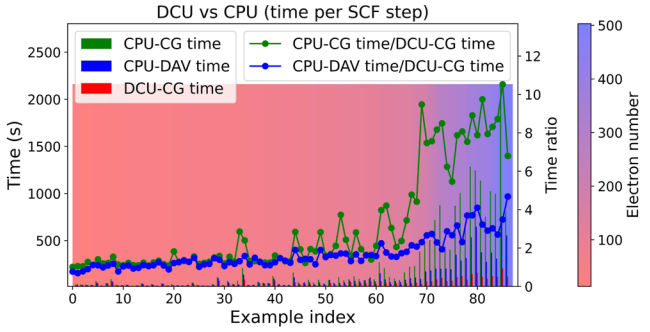

FIG. 11. Computation time per SCF step for a collection of examples (with different numbers of electrons) by using the conjugate gradient (CG) method on DCU (red), the Davidson (DAV) method on CPU (blue), and the CG method on CPU (green), respectively. The line chart shows their ratio. The examples are available from the link.[142] The hardware is `c32_m64` for CPU calculations and `4*DCU` for DCU calculations.

where $\hat{H}$ is the KS Hamiltonian operator and E_μ represents the chemical potential. In fact, the order of expansion decreases with increasing temperature, thereby enhancing the computational efficiency of sDFT at high temperatures.

In sDFT, the electron density is directly computed using the Hamiltonian operator as

$$\rho(\mathbf{r}) = 2\mathrm{Tr}\left[\hat{f}_H \delta(\hat{\mathbf{r}} - \mathbf{r})\right], \tag{40}$$

where the chemical potential in $\hat{f}_H$ is determined by solving the conservation of electron number via

$$N = \mathrm{Tr}\left[\hat{f}_{H\mu}\right]. \tag{41}$$

By adopting the self-consistent field method, the electron density can be self-consistently computed. The total energy can similarly be computed via

$$E_{\mathrm{tot}} = 2\mathrm{Tr}\left[\hat{f}_H \hat{H}\right] - \frac{1}{2}\iint \frac{\rho(\mathbf{r})\rho(\mathbf{r}')}{|\mathbf{r} - \mathbf{r}'|}\mathrm{d}\mathbf{r}\mathrm{d}\mathbf{r}' - \int V_{\mathrm{xc}}(\mathbf{r})\rho(\mathbf{r})\mathrm{d}\mathbf{r} + E_{\mathrm{xc}}[\rho(\mathbf{r})] + E_{\mathrm{II}}. \tag{42}$$

The entropy is similarly formulated as

$$S = -2k_B\mathrm{Tr}\left[\hat{f}_H \ln \hat{f}_H + (1 - \hat{f}_H)\ln(1 - \hat{f}_H)\right]. \tag{43}$$

However, the use of stochastic orbitals inevitably introduces stochastic errors. To achieve higher accuracy, a large number of stochastic orbitals are typically required, which substantially increases the computational time despite its linear scaling property. For instance, fragmentation approaches have been developed to compute molecular systems[145] and covalent materials,[146,147] while stochastic "embedding" methods have been used to calculate *p*-nitroaniline in water.[148] In addition, the energy window method proposed by Chen *et al.*[149] decomposes the electron density into different components based on orbital energies to reduce stochastic errors, demonstrating good generality and robustness.

For simulations of materials at extremely high temperatures, mixed stochastic-deterministic Density Functional Theory (mDFT) was proposed.[150] The method combines the advantages of traditional KS-DFT and sDFT. The mDFT method retains the computational efficiency of sDFT for high-temperature systems while reducing stochastic errors using some of the deterministic Kohn–Sham orbitals.

2. Stochastic orbitals

In detail, the sDFT defines a set of stochastic orbitals. For any orthogonal complete basis $\{\phi_j\}$, the stochastic orbitals $\{\chi_a\}$ are defined as

$$\langle\phi_j|\chi_a\rangle = \frac{1}{\sqrt{N_\chi}}\exp\left(i2\pi\theta_j^a\right), \tag{44}$$

where $\{\theta_j^a\}$ are stochastic numbers uniformly distributed over (0,1), and N_χ is the number of stochastic orbitals. In addition, stochastic orbitals can also be defined[147,149,151,152] as

$$\langle\phi_j|\chi_a\rangle = \pm\frac{1}{\sqrt{N_\chi}}, \tag{45}$$

each with a probability of 1/2. Notably, Baer *et al.*[153] demonstrated that both definitions yield the same expected values and similar variance for Hermitian matrices with comparable magnitudes of real and imaginary parts. As $N_\chi \to +\infty$, the stochastic orbitals form a complete basis with the relation of

$$\lim_{N_\chi\to+\infty}\sum_{a=1}^{N_\chi}\langle\phi_i|\chi_a\rangle\langle\chi_a|\phi_j\rangle = \delta_{ij} \tag{46}$$

and

$$\lim_{N_\chi\to+\infty}\sum_{a=1}^{N_\chi}|\chi_a\rangle\langle\chi_a| = \hat{I}. \tag{47}$$

To enhance the accuracy of stochastic orbitals, mDFT introduces a set of deterministic, orthogonal but not complete Kohn–Sham orbitals φ_i, along with stochastic orbitals $\tilde{\chi}_a$, where the stochastic orbitals are required to be orthogonal to the deterministic ones

$$|\tilde{\chi}_a\rangle = |\chi_a\rangle - \sum_{i=1}^{N_\varphi}\langle\varphi_i|\chi_a\rangle|\varphi_i\rangle, \tag{48}$$

where N_φ is the number of deterministic orbitals. The mixed orbitals composed of deterministic and orthogonal stochastic orbitals also form a complete basis set as

$$\lim_{N_\chi\to+\infty}\sum_{a=1}^{N_\chi}|\tilde{\chi}_a\rangle\langle\tilde{\chi}_a| + \sum_{i=1}^{N_\varphi}|\varphi_i\rangle\langle\varphi_i| = \hat{I}. \tag{49}$$

Therefore, the trace of any operator $\hat{O}$ is given by

$$\mathrm{Tr}\left[\hat{O}\right] = \lim_{N_\chi\to+\infty}\sum_{a=1}^{N_\chi}\langle\tilde{\chi}_a|\hat{O}|\tilde{\chi}_a\rangle + \sum_{i=1}^{N_\varphi}\langle\varphi_i|\hat{O}|\varphi_i\rangle. \tag{50}$$

For example, the formula for electron density in mDFT is

$$\rho(\mathbf{r}) \approx 2\sum_{a=1}^{N_\chi}\left|\left\langle\tilde{\chi}_a\middle|\hat{f}_H^{1/2}\middle|\mathbf{r}\right\rangle\right|^2 + 2\sum_{i=1}^{N_\varphi}f(\varepsilon_i)|\psi_i(\mathbf{r})|^2. \tag{51}$$

Note that here we use a finite number of stochastic orbitals N_χ, which introduces some stochastic errors.

3. Plane wave-based implementation

We have implemented the sDFT and mDFT methods based on plane wave basis[27] and periodic boundary conditions in ABACUS. Furthermore, both methods can be used with the *k*-point sampling method. The flow chart of sDFT and mDFT is shown in Fig. 12.

The stochastic orbitals based on the plane wave basis can be defined as

$$|\chi_{a\mathbf{k}}\rangle = \frac{1}{\sqrt{N_\chi}}\sum_{\mathbf{G}}\exp\left(i2\pi\theta_{\mathbf{k},\mathbf{G}}^a\right)|\mathbf{k}+\mathbf{G}\rangle, \tag{52}$$

where $\theta_{\mathbf{k},\mathbf{G}}^a$ are the independent stochastic numbers uniformly distributed in (0,1), and N_χ is the number of stochastic orbitals. In addition to the sum of stochastic orbitals, the sum of **k**-points should

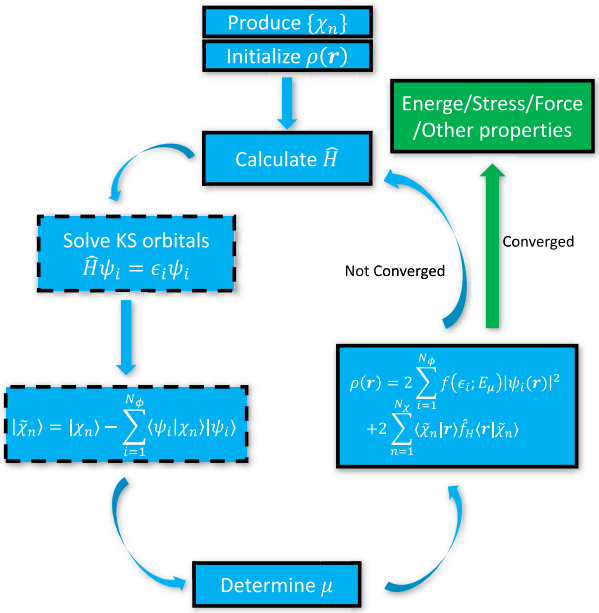

FIG. 12. Flow chart of stochastic DFT in ABACUS. When the number of KS orbitals N_ϕ is larger than 0, it is the flow chart of mixed stochastic-deterministic DFT. When the number of KS orbitals N_ϕ reduces to 0, indicating that the dashed box does not exist, it degenerates into the flow chart of sDFT. The chemical potential is μ.

also be done. In plane wave-based sDFT, the electron density can be computed as

$$\rho(\mathbf{r}) = 2\sum_{\mathbf{k}} W(\mathbf{k})\sum_{a\mathbf{G}}\left|\langle\mathbf{r}|\mathbf{k}+\mathbf{G}\rangle\left\langle\mathbf{k}+\mathbf{G}\middle|\hat{f}_H^{1/2}\middle|\chi_{a\mathbf{k}}\right\rangle\right|^2. \tag{53}$$

Let us define

$$\gamma_{a\mathbf{k}}(\mathbf{G}) = \left\langle\mathbf{k}+\mathbf{G}\middle|\hat{f}_H^{1/2}\middle|\chi_{a\mathbf{k}}\right\rangle, \tag{54}$$

so the electron density can be written as

$$\rho(\mathbf{r}) = 2\sum_{\mathbf{k}} W(\mathbf{k})\sum_{a\mathbf{G}}\left|\gamma_{a\mathbf{k}}(\mathbf{G})e^{i(\mathbf{k}+\mathbf{G})\cdot\mathbf{r}}\right|^2. \tag{55}$$

For the atomic forces, only the nonlocal potential part is different from the traditional Kohn–Sham method, which is given by

$$\begin{aligned}\mathbf{F}_I^{\mathrm{NL}} &= 2\mathrm{Tr}\left[-i\hat{f}_H\sum_{\mathbf{GG}'}(\mathbf{G}'-\mathbf{G})e^{i(\mathbf{G}'-\mathbf{G})\cdot\mathbf{R}_I}\right.\\ &\left.\times\, v_\tau^{\mathrm{NL}}(\mathbf{k}+\mathbf{G},\mathbf{k}+\mathbf{G}')|\mathbf{k}+\mathbf{G}\rangle\langle\mathbf{k}+\mathbf{G}'|\right]\\ &= -2i\sum_{\mathbf{k}} W(\mathbf{k})\sum_{a\mathbf{GG}'}\gamma_{a\mathbf{k}}(\mathbf{G})\gamma_{a\mathbf{k}}(\mathbf{G}')\\ &\times(\mathbf{G}'-\mathbf{G})e^{i(\mathbf{G}'-\mathbf{G})\cdot\mathbf{R}_I}v_\tau^{\mathrm{NL}}(\mathbf{k}+\mathbf{G},\mathbf{k}+\mathbf{G}').\end{aligned} \tag{56}$$

In addition, the stress tensor for the kinetic part and the nonlocal part is evaluated differently in sDFT and mDFT when compared to the traditional Kohn–Sham method. In particular, the kinetic part is

$$\begin{aligned}\sigma_{\alpha\beta}^T &= \frac{2}{\Omega}\mathrm{Tr}\left[\hat{f}_H\sum_{\mathbf{GG}'}(\mathbf{k}+\mathbf{G})_\alpha(\mathbf{k}+\mathbf{G}')_\beta|\mathbf{k}+\mathbf{G}\rangle\delta(\mathbf{GG}')\langle\mathbf{k}+\mathbf{G}'|\right]\\ &= \frac{2}{\Omega}\sum_{\mathbf{k}} W(\mathbf{k})\sum_{a\mathbf{GG}'}\gamma_{a\mathbf{k}}(\mathbf{G})(\mathbf{k}+\mathbf{G})_\alpha\delta(\mathbf{GG}')(\mathbf{k}+\mathbf{G}')_\beta\gamma_{a\mathbf{k}}(\mathbf{G}'),\end{aligned} \tag{57}$$

and the nonlocal part takes the form of

$$\begin{aligned}\sigma_{\alpha\beta}^{\mathrm{NL}} &= -\frac{2}{\Omega}\mathrm{Tr}\left[\hat{f}_H\sum_{\mathbf{GG}'\tau}S_\tau(\mathbf{G}'-\mathbf{G})\frac{\partial v_\tau^{\mathrm{NL}}(\mathbf{G}+\mathbf{k},\mathbf{G}'+\mathbf{k})}{\partial\varepsilon_{\alpha\beta}}\right.\\ &\left.\times\,|\mathbf{k}+\mathbf{G}\rangle\langle\mathbf{k}+\mathbf{G}'|\right]\\ &= -\frac{2}{\Omega}\sum_{a\mathbf{GG}'\tau}\gamma_{a\mathbf{k}}(\mathbf{G})S_\tau(\mathbf{G}'-\mathbf{G})\frac{\partial v_\tau^{\mathrm{NL}}(\mathbf{G}+\mathbf{k},\mathbf{G}'+\mathbf{k})}{\partial\varepsilon_{\alpha\beta}}\gamma_{a\mathbf{k}}(\mathbf{G}').\end{aligned} \tag{58}$$

Figure 13(a) shows the parallel efficiency of sDFT and mDFT. sDFT demonstrates excellent scalability, as all stochastic orbitals are independently evaluated, while mDFT involves calculating KS orbitals and additional data communication among CPU cores, reducing its efficiency compared to sDFT. Figure 13(b) compares the operational efficiency at different temperatures by recording the average time per electronic iteration for the sDFT method.

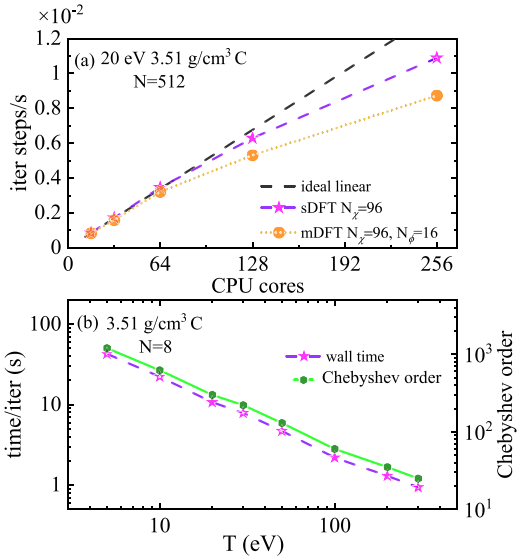

FIG. 13. Efficiency tests of the sDFT and mDFT methods. (a) Parallel efficiency of sDFT and mDFT for a C system with the number of atoms being N = 512 at a temperature of 20 eV. (b) Averaged wall time for an electronic iteration step of the sDFT method when calculating a C system (N = 8) at a temperature range from 5 to 300 eV. The tested machines are Intel(R) Xeon(R) Platinum 9242 CPU at 2.30 GHz nodes.

The temperature ranges from 5 to 300 eV, and 96 stochastic orbitals were adopted. In sDFT, the order of Chebyshev polynomial expansions was selected to ensure an electron error less than 10^{-9}. In particular, for temperatures of 5, 10, 20, 30, 50, 100, 200, and 300 eV, Chebyshev orders of 1200, 620, 300, 220, 130, 60, 35, and 25 were used, respectively. As the temperature increases, the number of Chebyshev orders decreases, causing the wall time to drop exponentially. The sDFT and mDFT methods implemented in ABACUS have been successfully applied to study warm dense matter.[27,109,154]

D. Orbital-free DFT

1. Formulas

An alternative method of KS-DFT is orbital-free density functional theory (OF-DFT),[3,155] which achieves a more affordable computational complexity of $O(N\ln N)$ or $O(N)$ by calculating the non-interacting kinetic energy directly via charge density instead of Kohn–Sham orbitals. In OF-DFT, once the kinetic energy density functional (KEDF) is defined, the total energy is a pure functional of charge density, taking the form of

$$E_{\mathrm{OF}}[\rho] = T_{\mathrm{s}}[\rho] + E_{\mathrm{ext}}[\rho] + E_{\mathrm{H}}[\rho] + E_{\mathrm{xc}}[\rho] + E_{\mathrm{II}}, \tag{59}$$

so that the ground state energy can be obtained by directly minimizing the total energy functional with optimization algorithms,[156] such as the truncated Newton method[157] and the conjugate gradient method.[158,159]

In practice, to guarantee the conservation of electrons, we define a Lagrangian as

$$L_{\mathrm{OF}}[\rho] = E_{\mathrm{OF}}[\rho] - \mu\left(\int \rho(\mathbf{r})\mathrm{d}\mathbf{r} - N\right), \tag{60}$$

where μ is the Lagrangian multiplier and the chemical potential. Then, the minimum of $L_{\mathrm{OF}}[\rho]$ is found by optimizing $\phi(\mathbf{r}) \equiv \sqrt{\rho(\mathbf{r})}$, which guarantees the non-negativity of $\rho(\mathbf{r})$, and the variation of $L_{\mathrm{OF}}[\rho]$ to $\phi(\mathbf{r})$ gives

$$\begin{aligned}\frac{\delta L}{\delta \phi} &= \frac{\delta E_{\mathrm{OF}}[\rho]}{\delta \phi} - 2\mu\phi \\ &= 2(V_s + V_{\mathrm{ext}} + V_{\mathrm{H}} + V_{\mathrm{xc}} - \mu)\phi.\end{aligned} \tag{61}$$

OF-DFT has been implemented in ABACUS using plane wave basis sets. Up to now, there are five available KEDFs in ABACUS, which are Thomas–Fermi (TF),[1,2] von Weizsäcker (vW),[160] TFλvW,[161] Wang–Teter (WT),[162] and Luo–Karasiev–Trickey (LKT)[163] KEDFs. In addition, due to the absence of Kohn–Sham orbitals, the commonly used norm-conserving pseudopotentials are usually unavailable in the field of OF-DFT unless special treatment is used.[164] Therefore, ABACUS employs a local pseudopotential (LPS) instead, supporting types including the bulk-derived (BLPS)[165] and a high-quality local pseudopotential.[166]

2. Kinetic energy density functional

Given that T_s is of comparable magnitude to the total energy, the accuracy of OF-DFT is heavily dependent on the form of the KEDF. Nevertheless, the development of an accurate KEDF has remained a significant challenge in the field of OF-DFT for several decades.

Several analytical KEDFs have been proposed over the past few decades,[155,167] and they can be categorized into two main classes. First, the local and semilocal KEDFs are characterized by their kinetic energy density as a function of the charge density, its gradient, the Laplacian of the charge density, or even higher-order derivatives.[1,2,160,163,168,169] Second, the nonlocal KEDFs define the kinetic energy density at each point in real space as a functional of the nonlocal charge density.[162,170–175] Semilocal KEDFs are generally more computationally efficient, while nonlocal KEDFs tend to provide greater accuracy. However, a universally applicable KEDF that effectively describes both simple metals and semiconductor systems remains largely elusive, and a systematic approach to its development remains to be explored.

Although the exact formula of the non-interacting kinetic energy T_s remains unknown, a rigorous lower bound is provided by the von Weizsäcker (vW) KEDF,[160] which is expressed as

$$T_{\mathrm{vW}} = \frac{1}{8}\int \frac{|\nabla\rho(\mathbf{r})|^2}{\rho\ (\mathbf{r})}\ \mathrm{d}\mathbf{r}. \tag{62}$$

The remaining part of the non-interacting kinetic energy, known as the Pauli energy,[176] is defined as

$$T_\theta = T_s - T_{\mathrm{vW}}. \tag{63}$$

This Pauli energy can be generally written as

$$T_\theta = \int \tau_{\mathrm{TF}} F_\theta \mathrm{d}\mathbf{r}, \tag{64}$$

where τ_{TF} is the Thomas–Fermi (TF) kinetic energy density,[1,2] which is accurate for free electron gas (FEG),

$$\tau_{\mathrm{TF}} = \frac{3}{10}(3\pi^2)^{2/3}\rho^{5/3}. \tag{65}$$

Here, F_θ represents the enhancement factor. The corresponding Pauli potential is then given by

$$V_\theta(\mathbf{r}) = \delta E_\theta/\delta\rho(\mathbf{r}). \tag{66}$$

Notably, in a spin-degenerate system, the Pauli kinetic energy density can be expressed analytically using Kohn–Sham orbitals $\psi_i(\mathbf{r})$ and corresponding occupation numbers f_i,[176]

$$\tau_\theta^{\mathrm{KS}} = \sum_{i=1}^{M} f_i|\nabla\psi_i|^2 - \frac{|\nabla\rho|^2}{8\rho}, \tag{67}$$

where i represents the Kohn–Sham orbitals. The Pauli potential is then defined by

$$V_\theta^{\mathrm{KS}} = \rho^{-1}\left(\tau_\theta^{\mathrm{KS}} + 2\sum_{i=1}^{M} f_i(\varepsilon_M - \varepsilon_i)\psi_i^*\psi_i\right), \tag{68}$$

where ε_i represents the eigenvalue associated with the Kohn–Sham orbital $\psi_i(\mathbf{r})$. In addition, M denotes the highest occupied state, and ε_M is the eigenvalue of $\psi_M(\mathbf{r})$, which corresponds to the chemical potential E_μ.

3. Machine learning based kinetic energy density functional

In recent years, machine learning (ML) techniques have breathed new life into the development of KEDF.[177–183] For example, Sun *et al.* imposed a Machine learning based Physical-constrained Nonlocal (MPN) KEDF and implemented it in ABACUS.[183] The MPN KEDF is designed to satisfy three exact physical constraints: the scaling law of electron kinetic energy $T_\theta[\rho_\lambda] = \lambda^2 T_\theta[\rho]$, $\rho_\lambda = \lambda^3\rho(\lambda\mathbf{r})$, the free electron gas (FEG) limit, and the non-negativity of Pauli energy density.

As illustrated by Fig. 14, the core structure of the MPN KEDF is a neural network (NN). The output of the NN, denoted as $F^{\mathrm{NN}}(\mathbf{r})$, represents the enhancement factor F_θ for each real-space grid point $\mathbf{r}$. To ensure that the calculated Pauli energy and potential adhere to the FEG limit and the non-negativity of the Pauli energy density, the enhancement factor for the Pauli energy is defined as

$$F_\theta^{\mathrm{NN}} = \mathrm{softplus}\left(F^{\mathrm{NN}} - F^{\mathrm{NN}}|_{\mathrm{FEG}} + \ln(e-1)\right), \tag{69}$$

where $\mathrm{softplus}(x) = \ln(1+e^x)$ is an activation function commonly used in machine learning, which satisfies $\mathrm{softplus}(x) \geq 0$ and $\mathrm{softplus}(x)|_{x=\ln(e-1)} = 1$. By construction, the non-negativity constraint is satisfied,

$$F_\theta^{\mathrm{NN}} \geq 0, \tag{70}$$

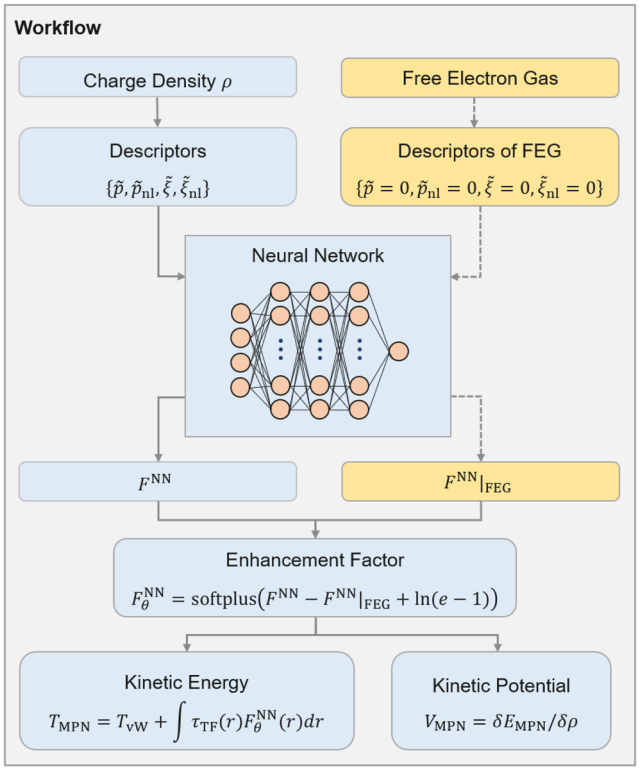

FIG. 14. Workflow of the MPN kinetic energy density functional within the framework of orbital-free DFT. Adapted with permission from L. Sun and M. Chen, Phys. Rev. B **109**(11), 115135 (2024). Copyright 2024 American Physical Society.

and the FEG limit, where the enhancement factor should be 1, is also met,

$$\begin{aligned} F_\theta^{\mathrm{NN}}|_{\mathrm{FEG}} &= \mathrm{softplus}\left(F^{\mathrm{NN}}|_{\mathrm{FEG}} - F^{\mathrm{NN}}|_{\mathrm{FEG}} + \ln(e-1)\right) \\ &= 1. \end{aligned} \tag{71}$$

Furthermore, the selection of the kernel function and descriptors ensures that once the FEG limit of the Pauli energy is satisfied, the FEG limit of the Pauli potential is automatically fulfilled. The scaling law is ensured by the definition of the descriptors, which will be introduced subsequently.

As displayed in Fig. 14, the NN for the MPN KEDF uses four descriptors $\{\tilde{p}, \tilde{p}_{\mathrm{nl}}, \tilde{\xi}, \tilde{\xi}_{\mathrm{nl}}\}$ as inputs. First, the semilocal descriptor $\tilde{p}$ is defined as the normalized dimensionless gradient of the charge density,

$$\tilde{p}(\mathbf{r}) = \tanh(0.2p(\mathbf{r})), \tag{72}$$

where the parameter $p(\mathbf{r})$ is given by

$$p(\mathbf{r}) = |\nabla\rho(\mathbf{r})|^2 / \left[2(3\pi^2)^{1/3}\rho^{4/3}(\mathbf{r})\right]^2. \tag{73}$$

The corresponding nonlocal descriptor $\tilde{p}_{nl}$ is defined as

$$\tilde{p}_{\mathrm{nl}}(\mathbf{r}) = \int w(\mathbf{r}-\mathbf{r}')\tilde{p}(\mathbf{r}')d\mathbf{r}', \tag{74}$$

where $w(\mathbf{r}-\mathbf{r}')$ is a kernel function similar to the WT kernel function.[162] This kernel function is defined in reciprocal space as

$$w(\eta) = \left(\frac{1}{2} + \frac{1-\eta^2}{4\eta}\ln\left|\frac{1+\eta}{1-\eta}\right|\right)^{-1} - 3\eta^2 - 1, \tag{75}$$

where $\eta = \frac{k}{2k_{\mathrm{F}}}$ is a dimensionless reciprocal space vector, and $k_{\mathrm{F}} = (3\pi^2\rho_0)^{1/3}$ is the Fermi wave vector, with ρ_0 representing the average charge density.

The third and fourth nonlocal descriptors, $\tilde{\xi}$ and $\tilde{\xi}_{\mathrm{nl}}$, represent the distribution of charge density. These descriptors are defined as

$$\tilde{\xi}(\mathbf{r}) = \tanh\left(\frac{\int w(\mathbf{r}-\mathbf{r}')\rho^{1/3}(\mathbf{r}')d\mathbf{r}'}{\rho^{1/3}(\mathbf{r})}\right) \tag{76}$$

and

$$\tilde{\xi}_{\mathrm{nl}}(\mathbf{r}) = \int w(\mathbf{r}-\mathbf{r}')\tilde{\xi}(\mathbf{r}')d\mathbf{r}'. \tag{77}$$

Here, $w(\mathbf{r}-\mathbf{r}')$ is the same kernel function used in the definition of the other nonlocal descriptors.

The loss function for the MPN KEDF is defined as

$$\begin{aligned} L = \frac{1}{N}\sum_{\mathbf{r}}\left[\left(\frac{F_\theta^{\mathrm{NN}} - F_\theta^{\mathrm{KS}}}{\bar{F}_\theta^{\mathrm{KS}}}\right)^2 + \left(\frac{V_\theta^{\mathrm{MPN}} - V_\theta^{\mathrm{KS}}}{\bar{V}_\theta^{\mathrm{KS}}}\right)^2\right] \\ + \left[F^{\mathrm{NN}}|_{\mathrm{FEG}} - \ln(e-1)\right]^2, \end{aligned} \tag{78}$$

where N is the total number of grid points, and $\bar{F}_\theta^{\mathrm{KS}}$ ($\bar{V}_\theta^{\mathrm{KS}}$) represents the mean value of F_θ^{KS} (V_θ^{KS}). The first term in the loss

function accounts for the discrepancy between the predicted Pauli energy enhancement factor F_θ^{NN} and the reference KS Pauli energy enhancement factor F_θ^{KS}. The second term ensures that the predicted Pauli potential V_θ^{MPN} closely matches the KS Pauli potential V_θ^{KS}. This term is crucial because the Pauli potential plays a significant role in determining the optimization direction and step size during OF-DFT calculations. The final term is a penalty term designed to minimize the magnitude of the FEG correction, thereby enhancing the stability of the MPN KEDF.

The training set for the MPN KEDF includes eight metallic structures, specifically bcc Li, fcc Mg, and fcc Al, as well as five alloys, Li_3Mg (mp-976254), LiMg (mp-1094889), Mg_3Al (mp-978271), β'' $MgAl_3$,[184] and $LiAl_3$ (mp-10890). The numbers in parentheses correspond to the Materials Project IDs.[185] To evaluate the precision and transferability of the MPN KEDF, a test set was constructed using 59 alloys from the Materials Project database.[185] This testing set includes 20 Li–Mg alloys, 20 Mg–Li alloys, 10 Li–Al alloys, and 9 Li–Mg–Al alloys. The total energies and formation energies of 59 alloys as calculated by various KEDFs in OF-DFT are presented in Fig. 15. As depicted in Fig. 15(a), the TFλvW KEDF systematically underestimates the total energies compared to the results from KS-DFT, leading to a substantial mean absolute error (MAE) of 0.934 eV/atom. In contrast, the LKT KEDF demonstrates improved performance with a reduced MAE of 0.145 eV/atom. The nonlocal WT KEDF further enhances accuracy, achieving an MAE of 0.043 eV/atom. Although the MPN KEDF has a higher MAE of 0.123 eV/atom compared to the WT KEDF, it still outperforms both the TFλvW and LKT KEDFs. Figure 15(b) illustrates the formation energies. The LKT KEDF consistently overestimates the values compared to those obtained by KS-DFT and yields a high MAE of 0.166 eV. This is significantly larger than the MAEs achieved by the TFλvW KEDF (0.051 eV) and the WT KEDF (0.035 eV). Notably, the MPN KEDF demonstrates superior performance with an even lower MAE of 0.028 eV, outperforming the WT KEDF.

While the MPN KEDF has shown promising results for simple metals and their alloys,[183] its performance remains limited for semiconductors. To address this, Sun *et al.* developed a multi-channel MPN KEDF[186] that incorporates information from multiple real-space length scales.

IV. METHODS IN NUMERICAL ATOMIC ORBITAL BASIS

A. Numerical atomic orbitals

The efficiency and accuracy of first-principles methods are largely determined by the basis sets. As mentioned in Sec. III, although the accuracy of the plane wave basis in solving the Kohn–Sham equation can be systematically improved by increasing the kinetic energy cutoff, its computational costs are generally formidable for systems consisting of hundreds or thousands of atoms. On the other hand, atomic orbital basis sets are generally more efficient than plane wave basis sets, at the cost of a slight loss in accuracy. In particular, numerical atomic orbitals (NAOs) have become a competitive option for basis set types, especially for calculating large systems consisting of hundreds or even thousands of atoms. The NAO basis set also supports the linear scaling algorithms due to the strict locality feature. Over the past several decades, several methods have been proposed[43,187–191] to perform efficient numerical integrations for NAOs.

Unlike the plane wave basis, there is no unique way to construct NAOs. For example, a popular method involves solving isolated atoms subject to confining potentials.[191–195] Based on confining potentials, Blum *et al.*[43] proposed to generate NAOs by iteratively picking up basis functions one by one from a pool of predefined candidates to seek the best improvement of a target energy. Alternatively, Ozaki[196,197] suggested that eigenfunctions of isolated atoms in confining potentials serve as "primitive orbitals" in terms of which NAOs are expanded, and expansion coefficients can be optimized with self-consistent calculations. Apart from the above energy-based methods, another class of methods constructs NAOs toward some reference states. For example, Sanchez-Portal *et al.*[198,199] proposed to optimize the following "spillage" function defined as

$$\mathscr{S} = \sum_{n\mathbf{k}} \langle \psi_n(\mathbf{k}) | (1 - \hat{P}(\mathbf{k}) | \psi_n(\mathbf{k}) \rangle, \tag{79}$$

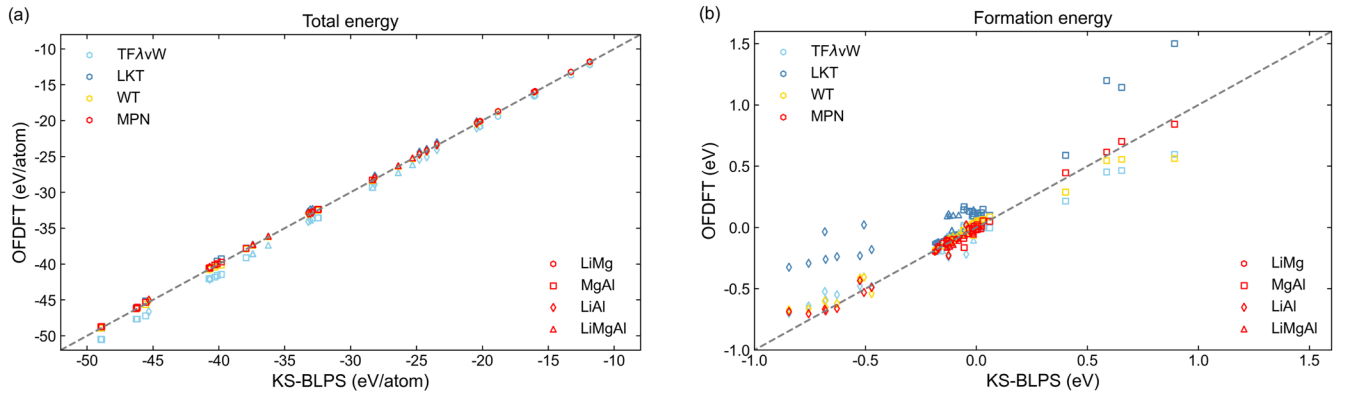

FIG. 15. (a) Total energies (in eV/atom) and (b) formation energies (in eV) of 59 alloys, including 20 Li–Mg alloys, 20 Mg–Li alloys, 10 Li–Al alloys, and 9 Li–Mg–Al alloys. Different colors indicate the formation energies from different KEDFs (TFλvW, LKT, WT, and MPN), while different shapes of markers indicate different alloys. Adapted with permission from L. Sun and M. Chen, Phys. Rev. B **109**(11), 115135 (2024). Copyright 2024 American Physical Society.

where $\{\psi_n(\mathbf{k})\}$ denotes the reference states from plane wave calculations, and $\hat{P}(\mathbf{k})$ is a projection operator defined as

$$\hat{P}(\mathbf{k}) = \sum_{\mu\nu} |\phi_\mu(\mathbf{k})\rangle S^{-1}_{\mu\nu}(\mathbf{k})\langle\phi_\nu(\mathbf{k})|. \tag{80}$$

Here, $S_{\mu\nu}(\mathbf{k})$ is the overlap matrix. In the original work, NAOs are chosen to be combinations of pseudo-atomic orbitals (eigenfunctions of isolated atoms with pseudo-potentials) or Slater-type orbitals. Based on the spillage formalism, Chen *et al.*[18] proposed to construct NAOs with localized spherical Bessel functions as a basis,[200] and reference systems are chosen to be a series of isolated dimers/trimers of variable bond lengths. Recently, Lin *et al.*[24] further improved the basis by introducing a gradient term to the original spillage,

$$\mathscr{S}^{\mathrm{LRH}} = \mathscr{S} + \sum_{n\mathbf{k}} \left\| \hat{p}\left(1 - \hat{P}(\mathbf{k})\right)|\psi_n(\mathbf{k})\rangle \right\|^2, \tag{81}$$

where $\hat{p}$ is the momentum operator. To use the NAO basis set in ABACUS, the collection of NAO basis sets paired with SG15 pseudopotentials[201] is publicly available.[202]

B. Kohn–Sham equation in NAO basis

With the usage of a localized basis set, the Kohn–Sham equation for a given $\mathbf{k}$ point in the Brillouin zone becomes a generalized eigenvalue problem that takes the form of

$$\boldsymbol{H}(\mathbf{k})\boldsymbol{C}(\mathbf{k}) = \boldsymbol{S}(\mathbf{k})\boldsymbol{C}(\mathbf{k})\boldsymbol{E}(\mathbf{k}), \tag{82}$$

where $\boldsymbol{H}(\mathbf{k})$, $\boldsymbol{C}(\mathbf{k})$, and $\boldsymbol{S}(\mathbf{k})$ are the Hamiltonian matrix, the electronic wave function coefficients of NAOs, and the overlap matrix, respectively. $\boldsymbol{E}(\mathbf{k})$ is a diagonal matrix with KS eigenvalues. The overlap matrix element $S_{\mu\nu}(\mathbf{k})$ is given by

$$S_{\mu\nu}(\mathbf{k}) = \sum_{\mathbf{R}} \langle\phi_{\mu 0}|\phi_{\nu\mathbf{R}}\rangle e^{i\mathbf{k}\cdot\mathbf{R}}, \tag{83}$$

where $\phi_{\nu\mathbf{R}}(\mathbf{r})$ is a NAO centered in the cell with lattice vector $\mathbf{R}$.

In general, the terms in the Hamiltonian matrix $H(\mathbf{k})$ are constructed in two ways, i.e., the two-center integrals and the grid integral techniques. Given an operator $\hat{O}$, the two-center integral calculates

$$O_{\mu\nu}(\mathbf{R}) = \int \phi_\mu(\mathbf{r})\hat{O}\phi_\nu(\mathbf{r}-\mathbf{R})\mathrm{d}\mathbf{r}, \tag{84}$$

where functions ϕ (basis or any "projector") centered at atoms spaced by $\mathbf{R}$ are distinguished by μ and ν. The overlap matrix $S_{\mu\nu}(\mathbf{R})$ and the kinetic energy matrix $T_{\mu\nu}(\mathbf{R})$ are evaluated directly with this form, while the representation of the non-local part of the pseudopotential requires the calculation of

$$V^{\mathrm{NL}}_{\mu\nu}(\mathbf{R}) = \sum_{Iij} D^I_{ij}\langle\phi_{\mu\mathbf{0}}|\beta^I_i\rangle\langle\beta^I_j|\phi_{\nu\mathbf{R}}\rangle. \tag{85}$$

Here, indices i and j run over all projects for atom I. Equation (82) is solved independently for each $\mathbf{k}$ point.

In the context of LCAO-based DFT calculations within the ABACUS package, real-space uniform grid integrals hold significant importance, as they are key to multiple critical computational steps. For example, the grid integration is used to construct the local potential term of the Hamiltonian and the electron density in real space, as well as the Pulay force term when calculating the atomic forces. To optimize these grid integrals, we partition real-space grids across MPI processes and use parallel matrix operations, which substantially accelerate the overall computation.[203]

The representation of the Hamiltonian or any operator within the momentum space is obtained via a "folding" operation,

$$H_{\mu\nu}(\mathbf{k}) = \sum_{\mathbf{R}} H_{\mu\nu}(\mathbf{R})e^{i\mathbf{k}\cdot\mathbf{R}}, \tag{86}$$

in which $\mathbf{R}$ always runs over all valid neighboring cells. After diagonalization of the Hamiltonian matrix, the eigenvalues and corresponding Kohn–Sham wave functions can be obtained.

To solve the generalized eigenvalue problem in Eq. (82), ABACUS supports numerical libraries such as ScaLAPACK[204] and the Eigenvalue SoLvers for Petaflop Applications (ELPAs).[205] ABACUS also provides the pole expansion and selected inversion (PEXSI) method as a low-scaling alternative (see Sec. VI I for the details). In addition, we have implemented GPU acceleration through specialized numerical libraries, such as the GPU-enabled ELPA implementation.[206] After diagonalization, the density matrix can be constructed via the formula

$$\rho_{\mu\nu}(\mathbf{R}) = \frac{1}{N_{\mathbf{k}}}\sum_{n\mathbf{k}} f_{n\mathbf{k}} c_{n\mu,\mathbf{k}} c^*_{n\nu,\mathbf{k}} e^{-i\mathbf{k}\cdot\mathbf{R}}, \tag{87}$$

where $f_{n\mathbf{k}}$ is the occupation, and the electronic wave functions are $\{c_{n\mu,\mathbf{k}}\}$. Subsequently, the electron charge density $\rho(\mathbf{r})$ can be evaluated through real-space grids.

To assess the accuracy of the NAO basis set, we conducted a systematic comparison with PW results. A series of NAO basis sets—including single-ζ (SZ), double-ζ plus polarization functions (DZP), and triple-ζ plus double polarization functions (TZDP)—were generated with varying cutoff radii based on the Pseudo-Dojo v0.4 (3plus) pseudopotential. We then performed SCF calculations using these basis sets, and the resulting total energies are presented in Fig. 16. Our analysis demonstrates that incorporating a larger number of atomic orbitals and employing higher cutoff values significantly reduces the discrepancy between NAO and PW results. Notably, the TZDP basis set with a cutoff of 10 a.u. yields the closest agreement with the PW results, exhibiting a minimal deviation of ~0.0053 eV/atom.

C. Forces and stress

To obtain the analytical expression for atomic forces and stress, one must start with the analytical expression for the total energy,

$$E_{\mathrm{tot}} = \sum_{\mu\nu\mathbf{R}} \rho_{\nu\mu}(\mathbf{R})\left[T_{\mu\nu}(\mathbf{R}) + V^{\mathrm{NL}}_{\mu\nu}(\mathbf{R})\right] + \int V_{\mathrm{local}}(\mathbf{r})\rho(\mathbf{r})\mathrm{d}\mathbf{r} + \frac{1}{2}\iint \frac{\rho(\mathbf{r})\rho(\mathbf{r}')}{|\mathbf{r}-\mathbf{r}'|}\mathrm{d}\mathbf{r}\mathrm{d}\mathbf{r}' + E_{\mathrm{xc}}[\rho(\mathbf{r})] + E_{\mathrm{II}}, \tag{88}$$

where the kinetic and nonlocal pseudopotential matrices are, respectively, labeled as $T_{\mu\nu}(\mathbf{R})$ and $V^{\mathrm{NL}}_{\mu\nu}(\mathbf{R})$, while the local pseudopotential is V_{local} and the ionic energy E_{II} is given by the Ewald method.[129] It should be noted that ABACUS uses Eq. (33) to calculate the total

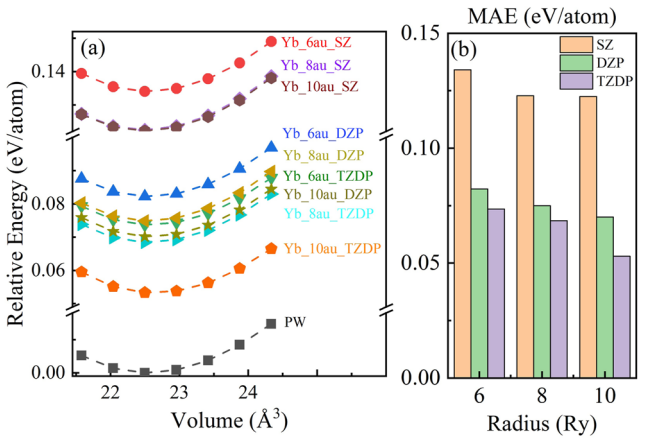

FIG. 16. (a) Comparison of energies calculated with NAO and PW basis sets for the $Li_{12}Yb_4Cl_{24}$ system, calculated using Yb SZ/DZP/TZDP orbitals with different orbital cutoffs. (b) Mean absolute error (MAE, in eV/atom) of the energies between NAO and PW basis sets for different volumes.

energy in practical computations. For more information about evaluating force and stress terms in ABACUS, we refer the readers to a recent review work in Ref. 30.

The atomic forces are obtained by direct differentiation of the total energy E_{tot} with respect to atomic positions,

$$\begin{aligned} \boldsymbol{F}_I &= -\sum_{\mu\nu\mathbf{R}} \rho_{\nu\mu}(\mathbf{R}) \frac{\partial H_{\mu\nu}(\mathbf{R})}{\partial \mathbf{R}_I} - \sum_{\mu\nu} \frac{\partial \rho_{\nu\mu}(\mathbf{R})}{\partial \mathbf{R}_I} H_{\mu\nu}(\mathbf{R}) \\ &= \boldsymbol{F}_I^{\mathrm{FH}} + \boldsymbol{F}_I^{\mathrm{Pulay}} + \boldsymbol{F}_I^{\mathrm{Orth}} + \boldsymbol{F}_I^{\mathrm{Ewald}}. \end{aligned} \tag{89}$$

Here, we utilize the Feynman–Hellmann theorem[130,131] and divide the total forces into four components. First, the Feynman–Hellmann force $\boldsymbol{F}_I^{\mathrm{FH}}$ describes the contribution of the partial derivatives of the Hamiltonian operator. In this term, the kinetic and nonlocal pseudopotential terms are evaluated through the two-center integration technique, while the local pseudopotential contribution is evaluated through the plane wave basis as shown in Eq. (35). Second, the Pulay force $\boldsymbol{F}_I^{\mathrm{Pulay}}$ describes the partial derivatives of the NAO basis set with respect to ionic positions, as, unlike the plane wave basis set, the NAO basis set changes with atomic positions. Third, the orthogonal force $\boldsymbol{F}_I^{\mathrm{Orth}}$ arises from the nonorthogonality of the NAO basis set, and an energy density matrix must be evaluated to yield this term. Finally, the contribution of ionic interactions to atomic forces is included in $\boldsymbol{F}_I^{\mathrm{Ewald}}$. The stress tensor defined in Eq. (23) can also be derived using the NAO basis set; the formulas are similar to the above force formulas. For more details, please refer to Ref. 30.

To evaluate the consistency of atomic forces using the NAO basis, we performed finite-difference tests on a body-centered cubic (bcc) iron (Fe) system. In particular, a single Fe atom was displaced along the x-axis in both positive and negative directions by a defined step size, and the corresponding energy changes were computed. Figure 17(a) compares the atomic forces derived from the finite-difference method (using a step size of 0.02 bohr) with analytically calculated forces at varying atomic positions. The inset illustrates

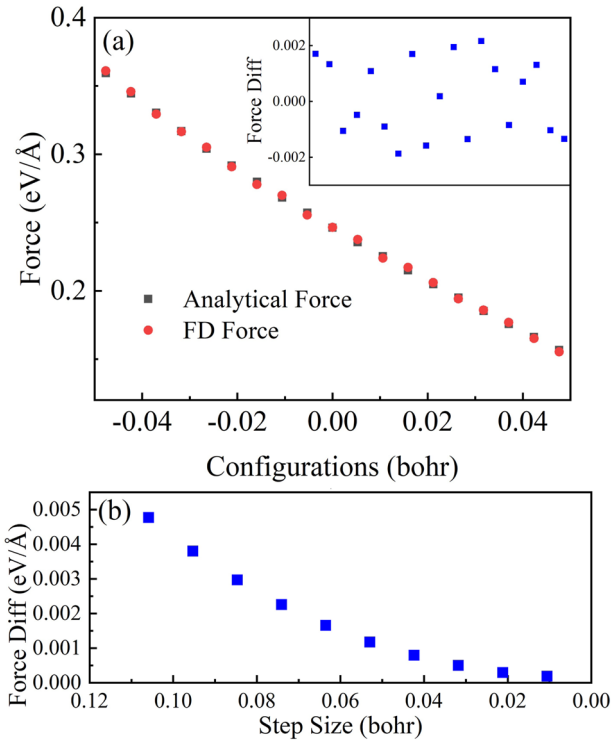

FIG. 17. By using the NAO basis set, the finite difference (FD) tests of atomic forces on the x-axis of bcc Fe. (a) Analytical forces and the forces calculated by the FD method along the x-direction for different configurations. The zoom-in figure shows the difference between them. (b) Deviations between FD values and analytical values along the Fe x-direction for different step sizes used in the FD method.

the residual differences between the two methods. For the Fe system, the observed force discrepancy is on the order of 0.002 eV/Å. This deviation is influenced by several factors, including the precision of the finite-difference step size and the numerical accuracy of the SCF calculations. Further investigation of the step-size dependence [Fig. 17(b)] reveals that the discrepancy diminishes as the step size decreases, asymptotically approaching zero. This behavior confirms the consistency between the NAO-implemented forces and the energy landscape in ABACUS.

D. Hybrid functional

Hybrid density functionals (HDFs) formulated within the generalized KS framework[207] belong to the fourth rung of Jacob's ladder.[208] It overcomes the drawbacks of the local and semi-local XC functionals, namely, the self-interaction errors[209,210] related to the underestimation of the bandgaps in solids. The ABACUS package supports pure exact exchange (EXX) calculations, specifically the Hartree–Fock (HF) method. Building upon this capability, we have implemented several widely used hybrid functionals, including the Heyd–Scuseria–Ernzerhof (HSE),[65] PBE0,[67,211] and SCAN0.[212] The local (semilocal) components of these functionals are computed using the LibXC library,[213] while the exact (Fock) exchange energy is evaluated through two-electron integrals of the Kohn–Sham orbitals.

The exact exchange Hamiltonian under the representation of the NAOs basis is given by

$$H_{\mu\nu}^{\mathrm{EXX}}(\mathbf{R}) = \sum_{\lambda\sigma}\sum_{\mathbf{R}_1}\sum_{\mathbf{R}_2}\rho_{\lambda\sigma}(\mathbf{R}_2-\mathbf{R}_1)(\phi_\mu^{\mathbf{0}}\phi_\lambda^{\mathbf{R}_1}|\phi_\sigma^{\mathbf{R}_2}\phi_\nu^{\mathbf{R}}), \quad (90)$$

where the real space density matrix $\rho_{\lambda\sigma}(\mathbf{R})$ is defined in Eq. (87) and the four-index integrals are defined as

$$(\phi_\mu^{\mathbf{0}}\phi_\lambda^{\mathbf{R}_1}|\phi_\sigma^{\mathbf{R}_2}\phi_\nu^{\mathbf{R}}) = \iint \phi_\mu^{\mathbf{0}}(\mathbf{r})\phi_\lambda^{\mathbf{R}_1}(\mathbf{r})v(\mathbf{r}-\mathbf{r}')\phi_\sigma^{\mathbf{R}_2}(\mathbf{r}')\phi_\nu^{\mathbf{R}}(\mathbf{r}')\mathrm{d}\mathbf{r}\mathrm{d}\mathbf{r}', \quad (91)$$

with $v(\mathbf{r}-\mathbf{r}') = 1/|\mathbf{r}-\mathbf{r}'|$ for the bare Coulomb in PBE0 and HF, while $v(\mathbf{r}-\mathbf{r}') = \mathrm{erfc}(\omega|\mathbf{r}-\mathbf{r}'|)/|\mathbf{r}-\mathbf{r}'|$ for short-range EXX in HSE.

In fact, the above EXX effective potential exhibits an unfavorable $O(N^4)$ scaling behavior, making it significantly more computationally demanding than local functionals in terms of both time and memory requirements. To mitigate this challenge, several algorithmic approaches have been developed, most notably the density fitting (DF) technique[214] and its specialized implementation for localized atomic orbitals known as resolution of identity (RI).[215–217] These methods reduce the four-center integrals to combinations of three- and two-center integrals by expanding the orbital products using auxiliary basis functions (ABFs).

For HDF calculations in large periodic systems, the local resolution of identity (LRI) approach[21,218,219] enables linear-scaling EXX calculations by exploiting the inherent locality of both atomic orbitals (AOs) and ABFs. Extensive benchmarking has demonstrated that with properly chosen ABFs, the LRI approximation achieves sufficient accuracy for HDF calculations.[21] Residual discrepancies in cohesive properties and bandgaps primarily originate from differences in core–valence interaction treatments (pseudopotentials vs all-electron methods) rather than basis set limitations.[220]

ABACUS employs two distinct types of ABFs: the "on-site" ABFs, designed to fit products of orbitals centered on the same atom, and the "opt" ABFs, developed to improve the fitting accuracy for interatomic orbital products. Both types maintain the same functional form as AOs, consisting of a radial function multiplied by spherical harmonics $P_{A\alpha=\{nlm\}}(\mathbf{r}) = g_{nl}(r)Y_{lm}(\hat{\mathbf{r}})$. The radial components of "on-site" ABFs are constructed through pairwise multiplication of AO radial functions on the same atom $g_{nl}(r) = f_{n_1l_1}(r)f_{n_2l_2}(r)$, with the angular momentum constraint $|l_1-l_2| \le l \le l_1+l_2$, followed by orthogonalization and selection via principal component analysis (PCA). The "opt" ABFs are generated in the same way as AO-generation.[18,19]

The computational efficiency is substantially enhanced by exploiting the inherent locality of both AOs and the density matrix, which enables effective prescreening of negligible submatrices below a specified threshold. For parallel computation of four-center integrals, we have implemented two complementary distribution strategies: a load-balancing greedy algorithm for multi-processor scheduling and a spatially optimized scheme based on K-means clustering of ABF atom pairs. The latter minimizes both inter-processor communication overhead and memory requirements by ensuring geometrically proximate pairs are assigned to the same processor, with memory consumption scaling linearly with the union of their neighbor lists.[23]

Notably, the LRI-based four-center integration has been modularized into the standalone LibRI library,[221] which provides a portable and efficient implementation that can be readily integrated into various electronic structure codes. This includes both conventional DFT packages and beyond-DFT methods such as the random phase approximation (RPA) and GW calculations,[222] offering substantial acceleration for two-electron Coulomb repulsion integral evaluations across different theoretical frameworks.

In 2025, Lin *et al.* developed a linear-scaling algorithm for exact-exchange forces and stresses in hybrid DFT, applicable to both molecules and periodic systems. Leveraging numerical atomic orbitals and localized resolution-of-identity, the massively parallel implementation enables structural relaxation of thousand-atom systems in ABACUS.[223]

The EXX module of ABACUS has already been applied to several studies.[21,224,225] In 2024, Lin *et al.* investigated the effect of exact exchange on some of the lead-free halide double perovskites (HDPs) $Cs_2BB'X_6$ (B = Ag^+, Na^+; B = In^{3+}, Bi^{3+}; X = Cl^-, Br^-).[224] They found that some local exchange–correlation functionals fail to capture the geometric and electronic structures of $Cs_2BB'X_6$, which can be traced back to the so-called delocalization error. To show the differences between these functionals, they calculated the bandgap as a function of the B–X bond length using the functionals PBE, PBEsol, SCAN, HSE, and HSE (0.4). Taking $Cs_2AgInCl_6$ as an example in Fig. 18, one can see that the bandgap obtained at the Ag–Cl bond length (2.724 Å) is in much better agreement with the experimental value (3.3 eV), marked by the red triangle.

Generally speaking, hybrid functional calculations can only process systems of limited size due to the large computational demand of building the exact exchange Hamiltonian. By combining NAO basis and LRI techniques, Fig. 19 shows that the time consumption of this part increases almost linearly with the system size, enabling ABACUS to perform hybrid functional calculations for large systems with thousands of atoms. In 2024, Tang *et al.* used hybrid functional data from ABACUS and trained a deep equivariant neural network approach for efficient hybrid density functional calculations.[225] Taking twisted bilayer graphene (TBG) as an

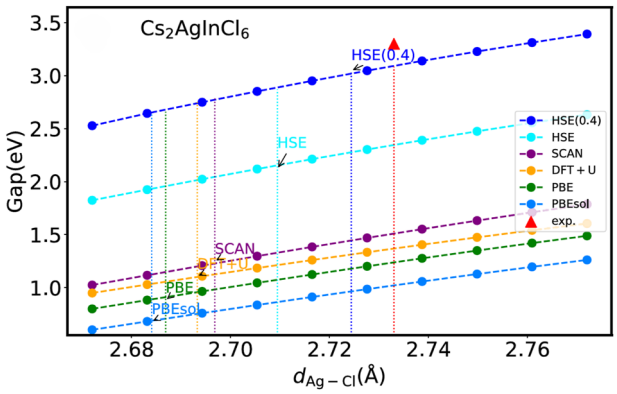

FIG. 18. Bandgaps of $Cs_2AgInCl_6$ with a lattice constant of 10.481 Å, as computed by HSE (0.4), HSE, SCAN, DFT+U, PBE, and PBEsol as a function of Ag–Cl bond length. Adapted with permission from Ji *et al.*, Phys. Rev. Res. **6**, 033172 (2024). Copyright 2024 American Physical Society.

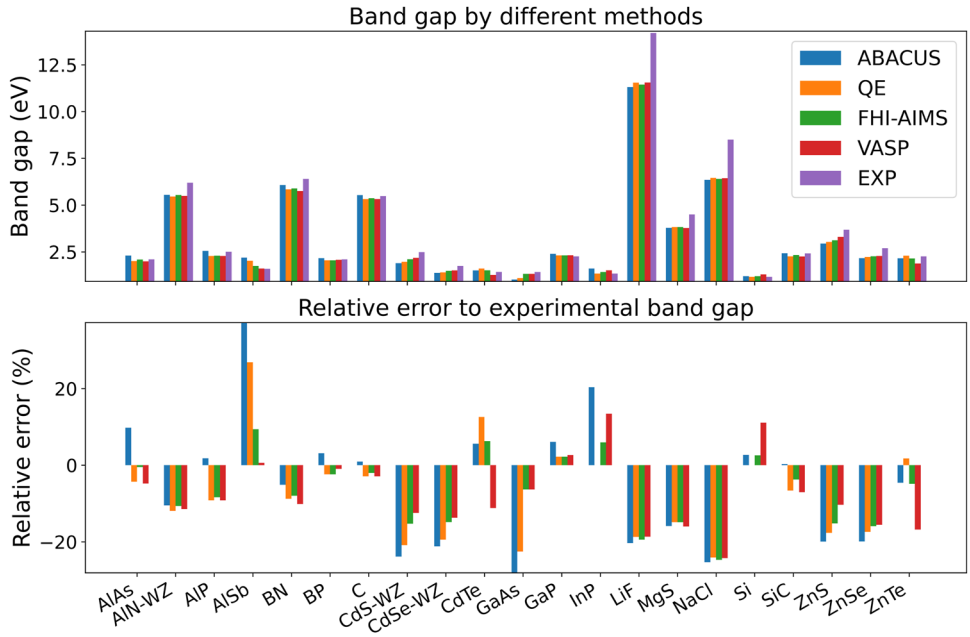

FIG. 19. Bandgaps of 21 different semiconductors, calculated by ABACUS+LibRI, along with the reference computed values from other software (QE/FHI-AIMS/VASP)[21] and experimental values.[226]

example in Fig. 20, they performed the HSE band structure calculations of (17, 16) TBG (twist angle $\theta \approx 2.0046^\circ$, 3268 atoms/cell).[225]

We also performed HSE calculations to obtain the bandgaps of several semiconductors and compared them with the results from other DFT packages (QE/VASP/FHI-AIMS) and the experimental values.[21,226] In these tests, ABACUS and QE employ the SG15-type norm-conserving PBE pseudopotentials (except for In, which is PSlibrary norm-conserving), and VASP employs the PBE PAW potentials, whereas FHI-AMIS performs all-electron calculations.[227] Figure 19 shows that the bandgaps obtained by ABACUS HSE calculations are consistent with the results from other DFT packages, demonstrating satisfactory results when compared to the experimental values.

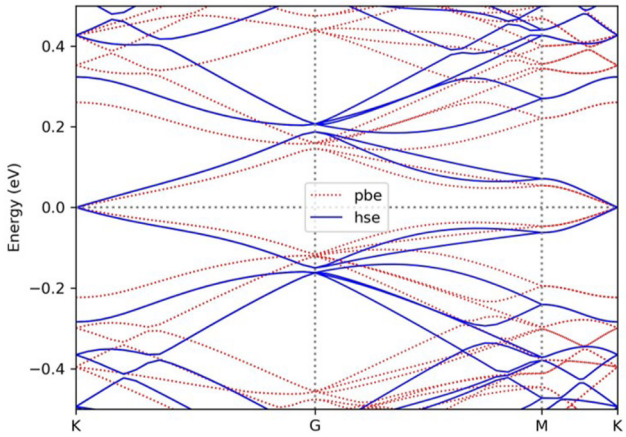

FIG. 20. Band structures of twisted bilayer graphene with $\theta \approx 2.0046^\circ$, 3268 atoms/cell, computed by ABACUS using the PBE and HSE06 functionals. Adapted with permission from Tang *et al.*, Nat. Commun. **15**, 8815 (2024). Copyright 2024 Springer Nature.

E. DeePKS

The exchange–correlation functional is critical to determining the accuracy of DFT. However, when different levels of XC functionals are selected, there exists a trade-off between accuracy and efficiency. Lower-level XC functionals on Jacob's ladder[208] typically offer higher computational efficiency but lower accuracy, whereas higher-level ones exhibit the opposite trend. With the rapid progress in increasing computational resources and advanced algorithms, AI-assisted methods hold the potential to mitigate this issue.[228,229]

Proposed in 2020, the DeeP Kohn–Sham method (DeePKS)[33] employs a computationally efficient neural network-based functional model to represent the energy and force difference between a lower-level XC functional and a higher-level XC functional. The resulting model maintains translational, rotational, and permutational invariance and can be used in self-consistent field calculations. Together with the DeePKS-kit[34] software, ABACUS supports the iterative training of DeePKS models.[230] In particular, DeePKS models can be trained in molecular or periodic systems to learn properties such as energy, force, stress, and bandgap. Based on the DeePKS model, ABACUS can achieve accuracy similar to that of the high-level XC functional on these specified properties, while the computational efficiency is similar to that of the low-level XC functional.

In the DeePKS method, we divide the total energy functional into two parts,

$$E_{\mathrm{DeePKS}}[\{\psi_i\}|\omega] = E_{\mathrm{baseline}}[\{\psi_i\}] + E_\delta[\{\psi_i\}|\omega], \tag{92}$$

where $\{\psi_i\}$ are the single-particle orbitals to yield the baseline energy E_{baseline}, and E_δ is constructed as a neural network model with

parameters ω. The model input is constructed based on the projected density matrix for each atom I, which takes the form

$$D^I_{nlmm'} = \sum_{\mu\nu} \langle \alpha^I_{nlm'} | \phi_\nu \rangle \rho_{\mu\nu} \langle \phi_\mu | \alpha^I_{nlm} \rangle. \quad (93)$$

Here, $\rho_{\mu\nu}$ represents the density matrix, and $|\alpha^I_{nlm}\rangle$ is a set of localized orbitals centered on atoms, identified by atomic index I, and quantum numbers nlm. The atomic-centered basis functions $|\alpha^I_{nlm}\rangle$ ensure the translational invariance. To maintain rotational invariance, we proceed to extract the eigenvalues of projected density matrix blocks with the same indices I, n, and l, resulting in a set of descriptors that are obtained as eigenvalues of the projected density matrix,

$$\mathbf{d}^I_{nlm} = \mathrm{Eig}(D^I_{nlmm'}). \quad (94)$$

The descriptors are then grouped into vectors based on the atomic index I, and E_δ is calculated as the sum of atomic contributions as

$$E_\delta = \sum_I F_{\mathrm{NN}}(\mathbf{d}^I | \boldsymbol{\omega}), \quad (95)$$

where F_{NN} is the deep neural network. Next, the Hamiltonian operator can be written as

$$H = H_{\mathrm{baseline}} + \hat{V}^\delta, \quad (96)$$

where the H_{baseline} term is the baseline Hamiltonian, and the correction potential can be evaluated via

$$\hat{V}^\delta_{\mu\nu} = \frac{\partial E_\delta}{\partial \rho_{\mu\nu}}. \quad (97)$$

Finally, the corresponding force and stress terms can also be obtained for the correction term.[230]

Here, we list a few applications using the DeePKS method. For instance, halide perovskites (ABX_3, X = halogen anion) have shown great promise as a cost-effective alternative to current commercial photovoltaic technologies. Designing effective photovoltaic systems requires a precise yet efficient description of the electronic structure of halide perovskites. One key benefit of halide perovskites is adjusting the absorption edge wavelength (bandgap) by changing the ratio of different halide ions. Ou *et al.*[231] constructed a general DeePKS model that can be utilized for halide perovskites, including different combinations of ABX_3 (A = FA, MA, Cs; B = Sn, Pb; X = Cl, Br, I), the organic–inorganic hybrid alternatives, and the Ruddlesden–Popper (RP) perovskites. In detail, the authors built an extensive DeePKS model upon 460 configurations spanning seven types of halide perovskites, with HSE06 accuracy and satisfactory predictions for the bandgap. Based on an iterative training process with ABACUS and DeePKS-kit, they showed that the resulting DeePKS model can accurately replicate forces, stress, bandgaps, and density of states (DOS) near the Fermi energy for all types of halide perovskites, including RP structures and hybrid compositions, when compared to HSE06. They further showed the bandgaps predicted by DeePKS and PBE, with respect to those by HSE06, over 30 tested systems. As depicted in Fig. 21, the DeePKS model demonstrated precise predictions of bandgaps for all perovskites examined, closely aligning with the HSE06 findings and yielding an average absolute error (MAE) of

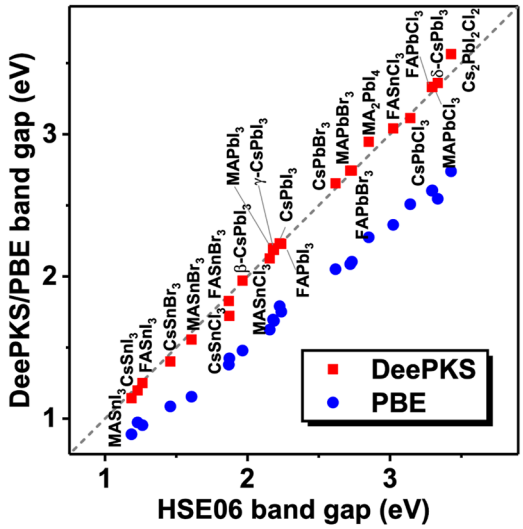

FIG. 21. Bandgaps predicted by DeePKS and PBE with respect to the HSE06 results for all tested perovskites.[231] All tested non-hybrid perovskites are cubic phase except for those indicated by Greek letters. Adapted with permission from Ou *et al.*, J. Phys. Chem. C **127**, 18755–18764 (2023). Copyright 2023 American Chemical Society.

0.0350 eV. On the other hand, PBE significantly underestimated the bandgap values, with a large MAE of 0.5222 eV.

In addition to providing an accurate yet efficient description of the electronic structure, DeePKS also serves as a "bridge" between expensive quantum mechanical (QM) models and ML-based potentials. While the ML-based potentials, such as the Deep Potential Molecular Dynamics (DeePMD),[31,32] have emerged as powerful tools for mitigating the high computational costs associated with *ab initio* molecular dynamics (AIMD), training these potentials demands a significant number of QM-labeled frames. DeePKS offers a solution to further save the computational cost by reducing the required QM-labeled frames, owing to its significantly better transferability as compared to DeePMD. Li *et al.*[230] examined DeePKS and DeePMD's training curves with respect to the number of training samples in systems with 64 water molecules at the accuracy of hybrid functional SCAN0. The DeePKS model outperforms the DeePMD model with fewer frames shown in Fig. 22. In addition, the DeePKS model has a smaller generalization gap than the DeePMD model. The work[230] also showed that excellent agreement can be achieved between the ABACUS-DeePKS-DeePMD results and the ones from SCAN or SCAN0-based DeePMD simulations. By labeling fewer than 200 frames in the training set with SCAN0 or SCAN functionals, the GGA-based DeePKS model can effectively reproduce the energies and forces for pure and salt water systems, with considerable time savings. SCF calculations with trained DeePKS models were carried out and utilized as labels for DeePMD training. Structural properties of liquid water, such as radial distribution function (RDF), bulk density, hydrogen (H) bonds, and dynamic properties such as diffusion coefficient, were found to be excellently matched with those obtained by the SCAN0 AIMD and DeePMD methods. For example, for systems consisting of 64 water molecules,

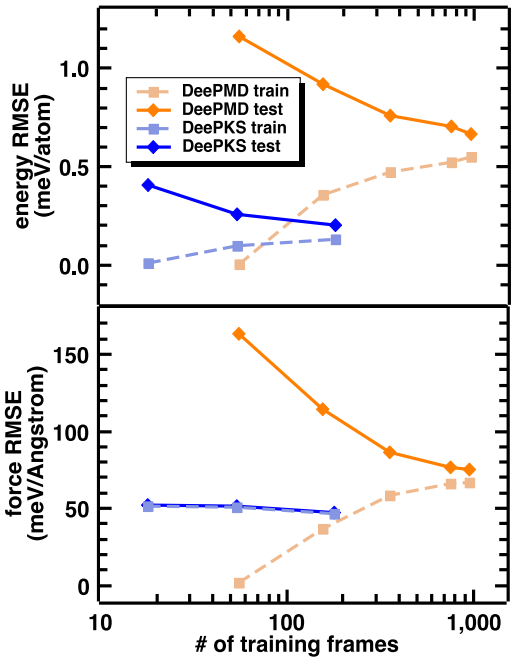

FIG. 22. Learning curves for energy (upper panel) and force (lower panel) given by DeePMD (orange) and DeePKS (blue) with respect to the number of training frames.[230] The dashed line with squares indicates the training set error, while the solid line with diamonds indicates the test set error. Adapted with permission from Li *et al.*, J. Phys. Chem. A **126**(49), 9154–9164 (2022). Copyright 2022 American Chemical Society.

they trained a DeePKS model with 180 training samples at the accuracy of SCAN0. Then, the authors used it to efficiently generate 1000 data points to train the DeePMD potential and performed MD simulations of 512 water molecules. As shown in Fig. 23, various RDFs derived from DeePKS-DeePMD simulations match well with both SCAN0-AIMD and SCAN0-DeePMD results, including a marked decrease in overstructured peaks.

Zhang *et al.*[232] investigated the tautomeric equilibria of glycine in water with the DeePMD model at the accuracy of M06-2X.[233] To avoid expensive computational costs for directly generating the dataset at the M06-2X level, they utilized the DeePKS method as implemented in ABACUS and DeePKS-kit, together with the on-the-fly probability enhanced sampling (OPES)[234] method, to construct the dataset for training the DeePMD model. With this DeePMD potential and OPES, they performed MD simulations and obtained a converged free energy surface (FES). They observed that glycine can undergo tautomerism, transitioning between its neutral and zwitterionic forms through intramolecular and intermolecular proton transfers. Zhang *et al.*[235] adopted a similar strategy to study the propensity of water self-ions at the air(oil)–water interface. They found that the trained DeePKS model can decrease calculation time by about nine times compared to regular M06-2X calculations. With the resulting DeePMD model for an efficient MD process, they demonstrated the stable ionic double-layer distribution near the interface for both air–water and oil–water interface systems.

Liang *et al.*[236] developed an enhanced version of the DeePKS approach, known as DeePKS-ES (electronic structure), to further improve its prediction of electronic structure properties. The DeePKS-ES method modifies the loss function by integrating the Hamiltonian matrix along with its eigenvalues (energy levels) and eigenvectors (wave function coefficients). This adjustment allows DeePKS-ES to reliably predict key electronic structure characteristics such as bandgaps, density of states (DOS), and Hamiltonian matrices, in addition to total energy and atomic forces. When tested on various water systems, including monomers, clusters, and liquid phases, DeePKS-ES achieves a level of accuracy similar to that of the hybrid functional HSE06 while maintaining the computational efficiency of the generalized gradient approximation PBE. In particular, the universal DeePKS-ES model shows strong adaptability across different water systems, connecting quantum-mechanical precision with scalable computation.

F. DFT+*U*

While local and semilocal density functional approximations (LDA and GGAs) can often predict ground-state properties of

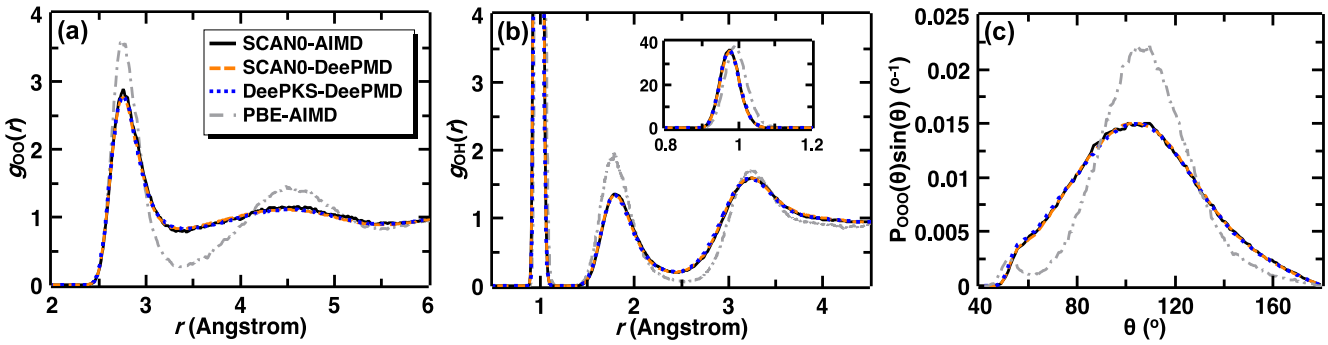

FIG. 23. Radial distribution functions (RDFs) of (a) $g_{OO}(r)$, (b) $g_{OH}(r)$, and (c) bond angle distribution $P_{OO}(\theta)$ given by DeePKS-DeePMD (blue dotted line), SCAN0-AIMD (black solid line), SCAN0-DeePMD (orange dashed line), and PBE-AIMD (gray dotted-dashed line). Adapted with permission from Li *et al.*, J. Phys. Chem. A **126**(49), 9154–9164 (2022). Copyright 2022 American Chemical Society.

various systems with reasonable accuracy, they exhibit significant limitations when applied to strongly correlated materials, such as transition metal oxides and rare-earth compounds. In these systems, the simplified exchange–correlation functionals fail to adequately capture complex electron–electron interactions, leading to substantial inaccuracies in predicted electronic properties, including but not limited to energy bandgaps, magnetic moments, and orbital polarization. The DFT+U method[80–84] addresses these limitations by incorporating a Hubbard-U correction term, which significantly improves the description of strongly correlated electronic systems while maintaining computational costs comparable to standard LDA or GGA calculations.

The DFT+U method is implemented through the following total energy functional:

$$E_{\mathrm{DFA}+U}[\rho] = E_{\mathrm{DFA}}[\rho] + E_{\mathrm{Hub}} - E_{\mathrm{dc}}, \tag{98}$$

where E_{DFA} denotes the baseline energy. In addition, the Hubbard term and double-counting terms are labeled as E_{Hub} and E_{dc}, respectively. In ABACUS, we introduce the fully localized limit (FLL) implementation of the DFT+U method,[83] which assumes that the on-site Coulomb interactions of localized electrons are fully accounted for by the Hubbard U term, while a mean-field average is subtracted to avoid overestimating these interactions. The Hubbard-corrected energy functional is given by

$$E_U\left[\left\{n^{I\sigma}_{mm'}\right\}\right] = \frac{U}{2}\sum_I \sum_{m\sigma}\left(n^{I\sigma}_{mm} - \sum_{m'} n^{I\sigma}_{mm'} n^{I\sigma}_{m'm}\right). \tag{99}$$

Here, the Hubbard parameter U represents an empirically adjusted Coulomb penalty specifically applied to localized electrons, designed to correct the systematic underestimation of electron–electron repulsion inherent in standard DFT calculations. In addition, the central quantity is the on-site density occupancy matrix $n^{I\sigma}_{mm'}$ with I, σ, and m being the atom, spin, and angular momentum indices, respectively. In general, this matrix can be expressed using a local projection operator,

$$\hat{P}^{\sigma}_{mm'} = |\alpha^{I\sigma}_m\rangle\langle\alpha^{I\sigma}_{m'}|, \tag{100}$$

where $\alpha^{I\sigma}_m$ denotes the projection orbital, and $\hat{\rho}$ represents the density matrix,

$$n^{I\sigma}_{mm'} = \langle\alpha^{I\sigma}_m\sigma|\hat{\rho}|\alpha^{I\sigma}_{m'}\sigma\rangle = \mathrm{Tr}(\hat{\rho}\hat{P}^{I\sigma}_{mm'}). \tag{101}$$

Two distinct implementations of the DFT+U method are available in ABACUS when using NAOs as basis sets. These implementations differ primarily in their approach to projecting the electron density onto localized states, a crucial step for accurately modeling strong electron–electron interactions within specific atomic orbitals. The first approach is termed the "dual projection" method, while the second is referred to as the "full projection" method.

First, the dual projection method[25,237] employs a Mulliken charge projector to construct the on-site density occupancy matrix. This approach facilitates the transformation of Kohn–Sham orbitals into a localized correlated subspace using NAOs, particularly for d or f orbitals. The Mulliken projector satisfies the charge sum rule, ensuring conservation of total electronic charge across all projected channels. This methodology is alternatively termed the "dual orbitals" approach[237] due to its fundamental reliance on dual orbitals that maintain mutual orthogonality. Mathematically, these dual orbitals are derived from the original atomic orbitals. The spin-dependent on-site density occupancy matrix is explicitly defined as

$$n^{I\sigma}_{mm'} = \frac{1}{4N_k}\sum_{\mathbf{k}\beta mm'\mu}\Big(S^I_{\beta m,\mu}(\mathbf{k})\rho^{I\sigma}_{\mu,\beta m'}(\mathbf{k}) + \rho^{I\sigma}_{\beta m,\mu}(\mathbf{k})S^I_{\mu,\beta m'}(\mathbf{k}) + S^I_{\beta m',\mu}(\mathbf{k})\rho^{I\sigma}_{\mu,\beta m}(\mathbf{k}) + \rho^{I\sigma}_{\beta m',\mu}(\mathbf{k})S^I_{\mu,\beta m}(\mathbf{k})\Big), \tag{102}$$

where $\rho^{I\sigma}_{\beta m,\mu}(\mathbf{k})$ denotes the density matrix, and $S^I_{\beta m,\mu}(\mathbf{k})$ is the overlap matrix of projected dual orbital $|\beta^I_m\rangle$ and numeric atomic orbital $|\phi_\mu\rangle$ [Eq. (83)]. More details are provided in Ref. 25.

Second, while the dual projection method offers a robust and efficient DFT+U implementation, it relies on a subset of NAOs as projection operators and introduces notable basis set dependence for the Hubbard U parameter. This dependence becomes particularly evident when employing large radial cutoffs, which may affect the description of localized electron characteristics. Therefore, an alternative approach, implemented in ABACUS since version 3.6, involves the modulation of NAOs to construct localized projection operators. This method employs spherical truncation through empirical atomic radius settings, systematically transforming the problem into orbital modulation while satisfying three criteria. First, close correspondence with the original numerical orbitals must be ensured. Second, the orbitals should satisfy the normalization condition. Third, sufficient smoothness at the cutoff of the atomic radius must be ensured.

To be specific, the radial function $\chi(r)$ of the original NAOs undergoes direct truncation followed by normalization operations to yield the truncated localized orbital,

$$\alpha(r) = \left.\frac{\chi(r)g(r;\gamma)}{\langle\chi(r)g(r;\gamma)|\chi(r)g(r;\gamma)\rangle}\right|_{\frac{\partial\langle\alpha|\chi\rangle}{\partial\gamma}=0}, \tag{103}$$

where the smooth function has the form

$$g(r;\gamma) = \begin{cases} 1 - \exp\left(-\dfrac{(r-r_c)^2}{2\gamma^2}\right), & r < r_c, \\ 0, & r \geq r_c. \end{cases} \tag{104}$$

Here, the parameter γ controls the smoothing interval, and the optimal γ is determined iteratively to maximize two-center integrals between modulated $\alpha(r)$ and the original $\chi(r)$ orbitals, yielding the target localized orbitals. The full projection method constructs the on-site density occupancy matrix via the projection operator in real space,[237]

$$\mathrm{n}^{I\sigma}_{mm'} = \sum_{\mathbf{RR}'}\sum_{\mu\nu}\rho^{\mathbf{R}\sigma}_{\mu\nu}\langle\phi^0_\mu|\alpha^{I\mathbf{R}'}_m\rangle\langle\alpha^{I\mathbf{R}'}_{m'}|\phi^{\mathbf{R}}_\nu\rangle. \tag{105}$$

We present systematic benchmarks of the full projection DFT+U method for MnO, CoO, FeO, and NiO systems using ABACUS v3.8. All calculations employ the optimized norm-conserving Vanderbilt (ONCV) pseudopotentials with the SG15-v1.0 version. The Brillouin zone discretization is 0.15 bohr^{-1}, and the energy cutoff is 100 Ry. We use the PBE functional[61] with the Hubbard U

correction, while spin–orbit coupling effects are excluded from consideration. In addition, we adopt a double-ζ plus polarization (DZP) atomic basis with a radial cutoff of 9.0 bohrs for transition metal (TM) elements and 7.0 bohrs for O atoms.

Table I presents the calculated bandgaps and atomic magnetic moments for transition metal oxides (TMOs) with the Hubbard U parameter ranging from 0 to 6 eV. All four investigated TMOs (MnO, FeO, CoO, and NiO) are in the rhombohedral structure with a type-II antiferromagnetic (AFM) configuration. The lattice parameters, adopted from Ref. 238, are 4.445, 4.334, 4.254, and 4.171 Å for MnO, FeO, CoO, and NiO, respectively, with the AFM ordering aligned along the [111] crystallographic direction. Figure 24 further shows the comparison of bandgaps for MnO, FeO, CoO, and NiO systems. The results obtained from ABACUS match well with those from other DFT packages such as VASP, Wien2k, and Quantum ESPRESSO.[25]

G. Real-time time-dependent DFT

DFT is effective in predicting ground-state properties but faces challenges when dealing with excited states. A more accurate theoretical framework for simulating excited states was proposed by Runge and Gross,[248] known as time-dependent density functional theory (TDDFT). Real-time TDDFT (rt-TDDFT) enables the investigation of electron dynamics, including applications in optical absorption spectra,[249] stopping power,[250] photocatalysis,[251] and field-induced transitions. However, its computational cost presents a significant hurdle for large-scale systems. In this context, the use of numerical atomic orbital (NAO) basis sets helps reduce computational expenses while still permitting detailed analysis of excited-state phenomena and their complex behaviors.[252]

The propagation of electrons obeys the time-dependent Kohn–Sham (TD-KS) equation,

$$\mathrm{i}\frac{\partial}{\partial t}\psi_j(\mathbf{r},t) = H\psi_j(\mathbf{r},t). \tag{106}$$

Here, the Hamiltonian H depends only on the electron density at time t, and we adopt the adiabatic approximation. For numerical atomic orbitals, the TD-KS equation can be expressed in the matrix form[253]

$$\mathrm{i}\frac{\partial \boldsymbol{c}}{\partial t} = \boldsymbol{S}^{-1}\boldsymbol{H}\boldsymbol{c}, \tag{107}$$

where $\boldsymbol{S}$ represents the overlap matrix, and $\boldsymbol{c}$ is the column vector of coefficients for the local basis. For simplicity, the subscripts denoting the band index and k-points have been omitted. We adopt the first-order Crank–Nicolson method to approximate the propagator,

$$\boldsymbol{C}(t+\Delta t) = \frac{\boldsymbol{S}(t+\Delta t/2) - \mathrm{i}\boldsymbol{H}(t+\Delta t/2)\Delta t/2}{\boldsymbol{S}(t+\Delta t/2) + \mathrm{i}\boldsymbol{H}(t+\Delta t/2)\Delta t/2}\boldsymbol{C}(t), \tag{108}$$

where $S(t+\Delta t/2)$ and $H(t+\Delta t/2)$ are computed using a linear approximation. Since $H(t+\Delta t/2)$ depends on $\mathbf{C}(t+\Delta t)$, a self-consistent procedure is needed to perform the propagation. The approach to approximating the propagator ensures its time-reversal invariance, conserves the total energy effectively, and preserves the orthogonality of the propagating wave functions. In addition, the Ehrenfest dynamics is adopted for ion–electron coupled systems, and the Verlet algorithm is employed to calculate the ionic velocities and positions at each time step.

The time-dependent electric field $\mathbf{E}(t)$ is introduced into the Hamiltonian to simulate the interactions between the laser field and materials, but there are different ways to implement the electric field. First, within the length gauge, the electric field potential term in the Hamiltonian takes the form of

$$V_{\text{efield}}(\mathbf{r},t) = \mathbf{E}(t)\cdot\mathbf{r}. \tag{109}$$

However, the periodic nature of the cell breaks the translational invariance of the electric potential. To address this, a sawtooth field in the spatial domain takes the form of

$$E_\mu(x_\mu,t) = \begin{cases} E_\mu(t), & \varepsilon < x_\mu < L_\mu - \varepsilon, \\ -E_\mu(t)(L_\mu - 2\varepsilon)/2\varepsilon, & -\varepsilon < x_\mu < \varepsilon, \end{cases} \tag{110}$$

where $\mu = x, y, z$, L_μ is the length of the cell along μ, and $\varepsilon \to 0$. To avoid divergence, the charge density must vanish in the region $-\varepsilon < x_\mu < \varepsilon$. Ideally, this region should be set as a vacuum layer. Therefore, the length gauge can only be used for finite systems.

TABLE I. Bandgaps (in eV) and atomic magnetism (in μ_B) with the format "value of bandgap (value of atomic magnetism of Mn/Co/Fe/Ni)" of MnO, FeO, CoO, and NiO as a function of effective on-site Coulomb energy $\bar{U}$ (in eV). The experimental values are presented in the last row.

$\bar{U}$ (eV)	MnO	CoO	FeO	NiO
0.0	0.00 (4.64)	1.04 (2.46)	0.00 (3.54)	0.83 (1.33)
1.0	0.54 (4.71)	1.30 (2.56)	0.00 (3.61)	1.37 (1.44)
2.0	1.31 (4.76)	1.52 (2.62)	1.01 (3.68)	1.83 (1.52)
3.0	2.01 (4.80)	1.71 (2.67)	1.38 (3.74)	2.25 (1.58)
4.0	2.45 (4.84)	1.86 (2.72)	1.93 (3.78)	2.63 (1.63)
5.0	2.63 (4.87)	1.99 (2.76)	2.28 (3.82)	3.01 (1.67)
6.0	2.77 (4.90)	2.10 (2.79)	2.48 (3.86)	3.23 (1.71)
Expt.	3.6–3.8[239] (4.58[240])	2.4[241] (3.8[242])	2.4[243] (3.32[244])	4.0[245]/4.3[246] (1.90[247])

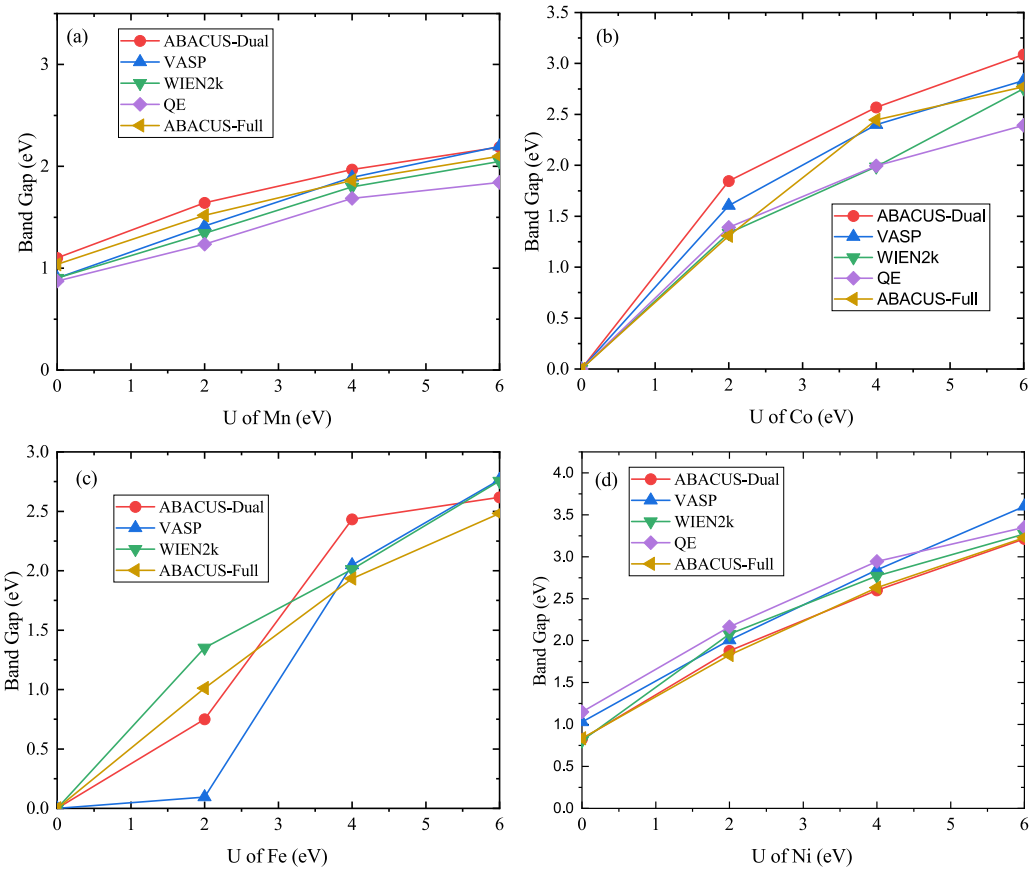

FIG. 24. Bandgaps of transition metal monoxide (a) MnO, (b) FeO, (c) CoO, and (d) NiO as influenced by the Hubbard *U* parameter, utilizing a rhombohedral cell with a type-II antiferromagnetic structure. "ABACUS-Full" presents the results from the full projection method. For comparative analysis, PBE+*U* results for other computational methods are from Ref. 25.

The second method is the velocity gauge, which introduces a vector potential $\mathbf{A}(t)$ to simulate the laser field as

$$\mathbf{A}(t) = -\int \mathbf{E}(t)\, \mathrm{d}t. \tag{111}$$

Therefore, the kinetic term of the velocity-gauge Hamiltonian becomes

$$H_{\text{kinetic}} = \frac{1}{2}[-\mathrm{i}\nabla + \mathbf{A}(t)]^2. \tag{112}$$

This method maintains the periodicity of the system. Third, while rt-TDDFT in periodic systems often relies on the velocity gauge to maintain periodicity under external fields, NAO implementations face a critical limitation: the position-dependent phase variations induced by the vector potential are neglected, leading to errors, especially for properties such as current. To overcome this challenge, Zhao and He[254] introduce a hybrid gauge in ABACUS that incorporates both the electric field and the vector potential, explicitly preserving phase information within atomic orbitals. Benchmark results confirm that this approach fully rectifies the inaccuracies of the pure velocity gauge in NAO-based rt-TDDFT, delivering reliable and precise simulations of ultrafast dynamics.

Based on the rt-TDDFT functionality of ABACUS, Liu *et al.*[251] studied the dissociation process of water molecules under thermal and photoexcitation conditions using Ni single atoms supported on CeO_2, as shown in Fig. 25. The ground-state electronic density shows that when water molecules adsorb on Ni single atoms, due to the presence of oxygen-rich defects, the anti-bonding state formed by the hybridization of the Ni atom *d* orbitals and H_2O molecular orbitals is occupied [Fig. 25(a)], leading to weak adsorption strength of H_2O and a correspondingly low dissociation barrier. Under thermal excitation at 600 K, H_2O dissociates into H and OH, causing the oxygen vacancies near the Ni exposure site to be covered by OH, which in turn deactivates the catalyst. However, under photoexcitation, the Ni atom site accumulates holes transferred to the H_2O molecule, weakening the adsorption between Ni and H_2O. As a result, the dissociation of H_2O to form O does not fill the oxygen vacancies around the Ni site, ensuring the stability of the catalyst. This mechanism has also been confirmed experimentally. In another study, Liu *et al.*[255] compared the dissociation of CO_2 driven directly by hot carriers generated via plasmonic excitation in metal clusters

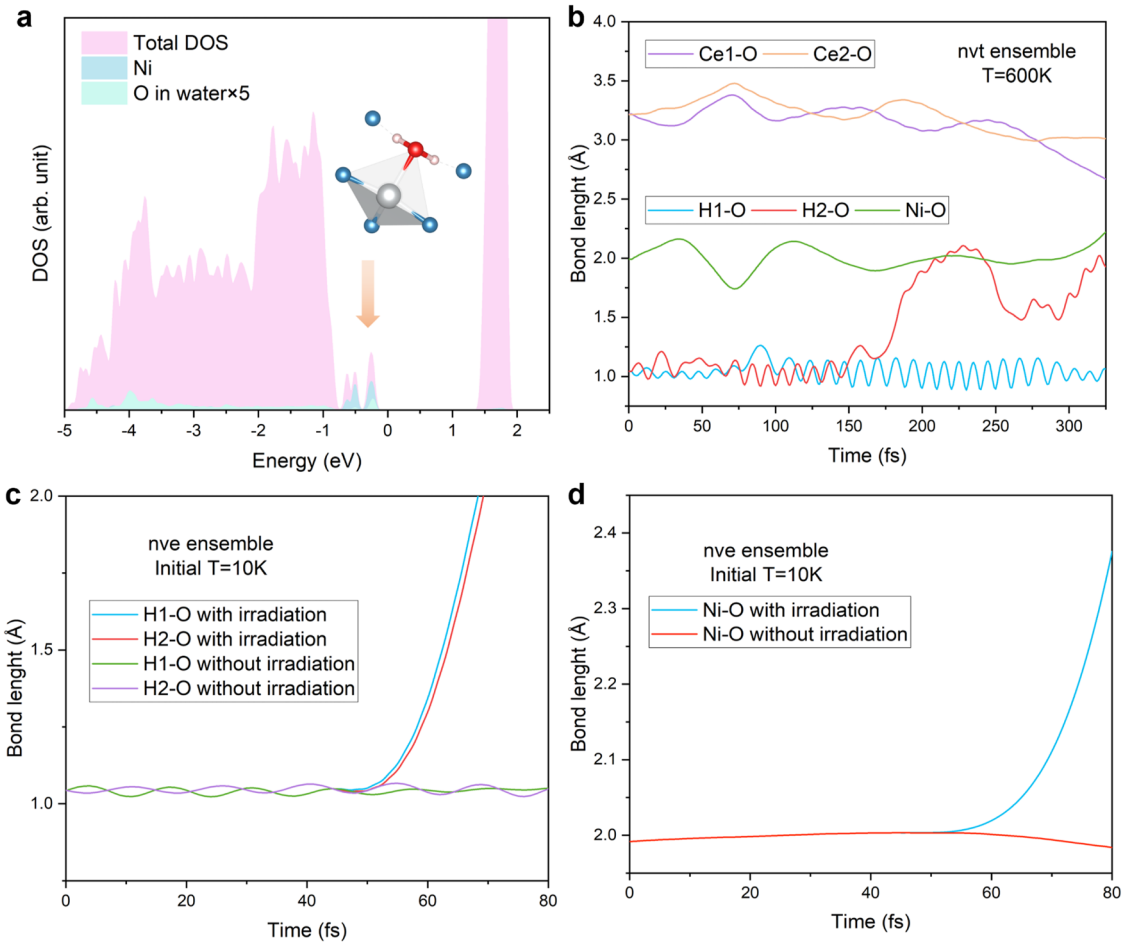

FIG. 25. Real-time TDDFT applications on photocatalysis.[251] (a) Projected density of states for H_2O on Ni single atom site load on CeO_2. (b) Bond length of thermal dissociation of H_2O under 600 K. (c) and (d) Bond length of light-induced dissociation of H_2O. Adapted with permission from Ren *et al.*, Nat. Commun. **15**, 4675 (2024). Copyright 2024 Springer Nature.

with the thermochemical reduction of CO_2 by H species. They used TDDFT to elucidate the mechanisms and characteristic timescales of both processes and provided experimental evidence from *in situ* infrared spectroscopy.

V. ABACUS IN THE OpenLAM PROJECT

As the collection of quantum mechanical data progressively encompasses the entire periodic table, the Deep Potential team has launched an ambitious project named the Large Atomic Model (LAM) based on the practice of the deep potential with attention (DPA) pre-training model.[256,257] Emphasizing open scientific collaboration, this initiative has been formally designated as the OpenLAM project,[41] reflecting its commitment to transparent development and community-driven progress. ABACUS serves as the cornerstone computational platform for generating cost-effective yet high-fidelity first-principles data to support OpenLAM's development. Through heterogeneous algorithm optimization specifically tailored for plane wave basis solutions of the Kohn–Sham equations, the software achieves remarkable efficiency gains in data generation.

A. APNS project

For those DFT codes that require pseudopotentials, several open-source codes for generating pseudopotentials are available, enabling users to tailor pseudopotentials to their specific requirements.[201,258] For LCAO calculations using ABACUS, it is crucial to validate both the NAO basis set and the pseudopotentials before practical applications. To address the above issues, we have initiated the "ABACUS Pseudopotential Numerical Atomic Orbital Square" (APNS) project.

Systematic verification of ABACUS remains essential in the APNS project to ensure reliable software development and maintain efficient high-throughput calculations. This aligns with growing research on validating DFT codes.[111,187,189,259] Major databases such as Materials Project,[260] Materials Cloud,[261] and

Computational Materials Repository[262] have improved DFT practices. These datasets help balance accuracy and efficiency in DFT calculations while establishing code implementation standards. The APNS workflow enables automated high-throughput testing with optional user interaction. It evaluates pseudopotentials and NAO basis sets across predefined and customizable systems, compatible with both PW and LCAO methods. The system also maintains a results database for test verification and validated pseudopotential/orbital file downloads. Here, we list some examples done in the APNS project.

Figure 26 demonstrates the standardized testing workflow, where the workflow has conducted efficiency and accuracy evaluations for multiple norm-conserving pseudopotential families, including SG15,[263] PseudoDojo,[264] PD03/PD04[265]

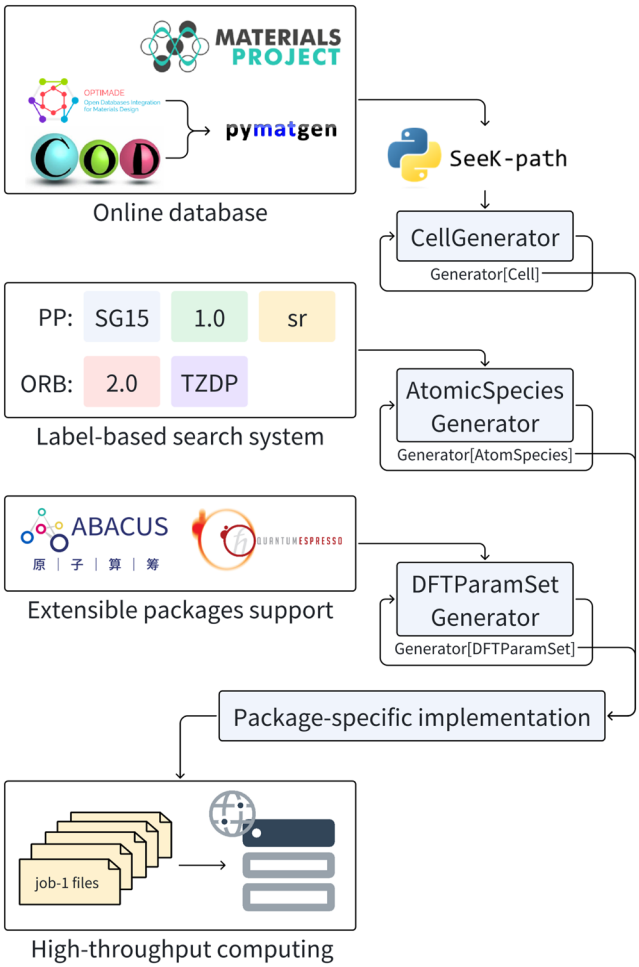

FIG. 26. Workflow chart of ABACUS Pseudopotential-Numerical atomic orbital Square automatic (APNS), a high-throughput workflow incorporating structure generation, download and management [interfaced with online open crystal structure databases Materials Project,[260] Optimade,[270] Crystallography Open Database (COD),[271] etc.], symmetry analysis (interfaced with SeeK-path[272,273]), modular and extensible software input generation (ABACUS and Quantum ESPRESSO[14]), and remote high-throughput computing support.

(with version variations and semi-core configurations), CP2K's Goedecker–Teter–Hutter pseudopotentials,[266] and three ultrasoft types (pslibrary 0.3.1/1.0.0,[267] GBRV v1.5[268,269]). This workflow has additionally supported ABACUS feature development, such as DFT+U implementation and ultrasoft pseudopotential compatibility.

The PW kinetic energy cutoff critically determines calculation accuracy, but excessively high values hinder computational efficiency. To address this trade-off, we established a systematic protocol for optimizing pseudopotentials through convergence testing across key parameters. This process involves two-phase validation. First, convergence testing of cutoff energies (20–300 Ry range) using stable crystal structures from Materials Project,[261] Crystallography Open Database,[271] and Optimade.[270] Second, equation of state (EOS) verification with optimized cutoffs. Three physical properties, including Kohn–Sham energy, lattice pressure (stress tensor trace), and band structure similarity metrics,[274] were used as convergence criteria across pseudopotential types.

EOS tests were performed using non-spin-polarized calculations, with k-sampled at a spacing of 0.06 bohr^{-1} in the Brillouin zone for all elements. The crystal volumes V range from 94% (V_m) to 106% (V_M) with a 2% step size. The kinetic energy cutoff for the plane wave (PW) basis is set to the maximum of the converged values for all elements in the tested system. The Δ value,[275] defined as

$$\Delta(a,b) = \sqrt{\frac{1}{V_M - V_m}\int_{V_m}^{V_M} [E_a(V) - E_b(V)]^2 \mathrm{d}V}, \qquad (113)$$

serves as a scalar indicator to quantify the difference between EOS profiles derived from pseudopotential and all-electron calculations (denoted by a and b, respectively). The continuous integral in Eq. (113) is evaluated over the curve fitted using the Birch–Murnaghan equation,[276] where $E_a(V)$ and $E_b(V)$ represent the Kohn–Sham energies relative to their equilibrium values.

We constructed three Bravais lattices for each element, including bcc (Body-Centered-Cubic), fcc (Face-Centered-Cubic), and diamond structures. We calculate E–V datasets and compare them with the all-electron results reported in Ref. 111. The converged kinetic energy cutoffs and corresponding Δ values for all available elements in the SG15 1.0 pseudopotential[201] are shown in Fig. 27.

For the NAO basis set, we conducted precision tests. Similar to plane wave (PW) calculations, precision is indicated by the EOS; in addition, the energy difference at the minimum of the EOS profile can serve as an indicator of basis set completeness. For ABACUS LCAO calculations, reliability verification tests for any given pseudopotential are often hindered by the relatively complex and time-consuming NAO generation procedure, which requires sophisticated experience and insights. This makes a rapid, highly automated orbital generation code necessary. Furthermore, as the precision and efficiency of NAOs are expected to improve continuously, a platform for orbital generation algorithm development is needed. Therefore, an open-source subproject, "ABACUS-ORBGEN," has been included as a development component of APNS. The current implementation remains based on the algorithms proposed in Refs. 18 and 24 but includes features such as automatic setting of orbital configurations for pseudopotentials generated with ONCVPSP codes,

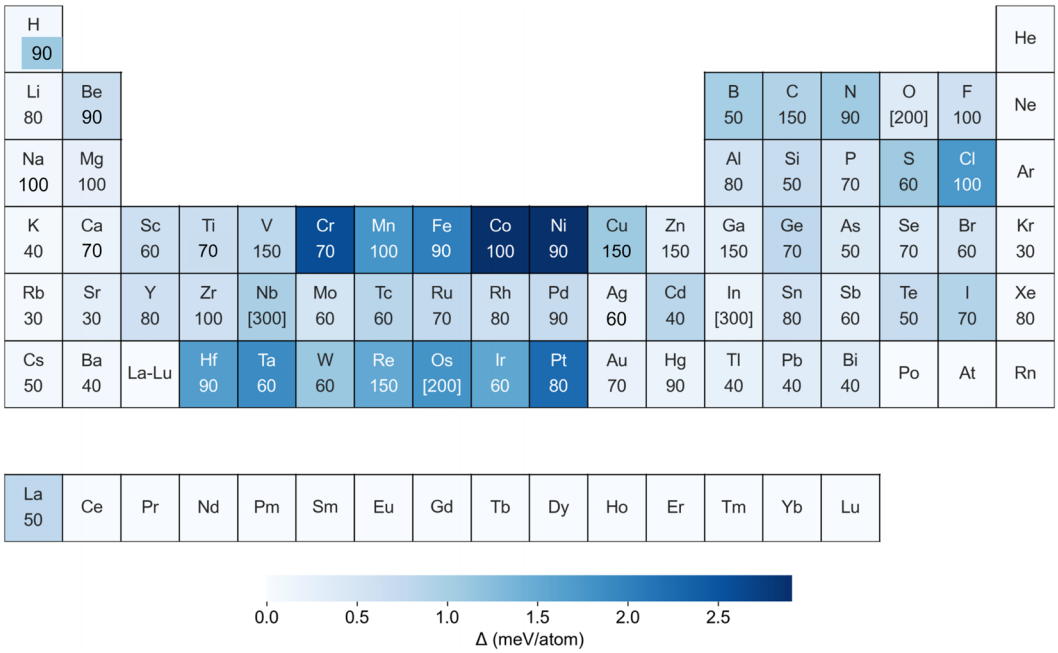

FIG. 27. Efficiency and precision tests on SG15 1.0 pseudopotentials using the PW basis of ABACUS. The number below the element symbol labels the converged kinetic energy cutoff (E_c^{kin}) under three thresholds: Kohn–Sham energy (<1 meV/atom), pressure (<0.1 kbar), and band similarity (<10 meV). Large E_c^{kin} values, which are enclosed by brackets, are results from the oscillation or slow convergence with respect to pressure. The color of each block indicates the Δ value calculated with converged E_c^{kin} averaged over bcc, fcc, and diamond structures. Blocks of elements whose pseudopotentials are not available are left empty.

automated improvement of orbital transferability through a series of bond length scans and potential curve fitting tasks, and a quick orbital quality estimation function.

B. UniPero model

Wu *et al.*[277] utilized "modular development of deep potential" (ModDP)[278] to create a universal interatomic potential for perovskite oxides (UniPero) using a deep neural network with a self-attention mechanism. This potential spans 26 types of perovskite oxides involving 200 components and 14 metal elements. All DFT calculations were performed with ABACUS. As depicted in Fig. 28(a), they first used DP-GEN to obtain a converged DPA-1 model[256] for three-element systems such as $PbTiO_3$ and $SrTiO_3$. Then, the converged dataset served as a starting point for DP-GEN to improve DPA-1 for four-element perovskite systems such as $Pb_xSr_{1-x}TiO_3$ and $PbZr_xTi_{1-x}O_3$. Ultimately, the final DPA-1 model (UniPero) can describe six-element perovskite systems, including the ternary solid solution $Pb(In_{1/2}Nb_{1/2})O_3$–$Pb(Mg_{1/3}Nb_{2/3})O_3$–$PbTiO_3$ (PIN–PMN–PT). UniPero functions as a universal interatomic potential, effectively modeling a wide range of perovskites through molecular dynamics simulations.

The $PbTiO_3/SrTiO_3$ (PTO/STO) superlattices serve as a model system for exploring real-space topological textures, including flux closures, vortices, skyrmions, and merons. The authors tested the DPA-1 model by simulating strain-driven topological evolution in the PTO/STO superlattice. Figure 28(b) illustrates a $40 \times 20 \times 20$ supercell, containing 80 000 atoms, employed to model a $(PTO)_{10}/(STO)_{10}$ superlattice. At a strain state where the in-plane lattice constants are a_{IP} = 3.937 Å and a_{IP} = 3.930 Å, the equilibrium state at 300 K obtained with Deep Potential Molecular Dynamics (DPMD) simulations adopts an ordered polar vortex lattice with alternating vortex and antivortex [Fig. 28(c)]. As the in-plane strain increases to a_{IP} = 3.950 Å, the vortex cores shift toward the PTO/STO interfaces [Fig. 28(b)]. Finally, at a large tensile in-plane strain (a_{IP} = 3.955 Å), it becomes the periodic electric dipole waves characterized by head-to-tail connected electric dipoles in the form of a sine function [Fig. 28(e)]. These results agree with the experimental observations[279] and previous MD simulations.[278]

C. DPA-Semi model

Liu *et al.*[280] generated over 200 000 DFT data for 19 bulk semiconductors ranging from group IIB to VIA, namely, Si, Ge, SiC, BAs, BN, AlN, AlP, AlAs, InP, InAs, InSb, GaN, GaP, GaAs, CdTe, InTe, CdSe, ZnS, and CdS. All of the DFT calculations were performed with the ABACUS v3.2 package with the Perdew–Burke–Ernzerhof (PBE)[61] exchange–correlation functional. The triple-zeta plus double polarization (TZDP) NAO basis sets were used for all DFT calculations. The atomic datasets are adopted as training data to generate an attention-based deep potential model using the DPA-1 method,[256] namely, the DPA-Semi model. Figure 29 shows the procedures for developing the DPA-Semi model.

To validate the accuracy of the DPA-Semi model, we find the energy RMSEs of the BAs system are the smallest (0.004

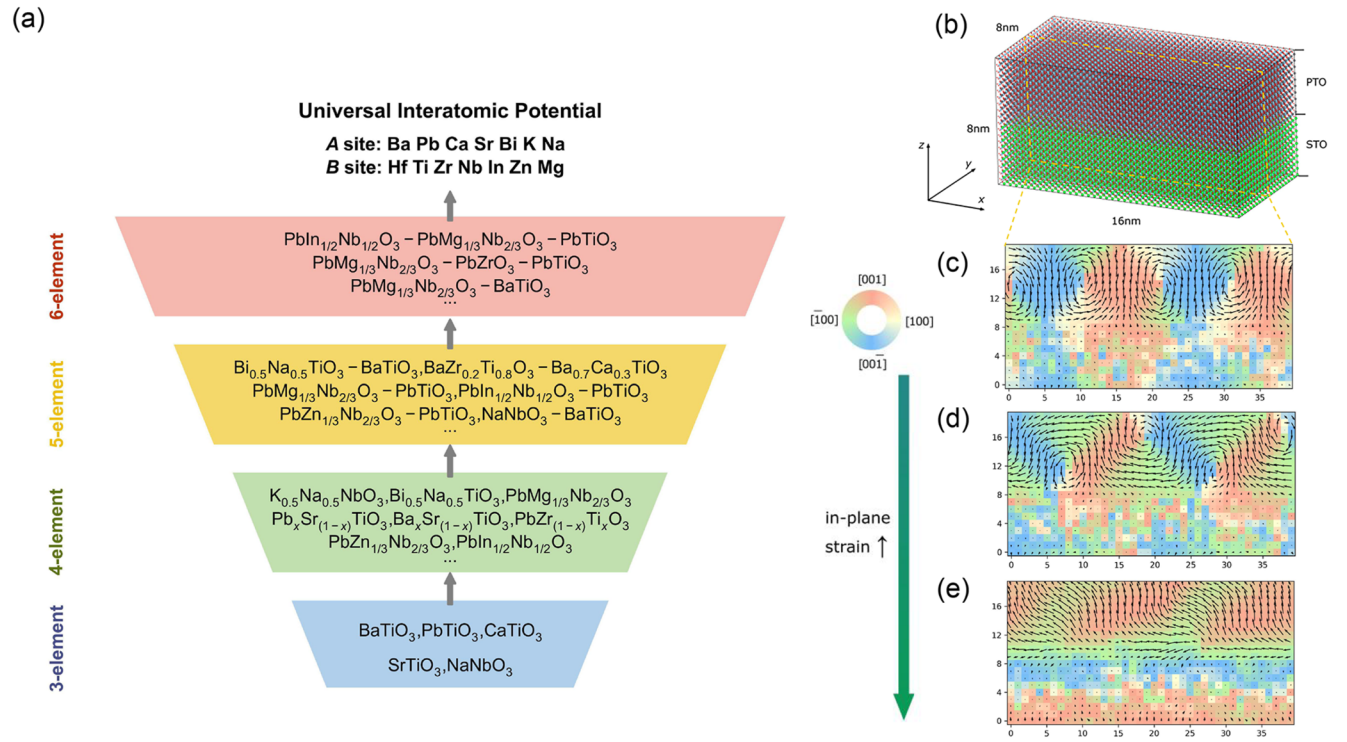

FIG. 28. (a) Workflow for developing a universal force field of perovskite oxides. Adapted with permission from Wu *et al.*, Phys. Rev. B **108**, L180104 (2023). Copyright 2023 American Physical Society. (b) $(PTO)_{10}/(STO)_{10}$ superlattices. Unipero predicts an in-plane strain-induced transition from (c) ordered polar vortex lattice to (d) shifted polar vortex lattice, and to (e) electric dipole waves.

eV/atom), while the force RMSEs of the InSb system are the smallest (0.11 eV/Å). For the lattice constants, bulk moduli, and elastic constants, the results from DPA-Semi are in excellent agreement with the DFT results, as the bulk moduli data are compared in Fig. 30. This work provided reliable evidence that the DPA-Semi model can be readily employed to study several semiconductor systems with *ab initio* accuracy.

D. DPA-1, DPA-2, and DPA-3

The DPA-1 model[256] is a universal machine learning interatomic potential that leverages the attention mechanism for molecular and materials modeling. Trained on the OC20 benchmark dataset and specialized materials systems, including aluminum–magnesium–copper alloys, high-entropy alloys, and solid-state electrolytes, this architecture achieves robust transferability across diverse atomic environments. With coverage spanning 56 elements in the periodic table, DPA-1 employs a pretraining-fine-tuning paradigm. The attention-based design supports first-principles accuracy while maintaining computational efficiency comparable to classical force fields.

The DPA-2 model[257] employs a multi-task learning framework that effectively integrates datasets from diverse DFT sources. This architecture substantially reduces the model's dependence on data uniformity, enabling the utilization of datasets generated by different methods. Notably, the pretraining phase of DPA-2 incorporates systematic learning of chemical compositions and spatial configurations, which dramatically reduces the demand for task-specific fine-tuning data in downstream applications.

The recently developed DPA-3[281] constructs a hierarchical graph neural network architecture based on line graph transformations, demonstrating substantial improvements in scaling law adherence and cross-dataset generalization capabilities. During the development of both DPA-2 and DPA-3 iterations, the ABACUS software served as a critical computational infrastructure, facilitating DFT calculations across diverse material datasets. Here, are two examples.

First, based on DFT calculations performed using ABACUS, we are developing general machine-learning-based potential models for alloys, covering 53 elements in the periodic table. The elements are Li, Na, K, Be, **Mg**, Ca, Sr, Sc, **Y**, La, **Ti**, **Zr**, **Hf**, **V**, **Nb**, **Ta**, **Cr**, **Mo**, **W**, **Cu**, Ag, Au, **Zn**, Cd, **Mn**, **Re**, **Fe**, **Co**, **Ni**, Os, Ir, Pt, Rh, Ru, Pd, Ce, Pr, Nd, Sm, Gd, Tb, Dy, Ho, Er, Tm, Lu, **Al**, Ga, In, Si, Ge, Sn, and Pb, where the bold ones are commonly used in structural alloys. The specific pseudopotentials utilized for these elements are listed in Ref. 282, and the calculations were performed efficiently by the ABACUS package on the Deep Computing Unit (DCU) hardware. In particular, the DP-GEN and Alloy Property EXplorer (APEX) workflows generated various structures,[283,284] including perfect and perturbed crystal structures, vacancies, interstitials, and surfaces of metals

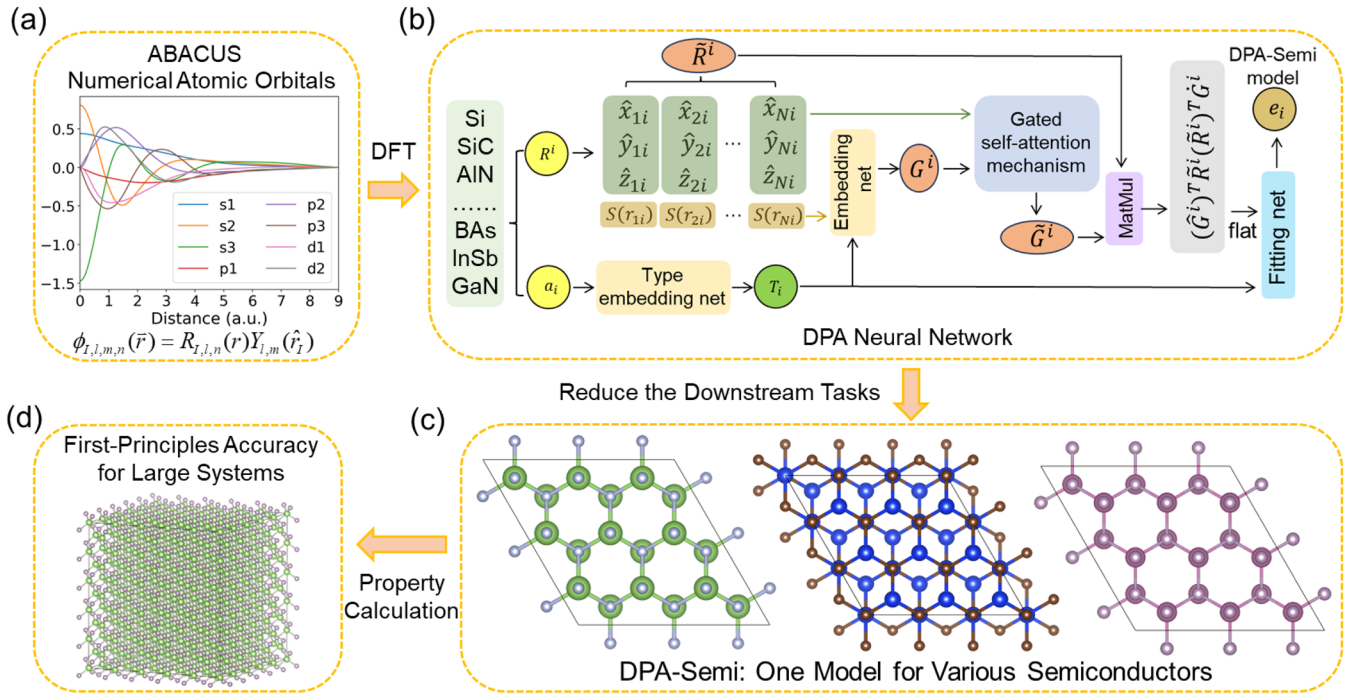

FIG. 29. Procedures for developing the DPA-Semi model. (a) Generate atomic datasets using the ABACUS package based on the numerical atomic orbitals as a basis set. (b) Generate the DPA-Semi model via the gated self-attention mechanism based on the DFT atomic datasets. (c) The DPA-Semi model can be used for various kinds of semiconductors and reduce the computational costs of downstream tasks. (d) The DPA-Semi model is readily applied to calculate properties of large systems with GGA quality accuracy. Adapted with permission from Liu *et al.*, J. Chem. Theory Comput. **20**(13), 5717–5731 (2024). Copyright 2024 American Chemical Society.

and alloys. Some structures were selected through the concurrent learning workflow in DP-GEN and then labeled by ABACUS, resulting in a training dataset of ~24 000 entries. By integrating previous training datasets from AI Square and the OpenLAM project,[41] the latest general LAM for alloys achieved a root mean square error (RMSE) of ~26 meV/atom for energies and ~0.20 eV/Å for atomic forces across the 53 metals and their alloys. This general LAM for alloys demonstrates superior performance in predicting various properties, including lattice parameters, elastic constants, point defects, and surface formation energies, compared to other LAMs.[285] ABACUS has proven to be a stable and reliable DFT workhorse for diverse structures covering these 53 elements.

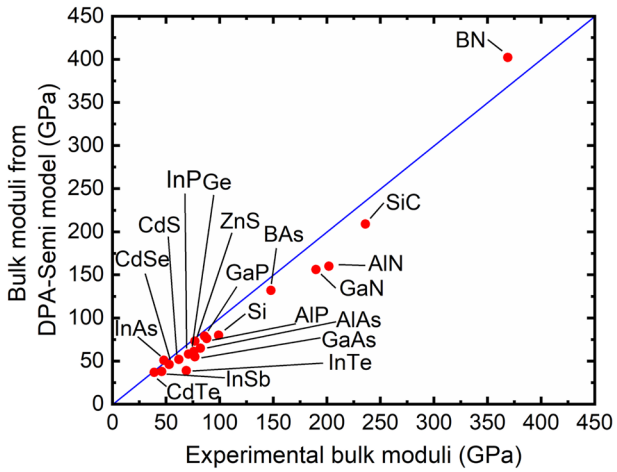

FIG. 30. Predicted bulk moduli of various semiconductors by the DPA-Semi model and available experimental data. Adapted with permission from Liu *et al.*, J. Chem. Theory Comput. **20**(13), 5717–5731 (2024). Copyright 2024 American Chemical Society.

Second, during the construction of the dataset for the DPA-1 and DPA-2 models of high-pressure superhydrides, all labels were calculated using ABACUS with plane wave basis sets. The thermodynamic stability of the discovered structures was confirmed by their energies above the convex hull, which was determined through structure optimization results from ABACUS. Dynamic stability was assessed using the phonon dispersion spectrum calculated by phonopy,[286,287] with all forces calculated by ABACUS. Our DFT calculations were performed on DCU hardware, significantly enhancing the efficiency of SCF calculations compared to traditional CPUs. We obtained a dataset comprising 218 349 data frames, covering 29 elements and a pressure range of 150–250 GPa. Utilizing these data, the DPA-1 model achieved a training RMSE of 48.1 meV/atom for energy and 334.8 meV/Å for force. The DPA-2 model achieved a training RMSE of 55.2 meV/atom for energy and 298.8 meV/Å for force. On the testing dataset, the DPA-1 model yielded an RMSE of 37.6 meV/atom for energy and 171.4 meV/Å for force, while the DPA-2 model yielded an RMSE of 37.4 meV/atom for energy and 122.1 meV/Å for force. Given the large dataset required for the

superhydrides model, ABACUS proved to be the most economical DFT software available. The high-quality training results further attest to the stable performance of ABACUS.

VI. INTERFACES TO OTHER PACKAGES

A. DeePKS-kit

DeePKS-kit[33,34] is an innovative computational framework designed to bridge machine learning with quantum-mechanical simulations. The software integrates deep learning techniques with the Kohn–Sham equations to refine exchange–correlation functionals and can be used with ABACUS or PySCF.[13] By training a neural network on high-fidelity quantum chemistry data, DeePKS-kit dynamically corrects errors in conventional DFT approximations, enabling predictions of electronic properties with near-chemical-accuracy at a fraction of the computational cost.

By adopting both the DeePKS-kit and ABACUS packages, we optimize the DeePKS model in two iterative steps. As shown in Fig. 31, $L(\omega)$ is the loss function. Loss function $L(\omega)$ can be composed of various energetic terms, including the energy E, the atomic force $\mathbf{F}$, the stress tensor σ, and the bandgap ε_g of the interested system. The first step is the SCF step, where we fix parameters $\{\omega^*\}$ in the DeePKS model and solve the Kohn–Sham equation to obtain the ground state electronic wave function. The second step is the TRAIN step, where the electronic wave functions are fixed and the model parameters $\{\omega\}$ are optimized. These two steps repeat until convergence is reached.[33]

B. DeePMD-kit

DeePMD[31,288] is a widely used[39] machine-learning molecular dynamics method based on the neural-network potential. ABACUS has an interface with the DeePMD-kit package,[32,97] allowing its deployment as a molecular dynamics engine in executing DeePMD simulations. Trained on system energy, atomic forces, and lattice stress derived from DFT calculations, this neural network potential enables DeePMD to replicate the potential energy surface with first-principles accuracy. Since the neural network potential is computationally more efficient than the DFT method, DeePMD can simulate large systems at a long time scale, which is barely accessible for AIMD simulations.

Regarding training, DeePMD requires a large number of atomic configurations with system energies, atomic forces, and optionally virial tensors calculated by the DFT software as the training data. Within ABACUS, these requisite data can be obtained either from the self-consistent calculations (Sec. II B) or from the AIMD simulations (Sec. II D). The Python package **dpdata**[289] for atomic simulation data manipulation facilitates convenient transfer of data to the DeePMD training data format.

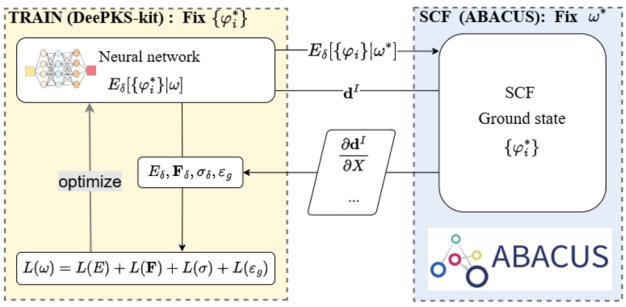

FIG. 31. Workflow of training a DeePKS model. The blue and yellow boxes represent the SCF step performed by the ABACUS software and the TRAIN step performed by the DeePKS-kit software, respectively. These two steps iterate over each other until convergence. The neural network can be optimized considering energy E, atomic force $\mathbf{F}$, stress σ, and bandgap ε_g.

C. DP-GEN

To develop the Deep Potential Energy Surface (PES) more efficiently, the DP-GEN (Deep Potential Generator) framework[283,290] employs a recurrent, adaptive learning scheme that systematically refines machine-learned interatomic potentials. The process begins with a minimal initial dataset of atomic configurations labeled via DFT calculations. Through an iterative active learning loop, DP-GEN trains Deep Potential models with varied initializations to explore new regions of the configuration space. During MD simulations, the framework identifies configurations where model predictions diverge significantly and prioritizes these for further DFT validation. This targeted sampling ensures that the training dataset grows strategically, focusing on physically relevant yet under-represented regions of the PES.

The workflow integrates automated DFT computations to validate candidate configurations. DP-GEN has interfaces with first-principles software such as ABACUS, VASP, and Quantum ESPRESSO. As new DFT data points are added, the Deep Potential models undergo retraining, progressively improving their accuracy across diverse atomic environments. The process continues until predefined error thresholds for forces and energies are met. A key innovation of DP-GEN is its parallelized sampling strategy, which enables simultaneous exploration of multiple trajectories to efficiently map high-dimensional configuration spaces while minimizing redundant DFT calculations.

The DP-GEN framework has proven particularly effective for complex systems such as multicomponent alloys,[291,292] chemical reaction pathways,[293,294] and phase transitions under extreme conditions,[295,296] where traditional sampling methods struggle to capture rare events or subtle energy landscapes. Open-source and modular by design, DP-GEN supports customization for specific materials or molecules, offering a versatile tool for accelerating the development of robust, quantum-mechanically informed potentials.

D. DeepH

The deep-learning density functional theory Hamiltonian (DeepH) method is a neural network approach based on equivariant graph neural networks for modeling the DFT Hamiltonian as a function of material structure.[297] Leveraging the sparsity of the Hamiltonian matrix under NAOs and its compatibility with Walter Kohn's "quantum nearsightedness principle,"[298] the DeepH method can learn from training data of small structures to infer electronic Hamiltonians of large structures, achieving high prediction accuracy with linear-scaling computational cost. The predicted Hamiltonian may be subsequently utilized for post-processing

to evaluate properties, including band structures, optical properties, and response properties from density functional perturbation theory, etc.[297,299,300]

The interface between ABACUS and DeepH was developed in 2022, shortly after the invention of the DeepH approach in 2021. The interface ensures compatibility between ABACUS and various versions of DeepH, including DeepH-pack,[297,301] DeepH-E3,[299,302] and DeepH-2.[303] Among these, DeepH-E3 stands out as the most stable open-source implementation to date and has been utilized with ABACUS in several example studies.[225,302,304] The ABACUS–DeepH interface is versatile, supporting spin–orbit coupling and magnetic systems, and facilitates ABACUS's integration with xDeepH—a specialized variant of DeepH for predicting the electronic structures of magnetic materials.[305] To address the modified sparsity patterns in hybrid DFT Hamiltonians, a dedicated toolkit, named DeepH-hybrid, has been developed, which verified DeepH's applicability to hybrid-functional Hamiltonians generated by ABACUS.[225,306] An interface between ABACUS and DeepH-DFPT (a generalization of the DeepH approach for deep-learning density functional perturbation theory) is currently under development to accelerate calculations of electron–phonon coupling.[300] In addition, a recently developed "Hamiltonian Projection and Reconstruction to atomic Orbitals" (H-PRO) method can transform the DFT Hamiltonian of plane wave basis into localized basis, making the DeepH compatible with the plane wave mode of ABACUS.[307] Very recently, a universal materials model (UMM) of DeepH, named DeepH-UMM, has been developed, demonstrating exceptional transferability across a wide range of material structures composed of various elements.[308] Given ABACUS's versatility, further development of DeepH-UMM in conjunction with ABACUS holds significant promise for advancing materials discovery.

The current ABACUS-DeepH interface is available on GitHub.[301] For inference with trained DeepH models, ABACUS provides an efficient method for generating the overlap matrix, from which the Hamiltonian can be predicted by DeepH. It is important to note that the overlap and Hamiltonian matrices are assumed to share the same sparsity pattern in DeepH. To ensure clarity, fixing such sparsity patterns with the tools provided in DeepH-hybrid is recommended.[306]

E. DeePTB

DeePTB is an open-source package that leverages deep learning to accelerate *ab initio* electronic simulations.[309,310] Its integration with ABACUS creates a powerful synergy, combining first-principles calculations with advanced machine learning techniques for efficient large-scale electronic structure predictions. Notably, it has demonstrated the capability to simulate systems containing up to millions of atoms,[309] a scale previously unattainable with traditional methods.

Figure 32 illustrates the ABACUS–DeePTB workflow. ABACUS performs DFT calculations on training structural data obtained from crystal databases or molecular dynamics simulations, generating essential quantum mechanical data as labels, including energy eigenvalues, NAOs basis Hamiltonian, overlap, and density matrices. DeePTB utilizes this ABACUS-generated data to train two key models: the DeePTB-SK[309] and DeePTB-E3[310] models. The DeePTB-SK model uses energy eigenvalues to develop an improved Slater–Koster TB model for efficient electronic structure prediction, while the DeePTB-E3 model, based on the SLEM (Strictly Localized Equivariant Message-passing) approach, predicts quantum operators, including the Hamiltonian, overlap, and density matrices.

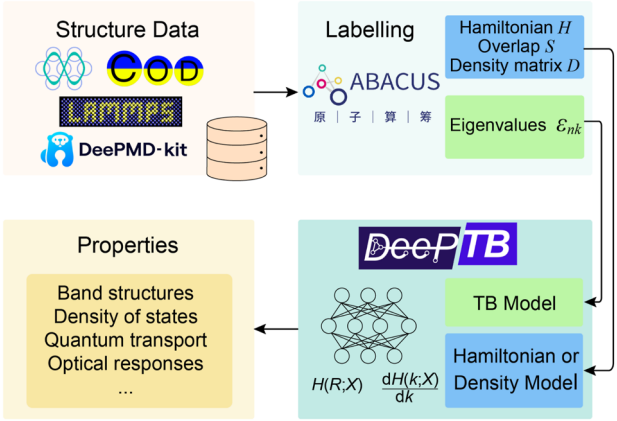

FIG. 32. Workflow chart of ABACUS–DeePTB integration for deep learning-based TB and quantum operator (Hamiltonian, overlap, and density matrices) predictions.

This integrated approach significantly enhances the efficiency and scalability of electronic structure simulations, enabling the study of complex and large-scale material systems previously limited by computational constraints. For instance, recent work combining DeePTB with non-equilibrium Green's function (NEGF) methods has demonstrated unprecedented efficiency in quantum transport simulations of large-scale nanodevices.[311] The ABACUS–DeePTB collaboration demonstrates the potential of combining traditional DFT methods with cutting-edge machine learning in computational materials science, opening new avenues for high-throughput materials discovery and design.

F. HamGNN

HamGNN (Hamiltonian Graph Neural Network) is an end-to-end model specifically designed for atomic orbital (AO)-based electronic Hamiltonian parameterization.[312] It inherently satisfies the symmetry requirements of rotation, parity, and translation. HamGNN parameterizes spin–orbit coupling (SOC) and magnetic interactions by incorporating physical principles, thereby accurately capturing the SOC effect and effectively describing the magnetic Hamiltonian across various materials.[313] Moreover, HamGNN enhances the accuracy and stability of band structure predictions through a two-stage training strategy: real-space pre-training followed by reciprocal-space fine-tuning, which effectively combines local atomic environments with global electronic behavior within the Brillouin zone. In practical applications—including the modeling of high-order Bi topological insulators,[314] Bi ferroelectric domain topological interface states,[315] and metal–oxide–semiconductor field-effect transistor (MOSFET) device design[316]—HamGNN has demonstrated both high computational efficiency and strong transferability.

The performance of HamGNN relies critically on high-quality training data, where ABACUS plays an essential role. ABACUS stands out as a key tool for building high-precision HSE Hamiltonian training databases, as it is one of the few DFT software packages based on numerical atomic orbitals that support HSE hybrid functionals. When combined with the cross-system transferability of the HamGNN model, this capability enables the development of a universal HSE Hamiltonian model covering the entire periodic table.[317] Recently, the Uni-HamGNN framework achieved universal modeling of SOC effects across the periodic table by decomposing the SOC Hamiltonian into spin-independent terms and SOC correction terms and employing a delta-learning strategy to fit them separately.[318] By incorporating a limited number of SOC Hamiltonian matrices from ABACUS, a universal SOC model with HSE-level accuracy can be further established using the delta-learning strategy. This approach, when applied in the training of the universal HSE SOC model, can significantly reduce the expensive computational cost of HSE SOC calculations.

These advancements in universal Hamiltonian modeling open up numerous practical applications with significant computational advantages. Using the universal HamGNN models trained on HSE Hamiltonian matrices as a computational engine can substantially accelerate the computation of carrier mobility and superconductivity-related electron–phonon coupling properties at the hybrid functional level.[319] Furthermore, HamGNN can accurately predict Hamiltonians and non-adiabatic coupling vectors (NACVs) that continuously change with atomic displacement, enabling dynamics simulations of excited states at HSE precision.[320] Looking forward, the deepening integration of ABACUS and HamGNN holds promise for developing even more powerful, universal electronic Hamiltonian prediction models, driving the materials computation field toward new horizons of enhanced efficiency and intelligence. The interface for ABACUS and HamGNN is available online.[321]

G. PYATB

PYATB (PYthon *Ab initio* Tight-Binding simulation package) is a Python package based on an *ab initio* tight-binding Hamiltonian, designed as a tool for calculating and analyzing the electronic structures of materials.[322] It can be viewed as a post-processing program for ABACUS. When ABACUS completes the SCF calculations and generates the tight-binding Hamiltonian, PYATB utilizes this Hamiltonian to perform electronic property calculations. This eliminates the need for the cumbersome construction of Maximally Localized Wannier Functions (MLWFs) while strictly preserving the Hamiltonian's symmetry, making it particularly well-suited for high-throughput workflows in electronic structure calculations of various materials. Currently, PYATB mainly offers three functional modules, i.e., bands, geometric, and optical. This allows ABACUS, in combination with PYATB, to compute basic band structures, fat bands, and projected density of states (PDOS). In addition, it can analyze the Berry curvature and Chern number of topological materials,[323,324] as well as compute first- and second-order optical responses such as optical conductivity, shift current, second harmonic generation,[325–327] and Berry curvature dipole.[328,329]

Once the Hamiltonian matrix $\boldsymbol{H}(\mathbf{k})$ and the overlap matrix $\boldsymbol{S}(\mathbf{k})$ are given, the element dipole matrix is given by

$$A^{\mathbf{R}}_{\mu\nu}(\mathbf{k}) = \sum_{\mathbf{R}} e^{i\mathbf{k}\cdot\mathbf{R}} \langle \phi_{\mu 0} | \mathbf{r} | \phi_{\nu \mathbf{R}} \rangle. \tag{114}$$

Using these input parameters, PYATB solves the following generalized eigenvalue problem of Eq. (82). Subsequently, based on the wave functions, the Berry curvature[323,330] can be calculated. This allows for the calculation of various topological and optical properties of materials. One can refer to Ref. 322 for the implementation details.

H. Hefei-NAMD

Hefei Non-Adiabatic Molecular Dynamics (Hefei-NAMD) is an *ab initio* simulation suite for studying excited carrier dynamics in condensed matter systems. It combines real-time time-dependent density functional theory (TDDFT) with the fewest-switches surface hopping scheme and classical-path approximation. Hefei-NAMD has been used to investigate processes such as charge transfer, electron–hole recombination, spin dynamics, and exciton dynamics.[331–334] It allows the study of excited carrier dynamics in energy, real, and momentum spaces, while also exploring interactions with phonons, defects, and molecular adsorptions, providing valuable insights into ultrafast dynamics at the atomic scale. Hefei-NAMD works by interfacing with other *ab initio* codes, e.g., VASP, ABACUS, etc. Figure 33 shows the flow chart of the simulation using Hefei-NAMD interfaced with ABACUS.

I. PEXSI

PEXSI (Pole EXpansion and Selected Inversion)[74,75] offers an efficient approach for solving the KS equation while circumventing the computational limitations inherent in conventional diagonalization techniques. This method directly computes the real-space density matrix through a P-term pole expansion of the Fermi–Dirac function, expressed as

$$f(\boldsymbol{H} - \mu \boldsymbol{S}) \approx \mathrm{Im} \sum_{l=1}^{P} \omega_l^{\rho} [\boldsymbol{H} - (z_l + \mu)\boldsymbol{S}]^{-1}, \tag{115}$$

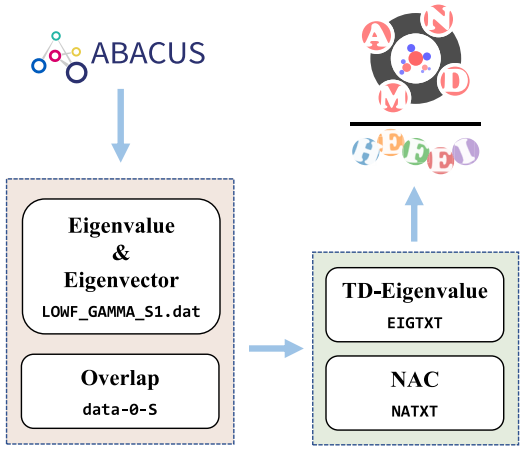

FIG. 33. Workflow chart of Hefei-NAMD interfaced with ABACUS.

where $\boldsymbol{H}$ denotes the Hamiltonian matrix, $\boldsymbol{S}$ is the overlap matrix, and z_l and ω_l correspond to the precomputed poles and weights of the complex contour integration, respectively. The numerical stability of this expansion is ensured through careful selection of these parameters. The computationally intensive matrix inversion operations are efficiently performed using the selected inversion algorithm.

Notably, PEXSI exhibits superior computational scaling compared to traditional diagonalization methods. While standard diagonalization scales cubically as $O(N^3)$, PEXSI achieves at most quadratic scaling $[O(N^2)]$, where N is the dimension of the matrix. The method's architecture features a two-level parallelization scheme, incorporating both pole expansion parallelism and selected inversion parallelism, thereby demonstrating exceptional scalability. ABACUS has implemented an interface to the parallel version of PEXSI for solving the KS equation expanded with the NAO basis.

J. Other packages

ASE (Atomic Simulation Environment) comprises a comprehensive suite of tools and Python modules designed for setting up, manipulating, executing, visualizing, and analyzing atomic simulations.[335] We have developed an ABACUS calculator[336] that interfaces with ASE (version 3.23.0b1) and that enables seamless integration of ASE's robust functionalities for both pre-processing and post-processing tasks. Regarding pre-processing capabilities, the interface facilitates tasks such as converting structural files into various formats, generating k-point grids, etc. For post-processing, the integration with ASE empowers ABACUS users with advanced tools for visualizing and analyzing simulation results. Moreover, the self-consistent calculations of ABACUS can be combined with ASE's built-in optimization algorithms, facilitating structural relaxation procedures, conducting MD simulations under varying conditions, performing precise phonon calculations based on the finite displacement method, carrying out global optimization by genetic algorithm (GA), locating transition states (TS) of reactions by saddle point refinement, etc. For TS search, as an example, the nudged elastic band (NEB)[337–339] method and the dimer[340–343] method, which represent double-ended TS searching methods and single-ended TS methods, respectively, are implemented in ASE. In addition, some other enhanced NEB methods are coded in the ASE package, such as dynamic NEB[344] and AutoNEB.[345] Furthermore, there are other saddle point refinement algorithms implemented in ASE, and some of them show better performance, such as Sella.[346–348] With the above-mentioned methods available in ASE, ABACUS can be used for searching for transition states.

The ATST-Tools scripts suite[349] is prepared for handy usage of ABACUS and ASE in TS locating jobs (see the workflow in Fig. 34). Apart from directly using TS search tools in ASE, the cooperation of different TS search methods can be done due to ASE's coding flexibility, which leads to better TS locating functionality. One way is to first generate a rough TS by NEB, then utilize a single-ended method such as Dimer or Sella to optimize the TS in the target threshold, which incorporates the advantage of both methods.

Phonopy[286,287] is a versatile open-source package designed for calculating phonon and related lattice dynamics properties from first-principles calculations. With the addition of the ABACUS interface in Phonopy version 2.19.1, users can now adopt ABACUS to compute the electronic structures and force constants that Phonopy requires for its phonon calculations.[280,350]

ShengBTE[351] is an open-source package aimed at solving the linearized Boltzmann Transport Equation (BTE) for phonons, enabling the *ab initio* prediction of lattice thermal conductivity in bulk crystalline solids and nanowires. It goes beyond the relaxation-time approximation by explicitly incorporating three-phonon scattering processes and isotopic scattering, yielding predictive results without empirical fitting. ShengBTE requires inputs of second- and third-order interatomic force constants (IFCs), traditionally computed using DFT packages, often aided by

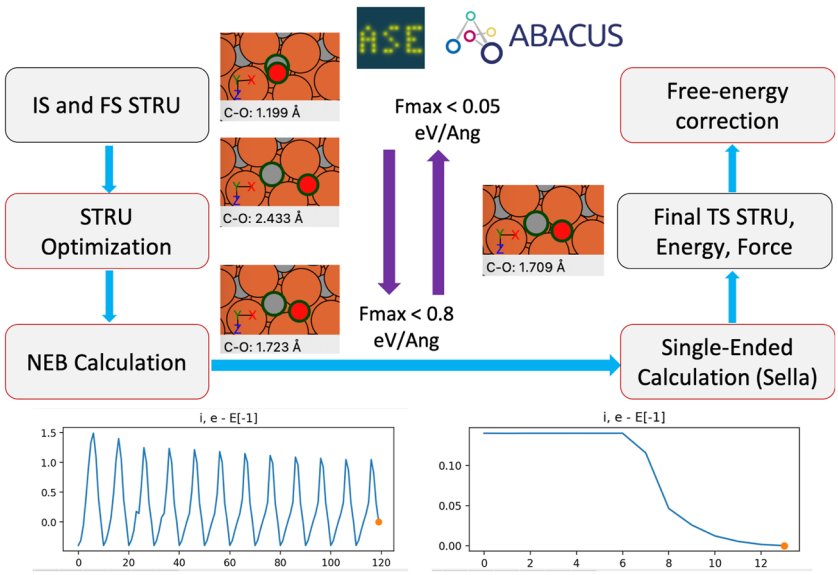

FIG. 34. Workflow chart of the NEB + Sella method for locating TS based on ASE and ABACUS; the red block denotes the usage of ABACUS as a calculator.

preprocessing tools. ABACUS can provide inputs for ShengBTE starting from v3.2.3.

TB2J[352] is an open-source Python package for automatic computation of magnetic interactions between atoms of magnetic crystals from density functional Hamiltonians based on Wannier functions or linear combinations of atomic orbitals. The program is based on Green's function method with the local rigid spin rotation treated as a perturbation.[353] The ABACUS interface has been added since TB2J version 0.8.0. With the Hamiltonian matrix $\mathbf{H}(\mathbf{k})$ and the overlap matrix $\mathbf{S}(\mathbf{k})$ obtained by an LCAO calculation, TB2J is able to compute the isotropic exchange, symmetric anisotropic exchange, and the Dzyaloshinskii–Moriya interaction (DMI). In 2024, Zhang *et al.*[354] studied $GeFe_3N$ by using ABACUS-TB2J, which helps them study the short-range order and strong interplay between local and itinerant magnetism in $GeFe_3N$.

Wannier90[355] is software designed for calculating maximally localized Wannier functions (MLWFs),[356] which facilitates cost-effective band structure calculations. MLWFs are often used to construct model Hamiltonians. The post-processing capabilities of Wannier90 enable the calculation of various properties, such as Berry curvature, Berry curvature dipole, and shift current.[355] In addition, MLWFs generated by Wannier90 can be analyzed for material surface states and topological properties using the Wannier Tools.[357] According to the standard scheme for generating maximally localized Wannier functions in Wannier90, ABACUS has implemented an interface compatible with the Wannier90 software. This interface allows ABACUS to generate the necessary files for Wannier90, including overlap files between the periodic parts of Bloch functions at neighboring $\mathbf{k}$-points, projection files of Bloch functions onto trial localized orbitals, eigenvalue files of the energy bands, and real-space distribution files of the periodic parts of Bloch functions.

APEX (Alloy Property EXplorer)[284] is a versatile and extensible Python package for general alloy property calculations. This package enables users to conveniently establish a wide range of cloud-native property-test workflows by utilizing ABACUS. APEX currently supports the calculations, including equation of state (EOS), elastic constants, surface energy, interstitial formation energy, vacancy formation energy, generalized stacking fault energy (Gamma line), and phonon spectra.

CALYPSO [Crystal structure AnaLYsis by Particle Swarm Optimization (PSO)][358] is software designed for the prediction of stable and metastable crystal structures. It employs advanced techniques such as particle swarm optimization (PSO) to efficiently explore complex potential energy surfaces. CALYPSO has an interface with ABACUS to compute accurate energies and forces during the structure search process. The combined CALYPSO-ABACUS workflow can be utilized for high-throughput structure prediction and inverse design of functional materials under specified chemical compositions and external conditions such as pressure.

USPEX (Universal Structure Predictor: Evolutionary Xtallography)[359] represents a powerful methodology for crystal structure prediction. USPEX employs evolutionary algorithms to efficiently predict stable and metastable structures solely on chemical composition. USPEX can be utilized with ABACUS for accurate energy and force calculations during evolutionary structure searches.

VII. SUMMARY

In this review, we have detailed the recent advances in the ABACUS package, which is an open-source platform for first-principles electronic structure calculations and molecular dynamics simulations. ABACUS supports both PW and NAO basis sets and is compatible with a range of electronic structure methods.

On one hand, built on a plane wave (PW) basis, ABACUS supports iterative methods with parallel algorithms for diagonalizing the Kohn–Sham equation. In addition, the stochastic DFT method has been implemented, offering an alternative approach to address extremely high-temperature systems with substantially improved computational efficiency. Furthermore, OFDFT has been incorporated, featuring diverse kinetic energy density functionals, including machine learning-based ones, and optimization methods tailored for large-scale materials systems. On the other hand, by using the NAO basis set, ABACUS provides efficient solutions to the Kohn–Sham equation, featuring methods such as hybrid functional, DeePKS, DFT+U, etc. In addition, real-time TDDFT has been implemented. These methods have been benchmarked and applied to various systems, demonstrating their accuracy and effectiveness.

ABACUS has been used to generate a large amount of first-principles data for training machine-learning-based potentials. The APNS project has been initiated to ensure the reliability and accuracy of ABACUS, where systematic tests for pseudopotentials and numerical atomic orbitals have been conducted, providing a solid foundation for the software's performance. ABACUS interacts with several packages, such as DeePKS-kit, DeePMD-kit, DP-GEN, DeepH, DeePTB, HamGNN, PyATB, Hefei-NAMD, PEXSI, etc., further expanding its functionality and applicability in multi-scale calculations and electronic structure analysis.

In conclusion, with the support of AI techniques, ABACUS has emerged as a robust and flexible platform for electronic structure calculations and analysis, well-positioned to address the challenges in materials science, chemistry, and physics within the AI era. Its ongoing development and integration with AI technologies are expected to further enhance its capabilities, strengthening its role as a valuable tool for researchers and scientists in the field.

ACKNOWLEDGMENTS

We thank Han Wang and Weinan E for many helpful discussions. We gratefully acknowledge the support from the AI for Science Institute, Beijing (AISI). M.C. acknowledges the funding support from the National Key R&D Program of China under Grant No. 2025YFB3003603 and the National Natural Science Foundation of China (Grant Nos. 12588201, 12588301, 12135002, 12122401, and 12074007). H.R. is supported by the Beijing Natural Science Foundation (Grant No. QY24014). S.X. gratefully acknowledges the funding support from the National Natural Science Foundation of China (Grant No. 52273223), DP Technology Corporation (Grant No. 2021110016001141), the School of Materials Science and Engineering at Peking University, and the AI for Science Institute, Beijing (AISI). S.L. acknowledges the support from the National Natural Science Foundation of China (Grant No. 92370104) and the Natural Science Foundation of Zhejiang Province (Grant No. 2022XHSJJ006). The computational resource was provided by the

Westlake HPC Center. M.L. gratefully acknowledges the financial support of the National Natural Science Foundation of China (Grant No. 52276212), and the National Key Research and Development Program of China (Grant No. 2022YFB3803600). Q.O. acknowledges the research grants from China Petroleum and Chemical Corp. (Funding No. 124014). T.W. acknowledges the support by The University of Hong Kong (HKU) via seed funds (Grant Nos. 2201100392 and 2409100597). Y.X. acknowledges the support from the National Key Basic Research and Development Program of China (Grant Nos. 2024YFA1409100 and 2023YFA1406400), the National Natural Science Foundation of China (Grants Nos. 12334003, 12421004, and 12361141826), and the National Science Fund for Distinguished Young Scholars (Grant No. 12025405). W.Z. gratefully acknowledges the AI for Science Institute, Beijing (AISI), as well as support from the Hongyi postdoctoral fellowship of Wuhan University.

AUTHOR DECLARATIONS

Conflict of Interest

The authors have no conflicts to disclose.

Author Contributions

Weiqing Zhou: Data curation (lead); Methodology (equal); Software (equal); Validation (lead); Visualization (lead); Writing – original draft (lead); Writing – review & editing (lead). **Daye Zheng**: Data curation (equal); Resources (equal); Software (equal); Writing – original draft (equal). **Qianrui Liu**: Visualization (equal); Writing – original draft (equal). **Denghui Lu**: Writing – original draft (equal). **Yu Liu**: Writing – original draft (equal). **Peize Lin**: Writing – original draft (equal). **Yike Huang**: Visualization (supporting); Writing – original draft (supporting). **Xingliang Peng**: Data curation (equal); Visualization (supporting). **Jie J. Bao**: Writing – review & editing (supporting). **Chun Cai**: Writing – original draft (supporting). **Zuxin Jin**: Writing – review & editing (supporting). **Jing Wu**: Visualization (supporting); Writing – original draft (supporting). **Haochong Zhang**: Writing – original draft (supporting). **Gan Jin**: Writing – original draft (supporting). **Yuyang Ji**: Writing – original draft (supporting). **Zhenxiong Shen**: Writing – original draft (supporting). **Xiaohui Liu**: Writing – original draft (supporting). **Liang Sun**: Writing – original draft (supporting). **Yu Cao**: Writing – original draft (supporting). **Menglin Sun**: Writing – original draft (supporting). **Jianchuan Liu**: Writing – original draft (supporting). **Tao Chen**: Writing – original draft (supporting). **Renxi Liu**: Writing – original draft (supporting). **Yuanbo Li**: Writing – original draft (supporting). **Haozhi Han**: Writing – original draft (supporting). **Xinyuan Liang**: Writing – original draft (supporting). **Taoni Bao**: Writing – original draft (supporting). **Zichao Deng**: Writing – original draft (supporting). **Tao Liu**: Writing – original draft (supporting). **Nuo Chen**: Writing – original draft (supporting). **Hongxu Ren**: Writing – original draft (supporting). **Xiaoyang Zhang**: Writing – original draft (supporting). **Zhaoqing Liu**: Writing – original draft (supporting). **Yiwei Fu**: Writing – original draft (supporting). **Maochang Liu**: Writing – original draft (supporting). **Zhuoyuan Li**: Writing – original draft (supporting). **Tongqi Wen**: Writing – original draft (supporting). **Zechen Tang**: Writing – original draft (supporting). **Yong Xu**: Writing – original draft (supporting). **Wenhui Duan**: Writing – original draft (supporting). **Xiaoyang Wang**: Writing – original draft (supporting). **Qiangqiang Gu**: Writing – original draft (supporting). **Fu-Zhi Dai**: Writing – original draft (supporting). **Qijing Zheng**: Writing – original draft (supporting). **Yang Zhong**: Writing – original draft (supporting). **Hongjun Xiang**: Writing – original draft (supporting). **Xingao Gong**: Writing – original draft (supporting). **Jin Zhao**: Writing – original draft (supporting). **Yuzhi Zhang**: Writing – original draft (supporting). **Qi Ou**: Writing – review & editing (supporting). **Hong Jiang**: Writing – review & editing (supporting). **Shi Liu**: Writing – review & editing (supporting). **Ben Xu**: Writing – review & editing (supporting). **Shenzhen Xu**: Writing – review & editing (supporting). **Xinguo Ren**: Conceptualization (equal); Methodology (lead); Software (lead); Writing – review & editing (equal). **Lixin He**: Conceptualization (equal); Methodology (lead); Software (lead); Writing – review & editing (equal). **Linfeng Zhang**: Conceptualization (equal). **Mohan Chen**: Conceptualization (lead); Investigation (lead); Methodology (lead); Resources (lead); Software (lead); Supervision (lead); Validation (lead); Writing – review & editing (lead).

DATA AVAILABILITY

The data that support the findings of this study are available from the corresponding author upon reasonable request.

REFERENCES

[1] L. H. Thomas, "The calculation of atomic fields," in *Mathematical Proceedings of the Cambridge Philosophical Society* (Cambridge University Press, 1927), Vol. 23, pp. 542–548.
[2] E. Fermi, "Statistical method to determine some properties of atoms," Rend. Accad. Naz. Lincei **6**, 602–607 (1927).
[3] Y. A. Wang and E. A. Carter, *Theoretical Methods in Condensed Phase Chemistry* (Springer, 2002), p. 117.
[4] P. Hohenberg and W. Kohn, "Inhomogeneous electron gas," Phys. Rev. **136**, B864 (1964).
[5] W. Kohn and L. J. Sham, "Self-consistent equations including exchange and correlation effects," Phys. Rev. **140**, A1133 (1965).
[6] P. Blaha, K. Schwarz, F. Tran, R. Laskowski, G. K. Madsen, and L. D. Marks, "WIEN2k: An APW+lo program for calculating the properties of solids," J. Chem. Phys. **152**, 074101 (2020).
[7] Y. Zhang, B. Suo, Z. Wang, N. Zhang, Z. Li, Y. Lei, W. Zou, J. Gao, D. Peng, Z. Pu *et al.*, "BDF: A relativistic electronic structure program package," J. Chem. Phys. **152**, 064113 (2020).
[8] A. H. Romero, D. C. Allan, B. Amadon, G. Antonius, T. Applencourt, L. Baguet, J. Bieder, F. Bottin, J. Bouchet, E. Bousquet *et al.*, "ABINIT: Overview and focus on selected capabilities," J. Chem. Phys. **152**, 124102 (2020).
[9] A. Nakata, J. S. Baker, S. Y. Mujahed, J. T. L. Poulton, S. Arapan, J. Lin, Z. Raza, S. Yadav, L. Truflandier, T. Miyazaki, and D. R. Bowler, "Large scale and linear scaling DFT with the CONQUEST code," J. Chem. Phys. **152**, 164112 (2020).
[10] T. D. Kühne, M. Iannuzzi, M. Del Ben, V. V. Rybkin, P. Seewald, F. Stein, T. Laino, R. Z. Khaliullin, O. Schütt, F. Schiffmann *et al.*, "CP2K: An electronic structure and molecular dynamics software package - Quickstep: Efficient and accurate electronic structure calculations," J. Chem. Phys. **152**, 194103 (2020).
[11] N. Tancogne-Dejean, M. J. T. Oliveira, X. Andrade, H. Appel, C. H. Borca, G. Le Breton, F. Buchholz, A. Castro, S. Corni, A. A. Correa *et al.*, "Octopus, a computational framework for exploring light-driven phenomena and quantum dynamics in extended and finite systems," J. Chem. Phys. **152**, 124119 (2020).

[12]J. C. A. Prentice, J. Aarons, J. C. Womack, A. E. A. Allen, L. Andrinopoulos, L. Anton, R. A. Bell, A. Bhandari, G. A. Bramley, R. J. Charlton *et al.*, "The ONETEP linear-scaling density functional theory program," J. Chem. Phys. **152**, 174111 (2020).
[13]Q. Sun, X. Zhang, S. Banerjee, P. Bao, M. Barbry, N. S. Blunt, N. A. Bogdanov, G. H. Booth, J. Chen, Z.-H. Cui *et al.*, "Recent developments in the PySCF program package," J. Chem. Phys. **153**, 024109 (2020).
[14]P. Giannozzi, O. Baseggio, P. Bonfà, D. Brunato, R. Car, I. Carnimeo, C. Cavazzoni, S. de Gironcoli, P. Delugas, F. Ferrari Ruffino *et al.*, "Quantum ESPRESSO toward the exascale," J. Chem. Phys. **152**, 154105 (2020).
[15]A. García, N. Papior, A. Akhtar, E. Artacho, V. Blum, E. Bosoni, P. Brandimarte, M. Brandbyge, J. I. Cerdá, F. Corsetti *et al.*, "SIESTA: Recent developments and applications," J. Chem. Phys. **152**, 204108 (2020).
[16]G. Kresse and D. Joubert, "From ultrasoft pseudopotentials to the projector augmented-wave method," Phys. Rev. B **59**, 1758 (1999).
[17]M. J. Frisch, G. W. Trucks, H. B. Schlegel, G. E. Scuseria, M. A. Robb, J. R. Cheeseman, G. Scalmani, V. Barone, G. A. Petersson, H. Nakatsuji, X. Li, M. Caricato, A. V. Marenich, J. Bloino, B. G. Janesko, R. Gomperts, B. Mennucci, H. P. Hratchian, J. V. Ortiz, A. F. Izmaylov, J. L. Sonnenberg, D. Williams-Young, F. Ding, F. Lipparini, F. Egidi, J. Goings, B. Peng, A. Petrone, T. Henderson, D. Ranasinghe, V. G. Zakrzewski, J. Gao, N. Rega, G. Zheng, W. Liang, M. Hada, M. Ehara, K. Toyota, R. Fukuda, J. Hasegawa, M. Ishida, T. Nakajima, Y. Honda, O. Kitao, H. Nakai, T. Vreven, K. Throssell, J. A. Montgomery, Jr., J. E. Peralta, F. Ogliaro, M. J. Bearpark, J. J. Heyd, E. N. Brothers, K. N. Kudin, V. N. Staroverov, T. A. Keith, R. Kobayashi, J. Normand, K. Raghavachari, A. P. Rendell, J. C. Burant, S. S. Iyengar, J. Tomasi, M. Cossi, J. M. Millam, M. Klene, C. Adamo, R. Cammi, J. W. Ochterski, R. L. Martin, K. Morokuma, O. Farkas, J. B. Foresman, and D. J. Fox, Gaussian 16, Revision C.01, Gaussian, Inc., Wallingford, CT, 2016.
[18]M. Chen, G.-C. Guo, and L. He, "Systematically improvable optimized atomic basis sets for *ab initio* calculations," J. Phys.: Condens. Matter **22**, 445501 (2010).
[19]M. Chen, G.-C. Guo, and L. He, "Electronic structure interpolation via atomic orbitals," J. Phys.: Condens. Matter **23**, 325501 (2011).
[20]P. Li, X. Liu, M. Chen, P. Lin, X. Ren, L. Lin, C. Yang, and L. He, "Large-scale *ab initio* simulations based on systematically improvable atomic basis," Comput. Mater. Sci. **112**, 503–517 (2016).
[21]P. Lin, X. Ren, and L. He, "Accuracy of localized resolution of the identity in periodic hybrid functional calculations with numerical atomic orbitals," J. Phys. Chem. Lett. **11**, 3082–3088 (2020).
[22]D. Zheng, X. Ren, and L. He, "Accurate stress calculations based on numerical atomic orbital bases: Implementation and benchmarks," Comput. Phys. Commun. **267**, 108043 (2021).
[23]P. Lin, X. Ren, and L. He, "Efficient hybrid density functional calculations for large periodic systems using numerical atomic orbitals," J. Chem. Theory Comput. **17**, 222–239 (2021).
[24]P. Lin, X. Ren, and L. He, "Strategy for constructing compact numerical atomic orbital basis sets by incorporating the gradients of reference wavefunctions," Phys. Rev. B **103**, 235131 (2021).
[25]X. Qu, P. Xu, H. Jiang, L. He, and X. Ren, "DFT+U within the framework of linear combination of numerical atomic orbitals," J. Chem. Phys. **156**, 234104 (2022).
[26]X. Qu, P. Xu, R. Li, G. Li, L. He, and X. Ren, "Density functional theory plus dynamical mean field theory within the framework of linear combination of numerical atomic orbitals: Formulation and benchmarks," J. Chem. Theory Comput. **18**, 5589–5606 (2022).
[27]Q. Liu and M. Chen, "Plane-wave-based stochastic-deterministic density functional theory for extended systems," Phys. Rev. B **106**, 125132 (2022).
[28]Z. Dai, G. Jin, and L. He, "First-principles calculations of the surface states of doped and alloyed topological materials via band unfolding method," Comput. Mater. Sci. **213**, 111656 (2022).
[29]R. Liu, D. Zheng, X. Liang, X. Ren, M. Chen, and W. Li, "Implementation of the meta-GGA exchange-correlation functional in numerical atomic orbital basis: With systematic testing on SCAN, rSCAN, and r^{2}SCAN functionals," J. Chem. Phys. **159**, 074109 (2023).
[30]P. Lin, X. Ren, X. Liu, and L. He, "Ab initio electronic structure calculations based on numerical atomic orbitals: Basic fomalisms and recent progresses," Wiley Interdiscip. Rev.: Comput. Mol. Sci. **14**, e1687 (2024).
[31]L. Zhang, J. Han, H. Wang, R. Car, and W. E, "Deep potential molecular dynamics: A scalable model with the accuracy of quantum mechanics," Phys. Rev. Lett. **120**, 143001 (2018).
[32]H. Wang, L. Zhang, J. Han, and W. E, "DeePMD-kit: A deep learning package for many-body potential energy representation and molecular dynamics," Comput. Phys. Commun. **228**, 178–184 (2018).
[33]Y. Chen, L. Zhang, H. Wang, and W. E, "DeePKS: A comprehensive data-driven approach toward chemically accurate density functional theory," J. Chem. Theory Comput. **17**, 170–181 (2021).
[34]Y. Chen, L. Zhang, H. Wang, and W. E, "DeePKS-kit: A package for developing machine learning-based chemically accurate energy and density functional models," Comput. Phys. Commun. **282**, 108520 (2022).
[35]J. Kirkpatrick, B. McMorrow, D. H. P. Turban, A. L. Gaunt, J. S. Spencer, A. G. D. G. Matthews, A. Obika, L. Thiry, M. Fortunato, D. Pfau *et al.*, "Pushing the frontiers of density functionals by solving the fractional electron problem," Science **374**, 1385–1389 (2021).
[36]W. Jia, H. Wang, M. Chen, D. Lu, L. Lin, R. Car, E. Weinan, and L. Zhang, "Pushing the limit of molecular dynamics with *ab initio* accuracy to 100 million atoms with machine learning," in *SC20: International Conference for High Performance Computing, Networking, Storage and Analysis* (IEEE, 2020), pp. 1–14.
[37]J. Han, L. Zhang, and E. Weinan, "Solving many-electron Schrödinger equation using deep neural networks," J. Comput. Phys. **399**, 108929 (2019).
[38]Y. Chen, L. Zhang, H. Wang, and W. E, "Ground state energy functional with Hartree–Fock efficiency and chemical accuracy," J. Phys. Chem. A **124**, 7155–7165 (2020).
[39]T. Wen, L. Zhang, H. Wang, W. E, and D. J. Srolovitz, "Deep potentials for materials science," Mater. Futures **1**, 022601 (2022).
[40]https://github.com/deepmodeling/abacus-develop, 2024.
[41]https://www.aissquare.com/openlam, 2024.
[42]S. Boker, M. Neale, H. Maes, M. Wilde, M. Spiegel, T. Brick, J. Spies, R. Estabrook, S. Kenny, T. Bates *et al.*, "OpenMx: An open source extended structural equation modeling framework," Psychometrika **76**, 306–317 (2011).
[43]V. Blum, R. Gehrke, F. Hanke, P. Havu, V. Havu, X. Ren, K. Reuter, and M. Scheffler, "*Ab initio* molecular simulations with numeric atom-centered orbitals," Comput. Phys. Commun. **180**, 2175–2196 (2009).
[44]J. R. Chelikowsky, N. Troullier, and Y. Saad, "Finite-difference-pseudopotential method: Electronic structure calculations without a basis," Phys. Rev. Lett. **72**, 1240–1243 (1994).
[45]L. E. Ratcliff, W. Dawson, G. Fisicaro, D. Caliste, S. Mohr, A. Degomme, B. Videau, V. Cristiglio, M. Stella, M. D'Alessandro *et al.*, "Flexibilities of wavelets as a computational basis set for large-scale electronic structure calculations," J. Chem. Phys. **152**, 194110 (2020).
[46]L. Kleinman, "Relativistic norm-conserving pseudopotential," Phys. Rev. B **21**, 2630 (1980).
[47]G. B. Bachelet and M. Schlüter, "Relativistic norm-conserving pseudopotentials," Phys. Rev. B **25**, 2103 (1982).
[48]A. M. Rappe, K. M. Rabe, E. Kaxiras, and J. D. Joannopoulos, "Optimized pseudopotentials," Phys. Rev. B **41**, 1227–1230 (1990).
[49]D. Vanderbilt, "Soft self-consistent pseudopotentials in a generalized eigenvalue formalism," Phys. Rev. B **41**, 7892–7895 (1990).
[50]N. Troullier and J. L. Martins, "Efficient pseudopotentials for plane-wave calculations," Phys. Rev. B **43**, 1993–2006 (1991).
[51]G. Kresse and J. Hafner, "Norm-conserving and ultrasoft pseudopotentials for first-row and transition elements," J. Phys.: Condens. Matter **6**, 8245 (1994).
[52]D. R. Hamann, "Optimized norm-conserving Vanderbilt pseudopotentials," Phys. Rev. B **88**, 085117 (2013).
[53]D. R. Hamann, M. Schlüter, and C. Chiang, "Norm-conserving pseudopotentials," Phys. Rev. Lett. **43**, 1494–1497 (1979).
[54]L. Kleinman and D. M. Bylander, "Efficacious form for model pseudopotentials," Phys. Rev. Lett. **48**, 1425 (1982).
[55]S. G. Louie, S. Froyen, and M. L. Cohen, "Nonlinear ionic pseudopotentials in spin-density-functional calculations," Phys. Rev. B **26**, 1738–1742 (1982).
[56]G. Theurich and N. A. Hill, "Self-consistent treatment of spin-orbit coupling in solids using relativistic fully separable *ab initio* pseudopotentials," Phys. Rev. B **64**, 073106 (2001).

[57]A. D. Corso and A. M. Conte, "Spin-orbit coupling with ultrasoft pseudopotentials: Application to Au and Pt," Phys. Rev. B **71**, 115106 (2005).
[58]R. Cuadrado, R. Robles, A. García, M. Pruneda, P. Ordejón, J. Ferrer, and J. I. Cerdá, "Validity of the on-site spin-orbit coupling approximation," Phys. Rev. B **104**, 195104 (2021).
[59]U. Von Barth and L. Hedin, "A local exchange-correlation potential for the spin polarized case. I," J. Phys. C: Solid State Phys. **5**, 1629 (1972).
[60]S. H. Vosko, L. Wilk, and M. Nusair, "Accurate spin-dependent electron liquid correlation energies for local spin density calculations: A critical analysis," Can. J. Phys. **58**, 1200–1211 (1980).
[61]J. P. Perdew, K. Burke, and M. Ernzerhof, "Generalized gradient approximation made simple," Phys. Rev. Lett. **77**, 3865 (1996).
[62]J. Sun, A. Ruzsinszky, and J. P. Perdew, "Strongly constrained and appropriately normed semilocal density functional," Phys. Rev. Lett. **115**, 036402 (2015).
[63]A. P. Bartók and J. R. Yates, "Regularized SCAN functional," J. Chem. Phys. **150**, 161101 (2019).
[64]J. W. Furness, A. D. Kaplan, J. Ning, J. P. Perdew, and J. Sun, "Accurate and numerically efficient r^2SCAN meta-generalized gradient approximation," J. Phys. Chem. Lett. **11**, 8208–8215 (2020).
[65]J. Heyd, G. E. Scuseria, and M. Ernzerhof, "Hybrid functionals based on a screened Coulomb potential," J. Chem. Phys. **118**, 8207–8215 (2003).
[66]H. J. S. Ge and M. Ernzerhof, "Erratum: "Hybrid functionals based on a screened Coulomb potential" [J. Chem. Phys. 118, 8207 (2003)]," J. Chem. Phys. **124**, 219906 (2006).
[67]C. Adamo and V. Barone, "Toward reliable density functional methods without adjustable parameters: The PBE0 model," J. Chem. Phys. **110**, 6158–6170 (1999).
[68]P. J. Stephens, F. J. Devlin, C. F. Chabalowski, and M. J. Frisch, "Ab initio calculation of vibrational absorption and circular dichroism spectra using density functional force fields," J. Phys. Chem. **98**, 11623–11627 (1994).
[69]B. Miehlich, A. Savin, H. Stoll, and H. Preuss, "Results obtained with the correlation energy density functionals of Becke and Lee, Yang and Parr," Chem. Phys. Lett. **157**, 200–206 (1989).
[70]https://libxc.gitlab.io/, 2024.
[71]P. Pulay, "Convergence acceleration of iterative sequences. The case of SCF iteration," Chem. Phys. Lett. **73**, 393–398 (1980).
[72]P. Pulay, "Improved SCF convergence acceleration," J. Comput. Chem. **3**, 556–560 (1982).
[73]D. D. Johnson, "Modified Broyden's method for accelerating convergence in self-consistent calculations," Phys. Rev. B **38**, 12807–12813 (1988).
[74]L. Lin, J. Lu, L. Ying, R. Car, and W. E, "Fast algorithm for extracting the diagonal of the inverse matrix with application to the electronic structure analysis of metallic systems," Commun. Math. Sci. **7**, 755 (2009).
[75]L. Lin, M. Chen, C. Yang, and L. He, "Accelerating atomic orbital-based electronic structure calculation via pole expansion and selected inversion," J. Phys.: Condens. Matter **25**, 295501 (2013).
[76]Y. Zhou, H. Wang, Y. Liu, X. Gao, and H. Song, "Applicability of Kerker preconditioning scheme to the self-consistent density functional theory calculations of inhomogeneous systems," Phys. Rev. E **97**, 033305 (2018).
[77]https://github.com/deepmodeling/abacus-develop/pull/3226, 2024.
[78]M. A. Halcrow, "Jahn–Teller distortions in transition metal compounds, and their importance in functional molecular and inorganic materials," Chem. Soc. Rev. **42**, 1784–1795 (2013).
[79]M. Heide and T. Ono, "Convergence of the broyden density mixing method in noncollinear magnetic systems," J. Phys. Soc. Jpn. **82**, 114706 (2013).
[80]M. Cococcioni and S. de Gironcoli, "Linear response approach to the calculation of the effective interaction parameters in the LDA+U method," Phys. Rev. B **71**, 035105 (2005).
[81]V. I. Anisimov, I. V. Solovyev, M. A. Korotin, M. T. Czyżyk, and G. A. Sawatzky, "Density-functional theory and NiO photoemission spectra," Phys. Rev. B **48**, 16929 (1993).
[82]V. I. Anisimov, F. Aryasetiawan, and A. I. Lichtenstein, "First-principles calculations of the electronic structure and spectra of strongly correlated systems: The **LDA** + *U* method," J. Phys.: Condens. Matter **9**, 767 (1997).
[83]S. L. Dudarev, G. A. Botton, S. Y. Savrasov, C. J. Humphreys, and A. P. Sutton, "Electron-energy-loss spectra and the structural stability of nickel oxide: An LSDA+U study," Phys. Rev. B **57**, 1505 (1998).
[84]H. Jiang, R. I. Gomez-Abal, P. Rinke, and M. Scheffler, "First-principles modeling of localized d states with the GW@LDA+U approach," Phys. Rev. B **82**, 045108 (2010).
[85]B. Meredig, A. Thompson, H. A. Hansen, C. Wolverton, and A. van de Walle, "Method for locating low-energy solutions within DFT+U," Phys. Rev. B **82**, 195128 (2010).
[86]B. Dorado, M. Freyss, B. Amadon, M. Bertolus, G. Jomard, and P. Garcia, "Advances in first-principles modelling of point defects in UO_2: f electron correlations and the issue of local energy minima," J. Phys.: Condens. Matter **25**, 333201 (2013).
[87]N. D. Mermin, "Thermal properties of the inhomogeneous electron gas," Phys. Rev. **137**, A1441–A1443 (1965).
[88]M. Methfessel and A. T. Paxton, "High-precision sampling for Brillouin-zone integration in metals," Phys. Rev. B **40**, 3616–3621 (1989).
[89]N. Marzari, D. Vanderbilt, A. De Vita, and M. C. Payne, "Thermal contraction and disordering of the Al(110) surface," Phys. Rev. Lett. **82**, 3296–3299 (1999).
[90]J. D. Head and M. C. Zerner, "A Broyden—Fletcher—Goldfarb—Shanno optimization procedure for molecular geometries," Chem. Phys. Lett. **122**, 264–270 (1985).
[91]E. Bitzek, P. Koskinen, F. Gähler, M. Moseler, and P. Gumbsch, "Structural relaxation made simple," Phys. Rev. Lett. **97**, 170201 (2006).
[92]Y. Liu, Y. Zhang, N. Xiao, X. Li, F.-Z. Dai, and M. Chen, "Investigating interfacial segregation of Ω/Al in Al–Cu alloys: A comprehensive study using density functional theory and machine learning," Acta Mater. **279**, 120294 (2024).
[93]Y. Liu, X. Liu, and M. Chen, "Copper-doped beryllium and beryllium oxide interface: A first-principles study," J. Nucl. Mater. **545**, 152733 (2021).
[94]Y. Liu, X. Ding, M. Chen, and S. Xu, "A caveat of the charge-extrapolation scheme for modeling electrochemical reactions on semiconductor surfaces: An issue induced by a discontinuous Fermi level change," Phys. Chem. Chem. Phys. **24**, 15511–15521 (2022).
[95]D. Chen, Y. Liu, Y. Zheng, H. Zhuang, M. Chen, and Y. Jiao, "Disordered hyperuniform quasi-one-dimensional materials," Phys. Rev. B **106**, 235427 (2022).
[96]Y. Liu and M. Chen, "Multihyperuniformity in high-entropy MXenes," Appl. Phys. Lett. **126**, 013101 (2025).
[97]J. Zeng, D. Zhang, D. Lu, P. Mo, Z. Li, Y. Chen, M. Rynik, L. Huang, Z. Li, S. Shi, Y. Wang, H. Ye, P. Tuo, J. Yang, Y. Ding, Y. Li, D. Tisi, Q. Zeng, H. Bao, Y. Xia, J. Huang, K. Muraoka, Y. Wang, J. Chang, F. Yuan, S. L. Bore, C. Cai, Y. Lin, B. Wang, J. Xu, J.-X. Zhu, C. Luo, Y. Zhang, R. E. A. Goodall, W. Liang, A. K. Singh, S. Yao, J. Zhang, R. Wentzcovitch, J. Han, J. Liu, W. Jia, D. M. York, W. E, R. Car, L. Zhang, and H. Wang, "DeePMD-kit v2: A software package for deep potential models," J. Chem. Phys. **159**, 054801 (2023).
[98]J. E. Jones and S. Chapman, "On the determination of molecular fields.—I. From the variation of the viscosity of a gas with temperature," Proc. R. Soc. London, Ser. A **106**, 441–462 (1924).
[99]J. E. Jones and S. Chapman, "On the determination of molecular fields.—II. From the equation of state of a gas," Proc. R. Soc. London, Ser. A **106**, 463–477 (1924).
[100]W. C. Swope, H. C. Andersen, P. H. Berens, and K. R. Wilson, "A computer simulation method for the calculation of equilibrium constants for the formation of physical clusters of molecules: Application to small water clusters," J. Chem. Phys. **76**, 637–649 (1982).
[101]G. J. Martyna, M. E. Tuckerman, D. J. Tobias, and M. L. Klein, "Explicit reversible integrators for extended systems dynamics," Mol. Phys. **87**, 1117–1157 (1996).
[102]S. Nosé, "A unified formulation of the constant temperature molecular dynamics methods," J. Chem. Phys. **81**, 511–519 (1984).
[103]W. G. Hoover, "Canonical dynamics: Equilibrium phase-space distributions," Phys. Rev. A **31**, 1695–1697 (1985).
[104]G. J. Martyna, M. L. Klein, and M. Tuckerman, "Nosé–Hoover chains: The canonical ensemble via continuous dynamics," J. Chem. Phys. **97**, 2635–2643 (1992).
[105]H. C. Andersen, "Molecular dynamics simulations at constant pressure and/or temperature," J. Chem. Phys. **72**, 2384–2393 (1980).

[106]H. J. C. Berendsen, J. P. M. Postma, W. F. van Gunsteren, A. DiNola, and J. R. Haak, "Molecular dynamics with coupling to an external bath," J. Chem. Phys. **81**, 3684–3690 (1984).
[107]T. Schneider and E. Stoll, "Molecular-dynamics study of a three-dimensional one-component model for distortive phase transitions," Phys. Rev. B **17**, 1302–1322 (1978).
[108]E. J. Reed, L. E. Fried, and J. D. Joannopoulos, "A method for tractable dynamical studies of single and double shock compression," Phys. Rev. Lett. **90**, 235503 (2003).
[109]T. Chen, Q. Liu, Y. Liu, L. Sun, and M. Chen, "Combining stochastic density functional theory with deep potential molecular dynamics to study warm dense matter," Matter Radiat. Extremes **9**, 015604 (2024).
[110]X. Liu, D. Zheng, X. Ren, L. He, and M. Chen, "First-principles molecular dynamics study of deuterium diffusion in liquid tin," J. Chem. Phys. **147**, 064505 (2017).
[111]Q. Wang, D. Zheng, L. He, and X. Ren, "Cooperative effect in a graphite intercalation compound: Enhanced mobility of Al Cl_4 in the graphite cathode of aluminum-ion batteries," Phys. Rev. Appl. **12**, 044060 (2019).
[112]X. Liu, Y. Qi, D. Zheng, C. Zhou, L. He, and F. Huang, "Diffusion coefficients of Mg isotopes in $MgSiO_3$ and Mg_2SiO_4 melts calculated by first-principles molecular dynamics simulations," Geochim. Cosmochim. Acta **223**, 364–376 (2018).
[113]Q. Wang, D. Zheng, L. He, and X. Ren, "Peculiar diffusion behavior of $AlCl_4$ intercalated in graphite from nanosecond-long molecular dynamics simulations," Chin. Phys. B **30**, 107102 (2021).
[114]D. Zheng, Z.-X. Shen, M. Chen, X. Ren, and L. He, "Retention and recycling of deuterium in liquid lithium-tin slab studied by first-principles molecular dynamics," J. Nucl. Mater. **543**, 152542 (2021).
[115]S. Zhang, H. Wang, W. Kang, P. Zhang, and X. T. He, "Extended application of Kohn-Sham first-principles molecular dynamics method with plane wave approximation at high energy—From cold materials to hot dense plasmas," Phys. Plasmas **23**, 042707 (2016).
[116]A. Blanchet, J. Clérouin, M. Torrent, and F. Soubiran, "Extended first-principles molecular dynamics model for high temperature simulations in the ABINIT code: Application to warm dense aluminum," Comput. Phys. Commun. **271**, 108215 (2022).
[117]A. Blanchet, F. Soubiran, M. Torrent, and J. Clérouin, "Extended first-principles molecular dynamics simulations of hot dense boron: Equation of state and ionization," Contrib. Plasma Phys. **62**, e202100234 (2022).
[118]V. V. Karasiev, J. W. Dufty, and S. Trickey, "Nonempirical semilocal free-energy density functional for matter under extreme conditions," Phys. Rev. Lett. **120**, 076401 (2018).
[119]Y. Zhang, C. Gao, Q. Liu, L. Zhang, H. Wang, and M. Chen, "Warm dense matter simulation via electron temperature dependent deep potential molecular dynamics," Phys. Plasmas **27**, 122704 (2020).
[120]C. Ma, M. Chen, Y. Xie, Q. Xu, W. Mi, Y. Wang, and Y. Ma, "Nonlocal free-energy density functional for a broad range of warm dense matter simulations," Phys. Rev. B **110**, 085113 (2024).
[121]W. Mi, X. Shao, C. Su, Y. Zhou, S. Zhang, Q. Li, H. Wang, L. Zhang, M. Miao, Y. Wang, and Y. Ma, "ATLAS: A real-space finite-difference implementation of orbital-free density functional theory," Comput. Phys. Commun. **200**, 87–95 (2016).
[122]K. Mathew, R. Sundararaman, K. Letchworth-Weaver, T. A. Arias, and R. G. Hennig, "Implicit solvation model for density-functional study of nanocrystal surfaces and reaction pathways," J. Chem. Phys. **140**, 084106 (2014).
[123]S. A. Petrosyan, A. A. Rigos, and T. A. Arias, "Joint density-functional theory: Ab initio study of Cr_2O_3 surface chemistry in solution," J. Phys. Chem. B **109**, 15436–15444 (2005).
[124]K. Mathew, V. S. C. Kolluru, S. Mula, S. N. Steinmann, and R. G. Hennig, "Implicit self-consistent electrolyte model in plane-wave density-functional theory," J. Chem. Phys. **151**, 234101 (2019).
[125]M. Sun, B. Jin, X. Yang, and S. Xu, "Probing nuclear quantum effects in electrocatalysis via a machine-learning enhanced grand canonical constant potential approach," Nat. Commun. **16**, 3600 (2025).
[126]L. Bengtsson, "Dipole correction for surface supercell calculations," Phys. Rev. B **59**, 12301–12304 (1999).
[127]T. Brumme, M. Calandra, and F. Mauri, "Electrochemical doping of few-layer ZrNCl from first principles: Electronic and structural properties in field-effect configuration," Phys. Rev. B **89**, 245406 (2014).
[128]H. J. Monkhorst and J. D. Pack, "Special points for Brillouin-zone integrations," Phys. Rev. B **13**, 5188–5192 (1976).
[129]R. M. Martin, *Electronic Structure: Basic Theory and Practical Methods* (Cambridge University Press, 2020).
[130]H. Hellmann, "A combined approximation method for the energy calculation in the many-electron problem," Acta Physicochim. URSS **1**, 913 (1935); **4**, 225 (1936); **4**, 324 (1936); J. Chem. Phys. **3**, 61 (1935).
[131]R. P. Feynman, "Forces in molecules," Phys. Rev. **56**, 340–343 (1939).
[132]E. Polak, *Computational Methods in Optimization: A Unified Approach* (Academic Press, 1971), Vol. 77.
[133]M. P. Teter, M. C. Payne, and D. C. Allan, "Solution of Schrödinger's equation for large systems," Phys. Rev. B **40**, 12255 (1989).
[134]W. Jia, J. Fu, Z. Cao, L. Wang, X. Chi, W. Gao, and L.-W. Wang, "Fast plane wave density functional theory molecular dynamics calculations on multi-GPU machines," J. Comput. Phys. **251**, 102–115 (2013).
[135]S. Maintz and M. Wetzstein, "Strategies to accelerate VASP with GPUs using openACC," in Proceedings of the Cray User Group, 2018.
[136]F. Gygi, E. W. Draeger, M. Schulz, B. R. De Supinski, J. A. Gunnels, V. Austel, J. C. Sexton, F. Franchetti, S. Kral, C. W. Ueberhuber *et al.*, "Large-scale electronic structure calculations of high-Z metals on the BlueGene/L platform," in *Proceedings of the 2006 ACM/IEEE Conference on Supercomputing* (ACM, 2006), pp. 45–es.
[137]O. Watanabe, A. Musa, H. Hokari, S. Singh, R. Mathur, and H. Kobayashi, "Performance evaluation of Quantum ESPRESSO on NEC SX-ACE," in *2017 IEEE International Conference on Cluster Computing (CLUSTER)* (IEEE, 2017), pp. 701–708.
[138]P. Lucignano, D. Alfè, V. Cataudella, D. Ninno, and G. Cantele, "Crucial role of atomic corrugation on the flat bands and energy gaps of twisted bilayer graphene at the magic angle $\theta \sim 1.08°$," Phys. Rev. B **99**, 195419 (2019).
[139]X. Gonze, B. Amadon, G. Antonius, F. Arnardi, L. Baguet, J.-M. Beuken, J. Bieder, F. Bottin, J. Bouchet, E. Bousquet *et al.*, "The ABINIT project: Impact, environment and recent developments," Comput. Phys. Commun. **248**, 107042 (2020).
[140]J. Feng, L. Wan, J. Li, S. Jiao, X. Cui, W. Hu, and J. Yang, "Massively parallel implementation of iterative eigensolvers in large-scale plane-wave density functional theory," Comput. Phys. Commun. **299**, 109135 (2024).
[141]https://bohrium.dp.tech/en-US, 2024.
[142]https://deepmodeling-activity.github.io/abacus-test.github.io/index.html?pname=bda, 2024.
[143]R. Baer, D. Neuhauser, and E. Rabani, "Self-averaging stochastic Kohn-Sham density-functional theory," Phys. Rev. Lett. **111**, 106402 (2013).
[144]Y. Cytter, E. Rabani, D. Neuhauser, and R. Baer, "Stochastic density functional theory at finite temperatures," Phys. Rev. B **97**, 115207 (2018).
[145]D. Neuhauser, R. Baer, and E. Rabani, "Communication: Embedded fragment stochastic density functional theory," J. Chem. Phys. **141**, 041102 (2014).
[146]E. Arnon, E. Rabani, D. Neuhauser, and R. Baer, "Equilibrium configurations of large nanostructures using the embedded saturated-fragments stochastic density functional theory," J. Chem. Phys. **146**, 224111 (2017).
[147]M. Chen, R. Baer, D. Neuhauser, and E. Rabani, "Overlapped embedded fragment stochastic density functional theory for covalently-bonded materials," J. Chem. Phys. **150**, 034106 (2019).
[148]W. Li, M. Chen, E. Rabani, R. Baer, and D. Neuhauser, "Stochastic embedding DFT: Theory and application to *p*-nitroaniline in water," J. Chem. Phys. **151**, 174115 (2019).
[149]M. Chen, R. Baer, D. Neuhauser, and E. Rabani, "Energy window stochastic density functional theory," J. Chem. Phys. **151**, 114116 (2019).
[150]A. J. White and L. A. Collins, "Fast and universal Kohn-Sham density functional theory algorithm for warm dense matter to hot dense plasma," Phys. Rev. Lett. **125**, 055002 (2020).

[151]M. F. Hutchinson, "A stochastic estimator of the trace of the influence matrix for laplacian smoothing splines," Commun. Stat. - Simul. Comput. **18**, 1059–1076 (1989).
[152]W. Zhou and S. Yuan, "A time-dependent random state approach for large-scale density functional calculations," Chin. Phys. Lett. **40**, 027101 (2023).
[153]R. Baer, D. Neuhauser, and E. Rabani, "Stochastic vector techniques in ground-state electronic structure," Annu. Rev. Phys. Chem. **73**, 255 (2022).
[154]T. Chen, Q. Liu, C. Gao, and M. Chen, "First-principles prediction of shock Hugoniot curves of boron, aluminum, and silicon from stochastic density functional theory," Matter Radiat. Extremes **10**, 057601 (2025).
[155]V. V. Karasiev and S. B. Trickey, "Issues and challenges in orbital-free density functional calculations," Comput. Phys. Commun. **183**, 2519–2527 (2012).
[156]H. Jiang and W. Yang, "Conjugate-gradient optimization method for orbital-free density functional calculations," J. Chem. Phys. **121**, 2030–2036 (2004).
[157]J. Nocedal, "Updating quasi-Newton matrices with limited storage," Math. Comput. **35**, 773–782 (1980).
[158]W. W. Hager and H. Zhang, "A new conjugate gradient method with guaranteed descent and an efficient line search," SIAM J. Optim. **16**, 170–192 (2005).
[159]J. C. Gilbert and J. Nocedal, "Global convergence properties of conjugate gradient methods for optimization," SIAM J. Optim. **2**, 21–42 (1992).
[160]C. F. v. Weizsäcker, "Zur theorie der kernmassen," Z. Phys. **96**, 431–458 (1935).
[161]A. Berk, "Lower-bound energy functionals and their application to diatomic systems," Phys. Rev. A **28**, 1908 (1983).
[162]L.-W. Wang and M. P. Teter, "Kinetic-energy functional of the electron density," Phys. Rev. B **45**, 13196 (1992).
[163]K. Luo, V. V. Karasiev, and S. B. Trickey, "A simple generalized gradient approximation for the noninteracting kinetic energy density functional," Phys. Rev. B **98**, 041111 (2018).
[164]Q. Xu, C. Ma, W. Mi, Y. Wang, and Y. Ma, "Nonlocal pseudopotential energy density functional for orbital-free density functional theory," Nat. Commun. **13**, 1385 (2022).
[165]C. Huang and E. A. Carter, "Transferable local pseudopotentials for magnesium, aluminum and silicon," Phys. Chem. Chem. Phys. **10**, 7109–7120 (2008).
[166]Y.-C. Chi and C. Huang, "High-quality local pseudopotentials for metals," J. Chem. Theory Comput. **20**, 3231–3241 (2024).
[167]W. C. Witt, B. G. del Rio, J. M. Dieterich, and E. A. Carter, "Orbital-free density functional theory for materials research," J. Mater. Res. **33**, 777–795 (2018).
[168]L. A. Constantin, E. Fabiano, and F. Della Sala, "Semilocal Pauli–Gaussian kinetic functionals for orbital-free density functional theory calculations of solids," J. Phys. Chem. Lett. **9**, 4385–4390 (2018).
[169]D. Kang, K. Luo, K. Runge, and S. B. Trickey, "Two-temperature warm dense hydrogen as a test of quantum protons driven by orbital-free density functional theory electronic forces," Matter Radiat. Extremes **5**, 064403 (2020).
[170]Y. A. Wang, N. Govind, and E. A. Carter, "Orbital-free kinetic-energy density functionals with a density-dependent kernel," Phys. Rev. B **60**, 16350 (1999).
[171]C. Huang and E. A. Carter, "Nonlocal orbital-free kinetic energy density functional for semiconductors," Phys. Rev. B **81**, 045206 (2010).
[172]W. Mi, A. Genova, and M. Pavanello, "Nonlocal kinetic energy functionals by functional integration," J. Chem. Phys. **148**, 184107 (2018).
[173]X. Shao, W. Mi, and M. Pavanello, "Revised Huang-Carter nonlocal kinetic energy functional for semiconductors and their surfaces," Phys. Rev. B **104**, 045118 (2021).
[174]L. Sun, Y. Li, and M. Chen, "Truncated nonlocal kinetic energy density functionals for simple metals and silicon," Phys. Rev. B **108**, 075158 (2023).
[175]A. Bhattacharjee, S. Jana, and P. Samal, "First step toward a parameter-free, nonlocal kinetic energy density functional for semiconductors and simple metals," J. Chem. Phys. **160**, 224110 (2024).
[176]M. Levy and H. Ou-Yang, "Exact properties of the Pauli potential for the square root of the electron density and the kinetic energy functional," Phys. Rev. A **38**, 625 (1988).
[177]J. C. Snyder, M. Rupp, K. Hansen, K.-R. Müller, and K. Burke, "Finding density functionals with machine learning," Phys. Rev. Lett. **108**, 253002 (2012).
[178]J. Seino, R. Kageyama, M. Fujinami, Y. Ikabata, and H. Nakai, "Semi-local machine-learned kinetic energy density functional with third-order gradients of electron density," J. Chem. Phys. **148**, 241705 (2018).
[179]R. Meyer, M. Weichselbaum, and A. W. Hauser, "Machine learning approaches toward orbital-free density functional theory: Simultaneous training on the kinetic energy density functional and its functional derivative," J. Chem. Theory Comput. **16**, 5685–5694 (2020).
[180]F. Imoto, M. Imada, and A. Oshiyama, "Order-*N* orbital-free density-functional calculations with machine learning of functional derivatives for semiconductors and metals," Phys. Rev. Res. **3**, 033198 (2021).
[181]K. Ryczko, S. J. Wetzel, R. G. Melko, and I. Tamblyn, "Toward orbital-free density functional theory with small data sets and deep learning," J. Chem. Theory Comput. **18**, 1122–1128 (2022).
[182]H. Zhang, S. Liu, J. You, C. Liu, S. Zheng, Z. Lu, T. Wang, N. Zheng, and B. Shao, "Overcoming the barrier of orbital-free density functional theory for molecular systems using deep learning," Nat. Comput. Sci. **4**, 210–223 (2024).
[183]L. Sun and M. Chen, "Machine learning based nonlocal kinetic energy density functional for simple metals and alloys," Phys. Rev. B **109**(11), 115135 (2024).
[184]K. M. Carling and E. A. Carter, "Orbital-free density functional theory calculations of the properties of Al, Mg and Al–Mg crystalline phases," Modell. Simul. Mater. Sci. Eng. **11**, 339 (2003).
[185]A. Jain, S. P. Ong, G. Hautier, W. Chen, W. D. Richards, S. Dacek, S. Cholia, D. Gunter, D. Skinner, G. Ceder, and K. A. Persson, "Commentary: The materials project: A materials genome approach to accelerating materials innovation," APL Mater. **1**, 011002 (2013).
[186]L. Sun and M. Chen, "Multi-channel machine learning based nonlocal kinetic energy density functional for semiconductors," Electron. Struct. **6**, 045006 (2024).
[187]J. D. Talman, "Numerical Fourier and Bessel transforms in logarithmic variables," J. Comput. Phys. **29**, 35–48 (1978).
[188]O. A. Sharafeddin, H. Ferrel Bowen, D. J. Kouri, and D. K. Hoffman, "Numerical evaluation of spherical Bessel transforms via fast Fourier transforms," J. Comput. Phys. **100**, 294–296 (1992).
[189]M. Toyoda and T. Ozaki, "Fast spherical Bessel transform via fast Fourier transform and recurrence formula," Comput. Phys. Commun. **181**, 277–282 (2010).
[190]A. Cerioni, L. Genovese, A. Mirone, and V. A. Sole, "Efficient and accurate solver of the three-dimensional screened and unscreened Poisson's equation with generic boundary conditions," J. Chem. Phys. **137**, 134108 (2012).
[191]J. M. Soler, E. Artacho, J. D. Gale, A. García, J. Junquera, P. Ordejón, and D. Sánchez-Portal, "The SIESTA method for *ab initio* order-*N* materials simulation," J. Phys.: Condens. Matter **14**, 2745 (2002).
[192]O. F. Sankey and D. J. Niklewski, "*Ab initio* multicenter tight-binding model for molecular-dynamics simulations and other applications in covalent systems," Phys. Rev. B **40**, 3979–3995 (1989).
[193]D. Porezag, T. Frauenheim, T. Köhler, G. Seifert, and R. Kaschner, "Construction of tight-binding-like potentials on the basis of density-functional theory: Application to carbon," Phys. Rev. B **51**, 12947–12957 (1995).
[194]A. P. Horsfield, "Efficient *ab initio* tight binding," Phys. Rev. B **56**, 6594–6602 (1997).
[195]J. Junquera, Ó. Paz, D. Sánchez-Portal, and E. Artacho, "Numerical atomic orbitals for linear-scaling calculations," Phys. Rev. B **64**, 235111 (2001).
[196]T. Ozaki, "Variationally optimized atomic orbitals for large-scale electronic structures," Phys. Rev. B **67**, 155108 (2003).
[197]T. Ozaki and H. Kino, "Numerical atomic basis orbitals from H to Kr," Phys. Rev. B **69**, 195113 (2004).
[198]D. Sanchez-Portal, E. Artacho, and J. M. Soler, "Projection of plane-wave calculations into atomic orbitals," Solid State Commun. **95**, 685–690 (1995).
[199]D. Sánchez-Portal, E. Artacho, and J. M. Soler, "Analysis of atomic orbital basis sets from the projection of plane-wave results," J. Phys.: Condens. Matter **8**, 3859 (1996).
[200]P. D. Haynes and M. C. Payne, "Localised spherical-wave basis set for $O(N)$ total-energy pseudopotential calculations," Comput. Phys. Commun. **102**, 17–27 (1997).
[201]M. Schlipf and F. Gygi, "Optimization algorithm for the generation of ONCV pseudopotentials," Comput. Phys. Commun. **196**, 36–44 (2015).

[202]ABACUS Team, "CGH and LRH basis sets," https://abacus.ustc.edu.cn/pseudo/list.htm (2020).
[203]H. Zhang, Z. Deng, Y. Liu, T. Liu, M. Chen, S. Yin, and L. He, "GPU acceleration of numerical atomic orbitals-based density functional theory algorithms within the ABACUS package," arXiv:2409.09399 (2024).
[204]https://netlib.org/scalapack/, 2024.
[205]https://elpa.mpcdf.mpg.de/, 2024.
[206]V. W.-z. Yu, J. Moussa, P. Kuus, A. Marek, P. Messmer, M. Yoon, H. Lederer, and V. Blum, "GPU-acceleration of the ELPA2 distributed eigensolver for dense symmetric and hermitian eigenproblems," Comput. Phys. Commun. **262**, 107808 (2021).
[207]A. Seidl, A. Görling, P. Vogl, J. A. Majewski, and M. Levy, "Generalized Kohn-Sham schemes and the band-gap problem," Phys. Rev. B **53**, 3764–3774 (1996).
[208]J. P. Perdew and K. Schmidt, "Jacob's ladder of density functional approximations for the exchange-correlation energy," AIP Conf. Proc. **577**, 1–20 (2001).
[209]J. P. Perdew and A. Zunger, "Self-interaction correction to density-functional approximations for many-electron systems," Phys. Rev. B **23**, 5048–5079 (1981).
[210]P. Mori-Sánchez, A. J. Cohen, and W. Yang, "Localization and delocalization errors in density functional theory and implications for band-gap prediction," Phys. Rev. Lett. **100**, 146401 (2008).
[211]M. Ernzerhof and G. E. Scuseria, "Assessment of the Perdew–Burke–Ernzerhof exchange-correlation functional," J. Chem. Phys. **110**, 5029–5036 (1999).
[212]K. Hui and J.-D. Chai, "SCAN-based hybrid and double-hybrid density functionals from models without fitted parameters," J. Chem. Phys. **144**, 044114 (2016).
[213]S. Lehtola, C. Steigemann, M. J. T. Oliveira, and M. A. L. Marques, "Recent developments in LIBXC — A comprehensive library of functionals for density functional theory," SoftwareX **7**, 1–5 (2018).
[214]J. L. Whitten, "Coulombic potential energy integrals and approximations," J. Chem. Phys. **58**, 4496–4501 (1973).
[215]M. Feyereisen, G. Fitzgerald, and A. Komornicki, "Use of approximate integrals in ab initio theory. An application in MP2 energy calculations," Chem. Phys. Lett. **208**, 359–363 (1993).
[216]O. Vahtras, J. Almlöf, and M. Feyereisen, "Integral approximations for LCAO-SCF calculations," Chem. Phys. Lett. **213**, 514–518 (1993).
[217]X. Ren, P. Rinke, V. Blum, J. Wieferink, A. Tkatchenko, A. Sanfilippo, K. Reuter, and M. Scheffler, "Resolution-of-identity approach to Hartree–Fock, hybrid density functionals, RPA, MP2 and *GW* with numeric atom-centered orbital basis functions," New J. Phys. **14**, 053020 (2012).
[218]S. V. Levchenko, X. Ren, J. Wieferink, R. Johanni, P. Rinke, V. Blum, and M. Scheffler, "Hybrid functionals for large periodic systems in an all-electron, numeric atom-centered basis framework," Comput. Phys. Commun. **192**, 60–69 (2015).
[219]A. C. Ihrig, J. Wieferink, I. Y. Zhang, M. Ropo, X. Ren, P. Rinke, M. Scheffler, and V. Blum, "Accurate localized resolution of identity approach for linear-scaling hybrid density functionals and for many-body perturbation theory," New J. Phys. **17**, 093020 (2015).
[220]Y. Ji, P. Lin, X. Ren, and L. He, "Reproducibility of hybrid density functional calculations for equation-of-state properties and band gaps," J. Phys. Chem. A **126**, 5924–5931 (2022).
[221]LibRI: https://github.com/abacusmodeling/LibRI (2024).
[222]LibRPA: https://github.com/Srlive1201/LibRPA (2024).
[223]P. Lin, Y. Ji, L. He, and X. Ren, "Efficient hybrid-functional-based force and stress calculations for periodic systems with thousands of atoms," J. Chem. Theory Comput. **21**, 3394–3409 (2025).
[224]Y. Ji, P. Lin, X. Ren, and L. He, "Geometric and electronic structures of $Cs_2BB'X_6$ double perovskites: The importance of exact exchange," Phys. Rev. Res. **6**, 033172 (2024).
[225]Z. Tang, H. Li, P. Lin, X. Gong, G. Jin, L. He, H. Jiang, X. Ren, W. Duan, and Y. Xu, "A deep equivariant neural network approach for efficient hybrid density functional calculations," Nat. Commun. **15**, 8815 (2024).
[226]Z.-H. Cui, Y.-C. Wang, M.-Y. Zhang, X. Xu, and H. Jiang, "Doubly screened hybrid functional: An accurate first-principles approach for both narrow- and wide-gap semiconductors," J. Phys. Chem. Lett. **9**, 2338–2345 (2018).
[227]B. Delley, "An all-electron numerical method for solving the local density functional for polyatomic molecules," J. Chem. Phys. **92**, 508–517 (1990).
[228]H. J. Kulik, T. Hammerschmidt, J. Schmidt, S. Botti, M. A. L. Marques, M. Boley, M. Scheffler, M. Todorović, P. Rinke, C. Oses, A. Smolyanyuk, S. Curtarolo, A. Tkatchenko, A. P. Bartók, S. Manzhos, M. Ihara, T. Carrington, J. Behler, O. Isayev, M. Veit, A. Grisafi, J. Nigam, M. Ceriotti, K. T. Schütt, J. Westermayr, M. Gastegger, R. J. Maurer, B. Kalita, K. Burke, R. Nagai, R. Akashi, O. Sugino, J. Hermann, F. Noé, S. Pilati, C. Draxl, M. Kuban, S. Rigamonti, M. Scheidgen, M. Esters, D. Hicks, C. Toher, P. V. Balachandran, I. Tamblyn, S. Whitelam, C. Bellinger, and L. M. Ghiringhelli, "Roadmap on machine learning in electronic structure," Electron. Struct. **4**, 023004 (2022).
[229]B. Huang, G. F. Von Rudorff, and O. A. Von Lilienfeld, "The central role of density functional theory in the AI age," Science **381**, 170–175 (2023).
[230]W. Li, Q. Ou, Y. Chen, Y. Cao, R. Liu, C. Zhang, D. Zheng, C. Cai, X. Wu, H. Wang, M. Chen, and L. Zhang, "DeePKS + ABACUS as a bridge between expensive quantum mechanical models and machine learning potentials," J. Phys. Chem. A **126**(49), 9154–9164 (2022).
[231]Q. Ou, P. Tuo, W. Li, X. Wang, Y. Chen, and L. Zhang, "DeePKS model for halide perovskites with the accuracy of a hybrid functional," J. Phys. Chem. C **127**, 18755–18764 (2023).
[232]P. Zhang, A. T. Gardini, X. Xu, and M. Parrinello, "Intramolecular and water mediated tautomerism of solvated glycine," J. Chem. Inf. Model. **64**, 3599–3604 (2024).
[233]Y. Zhao and D. G. Truhlar, "The M06 suite of density functionals for main group thermochemistry, thermochemical kinetics, noncovalent interactions, excited states, and transition elements: Two new functionals and systematic testing of four M06-class functionals and 12 other functionals," Theor. Chem. Acc. **120**, 215–241 (2008).
[234]M. Invernizzi and M. Parrinello, "Rethinking metadynamics: From bias potentials to probability distributions," J. Phys. Chem. Lett. **11**, 2731–2736 (2020).
[235]P. Zhang and X. Xu, "Propensity of water self-ions at air(oil)–water interfaces revealed by deep potential molecular dynamics with enhanced sampling," Langmuir **41**, 3675–3683 (2025).
[236]X. Liang, R. Liu, and M. Chen, "A deep learning framework for the electronic structure of water: Toward a universal model," J. Chem. Theory Comput. **21**, 6849 (2025).
[237]M. J. Han, T. Ozaki, and J. Yu, "O(N) LDA+U electronic structure calculation method based on the nonorthogonal pseudoatomic orbital basis," Phys. Rev. B **73**, 045110 (2006).
[238]F. Tran, P. Blaha, K. Schwarz, and P. Novák, "Hybrid exchange-correlation energy functionals for strongly correlated electrons: Applications to transition-metal monoxides," Phys. Rev. B **74**, 155108 (2006).
[239]L. Messick, W. C. Walker, and R. Glosser, "Direct and temperature-modulated reflectance spectra of MnO, CoO, and NiO," Phys. Rev. B **6**, 3941 (1972).
[240]A. K. Cheetham and D. A. O. Hope, "Magnetic ordering and exchange effects in the antiferromagnetic solid solutions $Mn_xNi_{1-x}O$," Phys. Rev. B **27**, 6964 (1983).
[241]H. K. Bowen, D. Adler, and B. H. Auker, "Electrical and optical properties of FeO," J. Solid State Chem. **12**, 355–359 (1975).
[242]B. E. F. Fender, A. J. Jacobson, and F. A. Wedgwood, "Covalency parameters in MnO, α-MnS, and NiO," J. Chem. Phys. **48**, 990–994 (1968).
[243]R. J. Powell and W. E. Spicer, "Optical properties of NiO and CoO," Phys. Rev. B **2**, 2182 (1970).
[244]W. L. Roth, "Magnetic structures of MnO, FeO, CoO, and NiO," Phys. Rev. **110**, 1333 (1958).
[245]G. A. Sawatzky and J. W. Allen, "Magnitude and origin of the band gap in NiO," Phys. Rev. Lett. **53**, 2339 (1984).
[246]S. Hüfner, J. Osterwalder, T. Riesterer, and F. Hulliger, "Photoemission and inverse photoemission spectroscopy of NiO," Solid State Commun. **52**, 793–796 (1984).
[247]D. C. Khan and R. A. Erickson, "Magnetic form factor of Co^{++} ion in cobaltous oxide," Phys. Rev. B **1**, 2243 (1970).
[248]E. Runge and E. K. U. Gross, "Density-functional theory for time-dependent systems," Phys. Rev. Lett. **52**, 997 (1984).
[249]J. Ren, E. Kaxiras, and S. Meng, "Optical properties of clusters and molecules from real-time time-dependent density functional theory using a self-consistent field," Mol. Phys. **108**, 1829–1844 (2010).

[250]I. Maliyov, J.-P. Crocombette, and F. Bruneval, "Electronic stopping power from time-dependent density-functional theory in Gaussian basis," Eur. Phys. J. B **91**, 172 (2018).
[251]Y. Ren, Y. Fu, N. Li, C. You, J. Huang, K. Huang, Z. Sun, J. Zhou, Y. Si, Y. Zhu, W. Chen, L. Duan, and M. Liu, "Concentrated solar CO_2 reduction in H_2O vapour with >1% energy conversion efficiency," Nat. Commun. **15**, 4675 (2024).
[252]S. Meng and E. Kaxiras, "Real-time, local basis-set implementation of time-dependent density functional theory for excited state dynamics simulations," J. Chem. Phys. **129**, 054110 (2008).
[253]C. Lian, M. Guan, S. Hu, J. Zhang, and S. Meng, "Photoexcitation in solids: First-principles quantum simulations by real-time TDDFT," Adv. Theory Simul. **1**, 1800055 (2018).
[254]H. Zhao and L. He, "Hybrid gauge approach for accurate real-time TDDFT simulations with numerical atomic orbitals," J. Chem. Theory Comput. **21**, 3335–3341 (2025).
[255]J. Chen, Y. Ren, Y. Fu, Y. Si, J. Huang, J. Zhou, M. Liu, L. Duan, and N. Li, "Integration of Co single atoms and Ni clusters on defect-rich ZrO_2 for strong photothermal coupling boosts photocatalytic CO_2 reduction," ACS Nano **18**, 13035–13048 (2024).
[256]D. Zhang, H. Bi, F.-Z. Dai, W. Jiang, X. Liu, L. Zhang, and H. Wang, "Pretraining of attention-based deep learning potential model for molecular simulation," npj Comput. Mater. **10**, 94 (2024).
[257]D. Zhang, X. Liu, X. Zhang, C. Zhang, C. Cai, H. Bi, Y. Du, X. Qin, A. Peng, J. Huang, B. Li, Y. Shan, J. Zeng, Y. Zhang, S. Liu, Y. Li, J. Chang, X. Wang, S. Zhou, J. Liu, X. Luo, Z. Wang, W. Jiang, J. Wu, Y. Yang, J. Yang, M. Yang, F.-Q. Gong, L. Zhang, M. Shi, F.-Z. Dai, D. M. York, S. Liu, T. Zhu, Z. Zhong, J. Lv, J. Cheng, W. Jia, M. Chen, G. Ke, W. E, L. Zhang, and H. Wang, "DPA-2: A large atomic model as a multi-task learner," npj Comput. Mater. **10**, 293 (2024).
[258]N. A. W. Holzwarth, M. Torrent, J.-B. Charraud, and M. Côté, "Cubic spline solver for generalized density functional treatments of atoms and generation of atomic datasets for use with exchange-correlation functionals including meta-GGA," Phys. Rev. B **105**, 125144 (2022).
[259]K. Lejaeghere, G. Bihlmayer, T. Björkman, P. Blaha, S. Blügel, V. Blum, D. Caliste, I. E. Castelli, S. J. Clark, A. Dal Corso, S. de Gironcoli, T. Deutsch, J. K. Dewhurst, I. Di Marco, C. Draxl, M. Dułak, O. Eriksson, J. A. Flores-Livas, K. F. Garrity, L. Genovese, P. Giannozzi, M. Giantomassi, S. Goedecker, X. Gonze, O. Grånäs, E. K. U. Gross, A. Gulans, F. Gygi, D. R. Hamann, P. J. Hasnip, N. A. W. Holzwarth, D. Iuşan, D. B. Jochym, F. Jollet, D. Jones, G. Kresse, K. Koepernik, E. Küçükbenli, Y. O. Kvashnin, I. L. M. Locht, S. Lubeck, M. Marsman, N. Marzari, U. Nitzsche, L. Nordström, T. Ozaki, L. Paulatto, C. J. Pickard, W. Poelmans, M. I. J. Probert, K. Refson, M. Richter, G.-M. Rignanese, S. Saha, M. Scheffler, M. Schlipf, K. Schwarz, S. Sharma, F. Tavazza, P. Thunström, A. Tkatchenko, M. Torrent, D. Vanderbilt, M. J. van Setten, V. Van Speybroeck, J. M. Wills, J. R. Yates, G.-X. Zhang, and S. Cottenier, "Reproducibility in density functional theory calculations of solids," Science **351**, aad3000 (2016).
[260]A. Jain, J. Montoya, S. Dwaraknath, N. E. Zimmermann, J. Dagdelen, M. Horton, P. Huck, D. Winston, S. Cholia, S. P. Ong *et al.*, "The materials project: Accelerating materials design through theory-driven data and tools," in *Handbook of Materials Modeling: Methods: Theory and Modeling* (Springer, 2020), pp. 1751–1784.
[261]L. Talirz, S. Kumbhar, E. Passaro, A. V. Yakutovich, V. Granata, F. Gargiulo, M. Borelli, M. Uhrin, S. P. Huber, S. Zoupanos *et al.*, "Materials Cloud, a platform for open computational science," Sci. Data **7**, 299 (2020).
[262]D. D. Landis, J. S. Hummelshøj, S. Nestorov, J. Greeley, M. Dułak, T. Bligaard, J. K. Nørskov, and K. W. Jacobsen, "The computational materials repository," Comput. Sci. Eng. **14**, 51–57 (2012).
[263]See http://www.quantum-simulation.org/potentials/sg15_oncv/ for SG15 ONCV Potentials.
[264]See http://www.pseudo-dojo.org/ for Pseudo Dojo.
[265]See https://www.pwmat.com/potential-download for PWmat-website.
[266]M. Krack, "Pseudopotentials for H to Kr optimized for gradient-corrected exchange-correlation functionals," Theor. Chem. Acc. **114**, 145–152 (2005).
[267]See http://theossrv1.epfl.ch/Main/Pseudopotentials for theos-pp.
[268]K. F. Garrity, J. W. Bennett, K. M. Rabe, and D. Vanderbilt, "Pseudopotentials for high-throughput DFT calculations," Comput. Mater. Sci. **81**, 446–452 (2014).
[269]See https://www.physics.rutgers.edu/gbrv/ for GBRV pseudopotentials.
[270]C. W. Andersen, R. Armiento, E. Blokhin, G. J. Conduit, S. Dwaraknath, M. L. Evans, Á. Fekete, A. Gopakumar, S. Gražulis, A. Merkys *et al.*, "OPTIMADE, an API for exchanging materials data," Sci. Data **8**, 217 (2021).
[271]S. Gražulis, D. Chateigner, R. T. Downs, A. Yokochi, M. Quirós, L. Lutterotti, E. Manakova, J. Butkus, P. Moeck, and A. Le Bail, "Crystallography open database – An open-access collection of crystal structures," J. Appl. Crystallogr. **42**, 726–729 (2009).
[272]A. Togo, K. Shinohara, and I. Tanaka, "Spglib: A software library for crystal symmetry search," Sci. Technol. Adv. Mater.: Methods **4**, 2384822 (2024).
[273]Y. Hinuma, G. Pizzi, Y. Kumagai, F. Oba, and I. Tanaka, "Band structure diagram paths based on crystallography," Comput. Mater. Sci. **128**, 140–184 (2017).
[274]G. Prandini, A. Marrazzo, I. E. Castelli, N. Mounet, and N. Marzari, "Precision and efficiency in solid-state pseudopotential calculations," npj Comput. Mater. **4**, 72 (2018).
[275]K. Lejaeghere, V. Van Speybroeck, G. Van Oost, and S. Cottenier, "Error estimates for solid-state density-functional theory predictions: An overview by means of the ground-state elemental crystals," Crit. Rev. Solid State Mater. Sci. **39**, 1–24 (2014).
[276]F. Birch, "Finite elastic strain of cubic crystals," Phys. Rev. **71**, 809 (1947).
[277]J. Wu, J. Yang, Y.-J. Liu, D. Zhang, Y. Yang, Y. Zhang, L. Zhang, and S. Liu, "Universal interatomic potential for perovskite oxides," Phys. Rev. B **108**, L180104 (2023).
[278]J. Wu, J. Yang, L. Ma, L. Zhang, and S. Liu, "Modular development of deep potential for complex solid solutions," Phys. Rev. B **107**, 144102 (2023).
[279]F.-H. Gong, Y.-L. Tang, Y.-L. Zhu, H. Zhang, Y.-J. Wang, Y.-T. Chen, Y.-P. Feng, M.-J. Zou, B. Wu, W.-R. Geng *et al.*, "Atomic mapping of periodic dipole waves in ferroelectric oxide," Sci. Adv. **7**, eabg5503 (2021).
[280]J. Liu, X. Zhang, T. Chen, Y. Zhang, D. Zhang, L. Zhang, and M. Chen, "Machine-learning-based interatomic potentials for group IIB to VIA semiconductors: Toward a universal model," J. Chem. Theory Comput. **20**(13), 5717–5731 (2024).
[281]D. Zhang, A. Peng, C. Cai, W. Li, Y. Zhou, J. Zeng, M. Guo, C. Zhang, B. Li, H. Jiang *et al.*, "A graph neural network for the era of large atomistic models," arXiv:2506.01686 (2025).
[282]https://github.com/ZLI-afk/static/tree/main/storage/abacus_alloy_pp, 2024.
[283]Y. Zhang, H. Wang, W. Chen, J. Zeng, L. Zhang, H. Wang, and W. E, "DP-GEN: A concurrent learning platform for the generation of reliable deep learning based potential energy models," Comput. Phys. Commun. **253**, 107206 (2020).
[284]Z. Li, T. Wen, Y. Zhang, X. Liu, C. Zhang, A. S. L. S. Pattamatta, X. Gong, B. Ye, H. Wang, L. Zhang, and D. J. Srolovitz, "APEX: An automated cloud-native material property explorer," npj Comput. Mater. **11**, 88 (2025).
[285]I. Batatia, P. Benner, Y. Chiang, A. M. Elena, D. P. Kovács, J. Riebesell, X. R. Advincula, M. Asta, M. Avaylon, W. J. Baldwin, F. Berger, N. Bernstein, A. Bhowmik, S. M. Blau, V. Cărare, J. P. Darby, S. De, F. D. Pia, V. L. Deringer, R. Elijošius, Z. El-Machachi, F. Falcioni, E. Fako, A. C. Ferrari, A. Genreith-Schriever, J. George, R. E. A. Goodall, C. P. Grey, P. Grigorev, S. Han, W. Handley, H. H. Heenen, K. Hermansson, C. Holm, J. Jaafar, S. Hofmann, K. S. Jakob, H. Jung, V. Kapil, A. D. Kaplan, N. Karimitari, J. R. Kermode, N. Kroupa, J. Kullgren, M. C. Kuner, D. Kuryla, G. Liepuoniute, J. T. Margraf, I.-B. Magdău, A. Michaelides, J. H. Moore, A. A. Naik, S. P. Niblett, S. W. Norwood, N. O'Neill, C. Ortner, K. A. Persson, K. Reuter, A. S. Rosen, L. L. Schaaf, C. Schran, B. X. Shi, E. Sivonxay, T. K. Stenczel, V. Svahn, C. Sutton, T. D. Swinburne, J. Tilly, C. van der Oord, E. Varga-Umbrich, T. Vegge, M. Vondrák, Y. Wang, W. C. Witt, F. Zills, and G. Csányi, "A foundation model for atomistic materials chemistry," arXiv:2401.00096 [physics.chem-ph] (2024).
[286]A. Togo, L. Chaput, T. Tadano, and I. Tanaka, "Implementation strategies in phonopy and phono3py," J. Phys.: Condens. Matter **35**, 353001 (2023).
[287]A. Togo, "First-principles phonon calculations with phonopy and phono3py," J. Phys. Soc. Jpn. **92**, 012001 (2023).
[288]L. Zhang, J. Han, H. Wang, W. A. Saidi, R. Car, and E. Weinan, "End-to-end symmetry preserving inter-atomic potential energy model for finite and extended systems," in *Proceedings of the 32nd International Conference on Neural Information Processing Systems, NIPS'18* (Curran Associates, Inc., 2018), pp. 4441–4451.
[289]https://github.com/deepmodeling/dpdata, 2024.

[290]L. Zhang, D.-Y. Lin, H. Wang, R. Car, and W. E, "Active learning of uniformly accurate interatomic potentials for materials simulation," Phys. Rev. Mater. **3**, 023804 (2019).
[291]J. Wu, Y. Zhang, L. Zhang, and S. Liu, "Deep learning of accurate force field of ferroelectric HfO_2," Phys. Rev. B **103**, 024108 (2021).
[292]Y. Shi, R. He, B. Zhang, and Z. Zhong, "Revisiting the phase diagram and piezoelectricity of lead zirconate titanate from first principles," Phys. Rev. B **109**, 174104 (2024).
[293]J. Zeng, T. J. Giese, Ş. Ekesan, and D. M. York, "Development of range-corrected deep learning potentials for fast, accurate quantum mechanical/molecular mechanical simulations of chemical reactions in solution," J. Chem. Theory Comput. **17**, 6993–7009 (2021).
[294]M. Yang, L. Bonati, D. Polino, and M. Parrinello, "Using metadynamics to build neural network potentials for reactive events: The case of urea decomposition in water," Catal. Today **387**, 143–149 (2022).
[295]T. E. Gartner, L. Zhang, P. M. Piaggi, R. Car, A. Z. Panagiotopoulos, and P. G. Debenedetti, "Signatures of a liquid–liquid transition in an ab initio deep neural network model for water," Proc. Natl. Acad. Sci. U. S. A. **117**, 26040–26046 (2020).
[296]F. Fu, X. Wang, L. Zhang, Y. Yang, J. Chen, B. Xu, C. Ouyang, S. Xu, F.-Z. Dai, and W. E, "Unraveling the atomic-scale mechanism of phase transformations and structural evolutions during (de)lithiation in Si anodes," Adv. Funct. Mater. **33**, 2303936 (2023).
[297]H. Li, Z. Wang, N. Zou, M. Ye, R. Xu, X. Gong, W. Duan, and Y. Xu, "Deep-learning density functional theory Hamiltonian for efficient ab initio electronic-structure calculation," Nat. Comput. Sci. **2**, 367–377 (2022).
[298]W. Kohn, "Density functional and density matrix method scaling linearly with the number of atoms," Phys. Rev. Lett. **76**, 3168 (1996).
[299]X. Gong, H. Li, N. Zou, R. Xu, W. Duan, and Y. Xu, "General framework for E(3)-equivariant neural network representation of density functional theory Hamiltonian," Nat. Commun. **14**, 2848 (2023).
[300]H. Li, Z. Tang, J. Fu, W.-H. Dong, N. Zou, X. Gong, W. Duan, and Y. Xu, "Deep-learning density functional perturbation theory," Phys. Rev. Lett. **132**, 096401 (2024).
[301]See https://github.com/mzjb/DeepH-pack for DeepH.
[302]See https://github.com/Xiaoxun-Gong/DeepH-E3 for DeepH.
[303]Y. Wang, H. Li, Z. Tang, H. Tao, Y. Wang, Z. Yuan, Z. Chen, W. Duan, and Y. Xu, "DeepH-2: Enhancing deep-learning electronic structure via an equivariant local-coordinate transformer," arXiv:2401.17015 (2024).
[304]S. Yang, J. Chen, C.-F. Liu, and M. Chen, "Evolution of flat bands in $MoSe_2/WSe_2$ moiré lattices: A study combining machine learning and band unfolding methods," Phys. Rev. B **110**, 235410 (2024).
[305]H. Li, Z. Tang, X. Gong, N. Zou, W. Duan, and Y. Xu, "Deep-learning electronic-structure calculation of magnetic superstructures," Nat. Comput. Sci. **3**, 321 (2023).
[306]Z. Tang, H. Li, P. Lin, X. Gong, G. Jin, L. He, H. Jiang, X. Ren, W. Duan, and Y. Xu (2023). "Code and dataset for the article "A deep equivariant neural network approach for efficient hybrid density functional calculations," Zenodo. https://doi.org/10.5281/zenodo.13444159
[307]X. Gong, S. G. Louie, W. Duan, and Y. Xu, "Generalizing deep learning electronic structure calculation to the plane-wave basis," Nat. Comput. Sci. **4**, 752–760 (2024).
[308]Y. Wang, Y. Li, Z. Tang, H. Li, Z. Yuan, H. Tao, N. Zou, T. Bao, X. Liang, Z. Chen *et al.*, "Universal materials model of deep-learning density functional theory Hamiltonian," Sci. Bull. **69**, 2514 (2024).
[309]Q. Gu, Z. Zhouyin, S. K. Pandey, P. Zhang, L. Zhang, and W. E, "Deep learning tight-binding approach for large-scale electronic simulations at finite temperatures with ab initio accuracy," Nat. Commun. **15**, 6772 (2024).
[310]Z. Zhouyin, Z. Gan, S. K. Pandey, L. Zhang, and Q. Gu, "Learning local equivariant representations for quantum operators," arXiv:2407.06053 [cond-mat, physics:quant-ph] (2024).
[311]J. Zou, Z. Zhouyin, D. Lin, L. Zhang, S. Hou, and Q. Gu, "Deep learning accelerated quantum transport simulations in nanoelectronics: From break junctions to field-effect transistors," arXiv:2411.08800 (2024).
[312]Y. Zhong, H. Yu, M. Su, X. Gong, and H. Xiang, "Transferable equivariant graph neural networks for the Hamiltonians of molecules and solids," npj Comput. Mater. **9**, 182 (2023).
[313]Y. Zhong, B. Zhang, H. Yu, X. Gong, and H. Xiang, "Accelerating the electronic-structure calculation of magnetic systems by equivariant neural networks," arXiv:2306.01558 (2023).
[314]D. Zhao, Y. Zhong, T. Yuan, H. Wang, T. Jiang, Y. Qi, H. Xiang, X. Gong, D. Feng, and T. Zhang, "Revealing higher-order topological bulk-boundary correspondence in bismuth crystal with spin-helical hinge state loop and proximity superconductivity," Sci. Bull. **70**, 3310 (2025); arXiv:2502.07533.
[315]W. Luo, Y. Zhong, H. Yu, M. Xie, Y. Chen, H. Xiang, and L. Bellaiche, "Topological interfacial states at phase boundaries in two-dimensional ferroelectric bismuth," Phys. Rev. B **111**, 075407 (2025).
[316]K. Wang, M. Huang, Z. Dai, S. Yan, Z. Guo, H. Xiang, X.-G. Gong, and S. Chen, "Silicon nanowire gate-all-around cold source MOSFET with ultralow power dissipation: A machine-learning-Hamiltonian accelerated design," Adv. Funct. Mater. (published online 2025).
[317]Y. Zhong, H. Yu, J. Yang, X. Guo, H. Xiang, and X. Gong, "Universal machine learning Kohn–Sham Hamiltonian for materials," Chin. Phys. Lett. **41**, 077103 (2024).
[318]Y. Zhong, R. Wang, X. Gong, and H. Xiang, "A universal spin-orbit-coupled Hamiltonian model for accelerated quantum material discovery," arXiv:2504.19586 (2025).
[319]Y. Zhong, S. Liu, B. Zhang, Z. Tao, Y. Sun, W. Chu, X.-G. Gong, J.-H. Yang, and H. Xiang, "Accelerating the calculation of electron–phonon coupling strength with machine learning," Nat. Comput. Sci. **4**, 615–625 (2024).
[320]C. Zhang, Y. Zhong, Z.-G. Tao, X. Qin, H. Shang, Z. Lan, O. V. Prezhdo, X.-G. Gong, W. Chu, and H. Xiang, "Advancing nonadiabatic molecular dynamics simulations in solids with E(3) equivariant deep neural Hamiltonians," Nat. Commun. **16**, 2033 (2025).
[321]https://github.com/QuantumLab-ZY/HamGNN/tree/main/utils_abacus, 2025.
[322]G. Jin, H. Pang, Y. Ji, Z. Dai, and L. He, "PYATB: An efficient Python package for electronic structure calculations using ab initio tight-binding model," Comput. Phys. Commun. **291**, 108844 (2023).
[323]D. Xiao, M.-C. Chang, and Q. Niu, "Berry phase effects on electronic properties," Rev. Mod. Phys. **82**, 1959–2007 (2010).
[324]M. Z. Hasan and C. L. Kane, "Colloquium: Topological insulators," Rev. Mod. Phys. **82**, 3045–3067 (2010).
[325]B. I. Sturman and V. M. Fridkin, *The Photovoltaic and Photorefractive Effects in Noncentrosymmetric Materials* (Gordon and Breach Science Publishers, 1992).
[326]J. E. Sipe and A. I. Shkrebtii, "Second-order optical response in semiconductors," Phys. Rev. B **61**, 5337–5352 (2000).
[327]G. Jin and L. He, "Peculiar band geometry induced giant shift current in ferroelectric SnTe monolayer," npj Comput. Mater. **10**, 23 (2024).
[328]I. Sodemann and L. Fu, "Quantum nonlinear Hall effect induced by Berry curvature dipole in time-reversal invariant materials," Phys. Rev. Lett. **115**, 216806 (2015).
[329]H. Pang, G. Jin, and L. He, "Tuning of Berry-curvature dipole in TaAs slabs: An effective route to enhance the nonlinear Hall response," Phys. Rev. Mater. **8**, 043403 (2024).
[330]G. Jin, D. Zheng, and L. He, "Calculation of Berry curvature using non-orthogonal atomic orbitals," J. Phys.: Condens. Matter **33**, 325503 (2021).
[331]Q. Zheng, W. Chu, C. Zhao, L. Zhang, H. Guo, Y. Wang, X. Jiang, and J. Zhao, "*Ab initio* nonadiabatic molecular dynamics investigations on the excited carriers in condensed matter systems," Wiley Interdiscip. Rev.: Comput. Mol. Sci. **9**, e1411 (2019).
[332]Z. Zheng, Q. Zheng, and J. Zhao, "Spin-orbit coupling induced demagnetization in Ni: *Ab initio* nonadiabatic molecular dynamics perspective," Phys. Rev. B **105**, 085142 (2022).
[333]X. Jiang, Q. Zheng, Z. Lan, W. A. Saidi, X. Ren, and J. Zhao, "Real-time *GW*-BSE investigations on spin-valley exciton dynamics in monolayer transition metal dichalcogenide," Sci. Adv. **7**, eabf3759 (2021).
[334]Z. Zheng, Y. Shi, J.-J. Zhou, O. V. Prezhdo, Q. Zheng, and J. Zhao, "*Ab initio* real-time quantum dynamics of charge carriers in momentum space," Nat. Comput. Sci. **3**, 532–541 (2023).
[335]https://wiki.fysik.dtu.dk/ase, 2024.
[336]https://gitlab.com/1041176461/ase-abacus, 2024.

[337]H. Jónsson, G. Mills, and K. W. Jacobsen, "Nudged elastic band method for finding minimum energy paths of transitions," in *Classical and Quantum Dynamics in Condensed Phase Simulations* (World Scientific, 1998), pp. 385–404.
[338]G. Henkelman and H. Jónsson, "Improved tangent estimate in the nudged elastic band method for finding minimum energy paths and saddle points," J. Chem. Phys. **113**, 9978–9985 (2000).
[339]G. Henkelman, B. P. Uberuaga, and H. Jónsson, "A climbing image nudged elastic band method for finding saddle points and minimum energy paths," J. Chem. Phys. **113**, 9901–9904 (2000).
[340]G. Henkelman and H. Jónsson, "A dimer method for finding saddle points on high dimensional potential surfaces using only first derivatives," J. Chem. Phys. **111**, 7010–7022 (1999).
[341]R. A. Olsen, G. J. Kroes, G. Henkelman, A. Arnaldsson, and H. Jónsson, "Comparison of methods for finding saddle points without knowledge of the final states," J. Chem. Phys. **121**, 9776–9792 (2004).
[342]A. Heyden, A. T. Bell, and F. J. Keil, "Efficient methods for finding transition states in chemical reactions: Comparison of improved dimer method and partitioned rational function optimization method," J. Chem. Phys. **123**, 224101 (2005).
[343]J. Kästner and P. Sherwood, "Superlinearly converging dimer method for transition state search," J. Chem. Phys. **128**, 014106 (2008).
[344]P. Lindgren, G. Kastlunger, and A. A. Peterson, "Scaled and dynamic optimizations of nudged elastic bands," J. Chem. Theory Comput. **15**, 5787–5793 (2019).
[345]E. L. Kolsbjerg, M. N. Groves, and B. Hammer, "An automated nudged elastic band method," J. Chem. Phys. **145**, 094107 (2016).
[346]E. D. Hermes, K. Sargsyan, H. N. Najm, and J. Zádor, "Accelerated saddle point refinement through full exploitation of partial Hessian diagonalization," J. Chem. Theory Comput. **15**, 6536–6549 (2019).
[347]E. D. Hermes, K. Sargsyan, H. N. Najm, and J. Zádor, "Geometry optimization speedup through a geodesic approach to internal coordinates," J. Chem. Phys. **155**, 094105 (2021).
[348]E. D. Hermes, K. Sargsyan, H. N. Najm, and J. Zádor, "Sella, an open-source automation-friendly molecular saddle point optimizer," J. Chem. Theory Comput. **18**, 6974–6988 (2022).
[349]https://github.com/QuantumMisaka/ATST-Tools, 2024.
[350]L.-W. Wang, L.-S. Xie, P.-X. Xu, and K. Xia, "First-principles study of magnon-phonon interactions in gadolinium iron garnet," Phys. Rev. B **101**, 165137 (2020).
[351]W. Li, J. Carrete, N. A. Katcho, and N. Mingo, "ShengBTE: A solver of the Boltzmann transport equation for phonons," Comput. Phys. Commun. **185**, 1747–1758 (2014).
[352]X. He, N. Helbig, M. J. Verstraete, and E. Bousquet, "TB2J: A python package for computing magnetic interaction parameters," Comput. Phys. Commun. **264**, 107938 (2021).
[353]A. I. Liechtenstein, M. I. Katsnelson, V. P. Antropov, and V. A. Gubanov, "Local spin density functional approach to the theory of exchange interactions in ferromagnetic metals and alloys," J. Magn. Magn. Mater. **67**, 65–74 (1987).
[354]T. Zhang, Y. Cao, B. Zhang, H. Guo, L. Qiao, F. Li, and Z. Li, "Short-range order and strong interplay between local and itinerant magnetism in $GeFe_3N$," Phys. Rev. B **110**, 224419 (2024).
[355]G. Pizzi, V. Vitale, R. Arita, S. Blügel, F. Freimuth, G. Géranton, M. Gibertini, D. Gresch, C. Johnson, T. Koretsune, J. Ibañez-Azpiroz, H. Lee, J.-M. Lihm, D. Marchand, A. Marrazzo, Y. Mokrousov, J. I. Mustafa, Y. Nohara, Y. Nomura, L. Paulatto, S. Poncé, T. Ponweiser, J. Qiao, F. Thöle, S. S. Tsirkin, M. Wierzbowska, N. Marzari, D. Vanderbilt, I. Souza, A. A. Mostofi, and J. R. Yates, "Wannier90 as a community code: New features and applications," J. Phys.: Condens. Matter **32**, 165902 (2020).
[356]N. Marzari and D. Vanderbilt, "Maximally localized generalized Wannier functions for composite energy bands," Phys. Rev. B **56**, 12847–12865 (1997).
[357]Q. Wu, S. Zhang, H.-F. Song, M. Troyer, and A. A. Soluyanov, "WannierTools: An open-source software package for novel topological materials," Comput. Phys. Commun. **224**, 405–416 (2018).
[358]Y. Wang, J. Lv, L. Zhu, and Y. Ma, "CALYPSO: A method for crystal structure prediction," Comput. Phys. Commun. **183**, 2063–2070 (2012).
[359]A. R. Oganov and C. W. Glass, "Crystal structure prediction using *ab initio* evolutionary techniques: Principles and applications," J. Chem. Phys. **124**, 244704 (2006).